The Pennsylvania State University

The Graduate School

College of Engineering

NUMERICALLY EFFICIENT TECHNIQUES FOR THE ANALYSIS OF MMIC STRUCTURES

A Thesis in

Electrical Engineering

by

Soon Jae Kwon

© 2004 Soon Jae Kwon

Submitted in Partial Fulfillment
of the Requirements
for the Degree of

Doctor of Philosophy

December 2004

The thesis of Soon Jae Kwon was reviewed and approved* by the following:

Raj Mittra
Professor of Electrical Engineering
Thesis Advisor
Chair of Committee

Douglas H. Werner
Professor of Electrical Engineering

Lynn A. Carpenter
Associate Professor of Electrical Engineering

Michael T. Lanagan
Associate Professor of Engineering Science and Mechanics

W. Kenneth Jenkins
Professor of Electrical Engineering
Head of the Department of Electrical Engineering

*Signatures are on file in the Graduate School

ABSTRACT

The method of moments (MoM) has been widely used for the full-wave electromagnetic analysis of layered structures. It has been gaining in popularity because the conventional equivalent circuit based simulation techniques have difficulty in producing accurate results for circuits with complex geometry and high operating frequency. However, the MoM is a computationally intensive process and requires considerable computer resources to perform the analysis. This thesis proposes and validates several techniques to speed up different stages of the MoM process.

We first consider the computation of impedance matrix for layered structures. It is time-consuming since each element requires the evaluation of quadruple integrals. To increase the efficiency, we propose a technique, referred to as the Fast Matrix Generation (FMG). In this method, conventional and rigorous numerical methods are still used for generating the impedance matrix elements that are associated with the near-field interactions, while a more efficient scheme is employed where the separation distance between basis and testing functions exceeds a threshold value. A significant saving in computation time, sometimes over 90%, can be achieved via the application of this approach, as is demonstrated by numerical results for a number of typical microwave circuits.

The frequency response of microwave passive structures often involves one or more resonances, and this, in turn, requires the use of small frequency steps for their analysis. This imposes an enormous computational burden when computing their frequency response via the MoM process. We introduce an impedance matrix

interpolation technique that serves to reduce the computation time for the impedance matrix quite considerably, especially if the frequency band of interest is wide. In this approach, the frequency variation of the matrix element is expressed in term of interpolating polynomials with or without extracting the phase factor e^{-jkr}, depending on the separation distance between the source and field points. Although the concept of matrix interpolation is not entirely new, the accuracy has been improved in this work over those published previously. Furthermore, our algorithm has the added advantage that it can be readily incorporated into existing codes. The efficiency of this approach is validated by considering a variety of layered structure problems.

Next, the Characteristic Basis Function Method (CBFM) is proposed to reduce the matrix solution time for MoM analysis of large and/or complex geometries. The CBFs are special types of high-level basis functions, defined over domains that encompass a relatively large number of conventional subdomain bases, *e.g*., triangular patches or rooftops. In this approach, we define two kinds of CBFs that represent different kinds of interactions between the conventional subdomain bases contained in the CBFs. The primary CBF for a particular block is associated with the solution for the isolated block, while the secondary ones account for the mutual coupling effects between this block and others. Efficiency of the CBFM is demonstrated with several numerical examples

Finally, we present an iterative process for solving the matrix equation by using an extrapolated initial guess in conjunction with the Conjugate Gradient (CG) method. The initial guess is computed from the orthonormalized version of the solutions at previous frequencies. The number of iterations needed to make the residual error smaller

than a tolerance is reduced via the application of the extrapolated initial guess. The effectiveness of this approach is illustrated via several numerical examples.

TABLE OF CONTENTS

LIST OF FIGURES viii

LIST OF TABLES xii

ACKNOWLEDGEMENTS xiii

Chapter 1 INTRODUCTION 1

1.1 Research Objectives 7
1.2 Outline of the Thesis 9

Chapter 2 BASIC BACKGROUND FOR ELECTROMAGNETIC ANALYSIS OF PLANAR STRUCTURES 12

2.1 Maxwell's equations 12
2.2 Boundary conditions 13
2.3 Auxiliary potentials 15
2.4 Green's function 16
2.5 Integral equation 17
2.6 Method of Moments 20

Chapter 3 IMPEDANCE MATRIX GENERATION BY USING THE FAST MATRIX GENERATION (FMG) TECHNIQUE 22

3.1 Introduction 22
3.2 Theory and algorithm 24
3.2.1 Closed-form Green's function 26
3.2.2 Mixed-Potential Integral Equation (MPIE) and the Method of Moments 28
3.2.3 Fast matrix generation: Method-1 33
3.2.4 Fast matrix generation: Method-2 43
3.3 Numerical results 50
3.3.1 Bandpass filter 50
3.3.2 Four-pole elliptic bandpass filter 55
3.3.3 Rectangular resonator 59
3.4 Conclusions 63

Chapter 4 EFFICIENT IMPEDANCE MATRIX INTERPOLATION TECHNIQUE FOR THE ANALYSIS OF PRINTED LAYERED STRUCTURE 65

4.1 Introduction 65
4.2 Theory and algorithm 67

4.2.1 Integral equation and the method of moments (MoM) 68
4.2.2 Interpolation algorithm 70
4.3 Numerical results 81
4.3.1 Microstrip patch antenna 81
4.3.2 Interdigital bandpass filter 84
4.3.3 Hairpin bandpass filter 88
4.3.4 Proximity couple patch 92
4.4 Conclusions 96

Chapter 5 CHARACTERISTIC BASIS FUNCTION METHOD (CBFM) 97

5.1 Introduction 97
5.2 Theory and algorithm 100
5.2.1 Introduction to Characteristic Basis Function Method (CBFM) 100
5.2.2 Generation of CBFs 101
5.2.3 Thresholding the secondary CBFs 104
5.2.4 Construction of reduced matrix and its solution 105
5.3 Numerical results 107
5.3.1 Meander line 108
5.3.2 Bandpass filter 115
5.3.3 Two-stage amplifier 119
5.4 Conclusions 124

Chapter 6 A NOVEL TECHNIQUE FOR ITERATIVE SOLUTION OF MATRIX EQUATION ARISING IN THE METHOD OF MOMENTS FORMULATION 125

6.1 Introduction 125
6.2 Theory and algorithm 126
6.3 Numerical results 129
6.3.1 Four-element microstrip patch array 129
6.3.2 Two-element proximity-coupled patch array 133
6.4 Conclusion 136

Chapter 7 CONCLUSIONS AND FUTURE WORK 137

Bibliography 141

LIST OF FIGURES

Fig. **1.1**: Block diagram illustrating the MoM process and associated techniques proposed. 11

Fig. **2.1**: Boundary between two layers 13

Fig. **2.2**: Geometry of general layered structure 18

Fig. **3.1**: Original Sommerfeld integration path (SIP) and its deformed version in the spectral domain. 27

Fig. **3.2**: x-directed rooftop basis function for current and associated charge density. 30

Fig. **3.3**: Surface current of a conductor modeled by the rooftop basis functions. 30

Fig. **3.4**: Basis and testing function pair with a separation distance r 33

Fig. **3.5**: Example of a printed layered structure for impedance matrix comparison. 37

Fig. **3.6**: Geometry for the impedance matrix element comparison for the interaction between basis and testing functions both in x-direction. 39

Fig. **3.7**: (a) Impedance matrix comparison for the *xx* interaction generated by the rigorous and FMG-1 methods. (b) Relative difference between the matrix elements generated by these two methods. 40

Fig. **3.8**: Geometry for the impedance matrix element comparison for the interaction between basis and testing functions in x- and y-directions, respectively. 41

Fig. **3.9**: Impedance matrix comparison for the *xy* interaction generated by the rigorous and FMG-1 methods. (b) Relative difference between the matrix elements generated by these two methods. 42

Fig. **3.10**: A pair of basis and testing functions with their equivalent dipole moments and key parameters indicated. 43

Fig. **3.11**: Arrangement of basis and testing function for calculating $Z_{\rho,ref}(\rho)$ and their equivalent dipoles. 45

Fig. **3.12**: Arrangement of basis and testing functions for computing $Z_{\phi,ref}(\rho)$ and their equivalent dipole moments. 46

Fig. **3.13**: (a) Impedance matrix comparison for the *xx* interaction generated by the rigorous and the FMG-2 methods. (b) Relative difference between the matrix elements generated by these two methods. 48

Fig. **3.14**: (a) Impedance matrix comparison for the *xy* interaction generated by the rigorous and FMG-2 methods. (b) Relative difference between the matrix elements generated by these two methods. 49

Fig. **3.15**: Geometry of the bandpass filter: (a) entire geometry. (b) One-half of the geometry with the definitions of the relevant geometrical parameters. 52

Fig. **3.16**: Comparison of the S-parameters for the bandpass filter derived by using the rigorous and FMG-1 methods: (a) S_{11} ; (b) S_{21}. 53

Fig. **3.17**: Comparison of the S-parameters for the bandpass filter derived by using the rigorous and FMG-2 methods: (a) S_{11} ; (b) S_{21}. 54

Fig. **3.18**: Geometry of the four-pole elliptic bandpass filter. 56

Fig. **3.19**: Comparison of the S-parameters of a four-pole elliptic bandpass filter, derived by using the rigorous and FMG-1 methods: (a) S_{11} ; (b) S_{21}. 57

Fig. **3.20**: Comparison of the S-parameters of a four-pole elliptic bandpass filter, derived by using the rigorous and FMG-2 methods: (a) S_{11} ; (b) S_{21}. 58

Fig. **3.21**: Geometry of a rectangular resonator. 60

Fig. **3.22**: Comparison of the S-parameters of a rectangular resonator, derived by using the rigorous and FMG-1 methods: (a) S_{11} ; (b) S_{21}. 61

Fig. **3.23**: Comparison of the S-parameters of a rectangular resonator, derived by using the rigorous and FMG-2 methods: (a) S_{11} ; (b) S_{21}. 62

Fig. **4.1**: Geometry of a patch antenna fed by a microstrip line. 77

Fig. **4.2**: Comparison of impedance matrix element derived by using the direct and interpolation methods ($\rho = 0\,mm$). (a) real part; (b) imaginary part. 78

Fig. **4.3**: Comparison of impedance matrix elements derived by using the direct and interpolation methods ($\rho = 20\,mm$). (a) real part; (b) imaginary part. 79

Fig. **4.4**: Comparison of impedance matrix elements derived by using the direct and interpolation methods ($\rho = 40\,mm$). (a) real part; (b) imaginary part. 80

Fig. **4.5**: Comparison of S_{11} derived by using the direct and interpolation methods. (a) magnitude; (b) phase. 83

Fig. **4.6**: Geometry of an interdigital bandpass filter. 85

Fig. **4.7**: Comparison of S-parameters derived by using direct and interpolation methods. (a) magnitude of S_{11}; (b) magnitude of S_{21}. 86

Fig. **4.8**: Comparison of S-parameters derived by using direct and interpolation methods. (a) phase of S_{11}; (b) phase of S_{21}. 87

Fig. **4.9**: Geometry of a hairpin bandpass filter. 89

Fig. **4.10**: Comparison of S-parameters derived by using direct and interpolation methods. (a) magnitude of S_{11}; (b) magnitude of S_{21}. 90

Fig. **4.11**: Comparison of S-parameters derived by using direct and interpolation methods. (a) phase of S_{11}; (b) phase of S_{21}. 91

Fig. **4.12**: Geometry of the proximity-coupled patch. 94

Fig. **4.13**: Comparison of S_{11} derived by using direct and interpolation methods. (a) magnitude; (b) phase. 95

Fig. **5.1**: Segmentation of the lowpass filter. Dotted lines and numbers indicate the borders between sections and the section numbers, respectively. 102

Fig. **5.2**: Block impedance matrix of the original problem. Diagonal matrix for section-i is extended, and this part is indicated by the shaded region. 103

Fig. **5.3**: Meander line. Dotted lines separate the sections. 108

Fig. **5.4**: Comparison of the S-parameters of the meander line calculated by using the CBFM and the direct method. Only primary CBFs were used. (a) Magnitude of S_{11}; (b) Magnitude of S_{12}. 111

Fig. **5.5**: Comparison of S-parameters of the meander line calculated by using the CBFM and direct method. Primary CBFs and all of the secondary CBFs were used. (a) Magnitude of S_{11}; (b) Magnitude of S_{12} 112

Fig. **5.6**: Comparison of the S-parameters of the meander line calculated by using the CBFM and the direct method. Primary CBFs and secondary CBFs with thresholding were used. (a) Magnitude of S_{11}; (b) Magnitude of S_{12}. 113

Fig. **5.7**: Number of the CBFs as functions of the frequency for the meander line, when different criteria are used. 114

Fig. **5.8**: Bandpass filter. (a) Entire bandpass filter geometry. (b) Designation of geometrical parameters. 116

Fig. **5.9**: Comparison of the S-parameters of the bandpass filter, computed by using the primary and secondary CBFs with thresholding, and the direct method. (a) Magnitude of S_{11}; (b) Magnitude of S_{12}. 117

Fig. **5.10**: Number of CBFs as functions of the frequency used to analyze the bandpass filter, when different thresholding criteria are used. 118

Fig. **5.11**: Passive components of a two-stage amplifier circuit. 120

Fig. **5.12**: Comparison of the S-parameters of the passive components of a two-stage amplifier circuit computed by the CBFM using the primary and the secondary CBFs with thresholding, and the direct method. (a) Magnitude of S_{13}; (b) Magnitude of S_{44}. 121

Fig. **5.13**: Comparison of the Gain of the entire two-stage amplifier circuit computed by using the CBFM and the conventional method. 122

Fig. **5.14**: Number of the CBFs as functions of the frequency for the two-stage amplifier circuit. 123

Fig. **6.1**: A four-element microstrip patch array antenna. 131

Fig. **6.2**: (a) Number of iterations needed to achieve 0.1 % residual error with the zero and extrapolated initial guesses. (b) S_{11} derived by the direct solution, and CG with the zero and extrapolated initial guesses. 132

Fig. **6.3**: A two-element microstrip patch antenna. 134

Fig. **6.4**: (a) Number of iterations needed to achieve 0.1 % residual error with the zero and extrapolated initial guesses. (b) S_{11} derived by the direct solution, and CG with the zero and extrapolated initial guesses. 135

LIST OF TABLES

Table 3-1: Comparison of the impedance matrix generation times for example problems (Pentium IV 3 GHz, 2 GByte RAM) 63

Table 4-1: Comparison of the impedance matrix generation times for sample problems (Pentium IV 2 GHz, 1 GByte RAM) 93

Table 5-1: Comparison of the total solve times for the meander line over the frequency band 9 GHz to 10.5 GHz, when different criteria are used. 114

Table 5-2: Comparison of the total solve times for the bandpass filter over the frequency band of 11 GHz to 13 GHz, between the CBFM using the primary and the secondary CBFs with thresholding, and the direct method. 118

Table 5-3: Comparison of the total solve times for simulating the passive component of a two-stage amplifier over the frequency band 8 GHz to 14 GHz, between the CBFM using the primary and the secondary CBFs with thresholding, and the direct method. 123

ACKNOWLEDGEMENTS

I am dedicating this thesis to my wife Chinkyung and my son Joseph, for their patience and constant support throughout my graduate studies. I would also like to thank my parents and parent-in-laws, for their patience, support and love throughout my graduate studies.

I am indebted to my adviser, Dr. Raj Mittra for his valuable guidance and support throughout the course of this research. I also thank my committee members, Drs. Douglas H. Werner, Lynn A. Carpenter and Michael T. Lanagan for patiently reviewing my thesis and administering the Comprehensive and Final Oral Examinations.

My special thanks go to my colleagues of the Electromagnetic Communication Laboratory at Penn State. I have benefited from our many discussions and the development of new ideas.

Chapter 1

INTRODUCTION

Over the years, the importance of modeling and simulation of RF and microwave circuits has grown due to the growth of the wireless communication industry, which in turn has spurred the development of sophisticated design and analysis tools. Although many of the existing microwave CAD tools are based on simplified circuit models because they are less time-consuming to apply, the full-wave field solver is gaining popularity because it yields more reliable results, especially at high frequencies.

Full-wave field solution techniques, such as the Finite Difference Time Domain (FDTD) method [1], the Finite Element Method (FEM) [2], and the Method of Moments (MoM) [3], are commonly used for the analysis of layered structures. Microwave passive circuits are mostly printed on layered substrates, and the current induced on the surface of the conductor is usually the unknown quantity that we solve for. As a consequence, the MoM has been the preferred technique for the analysis of layered structures since the problem domain only involves the conductor surfaces, provided the Green's function for the layered structure is employed. However, the use of the MoM also entails a series of computationally expensive processes, *viz*., the Green's function generation, impedance matrix filling, and the solution of the matrix equation, all of which can be resource-intensive in terms of CPU time and memory.

The generation of the spatial-domain Green's function starts with the formulation of the Green's function in the spectral domain, which is readily obtainable in an

analytical form for planar-layered structures. The time-consuming process of evaluating the Sommerfeld integral [4], required to evaluate the spatial-domain Green's function from the spectral-domain counterpart can be circumvented by employing the closed-form Green's function technique [5,6]. In this technique, the spectral-domain Green's function is first approximated by a linear combination of complex exponentials; then, a closed-form spatial-domain Green's function is obtained by performing Hankel transform analytically with the aid of the Sommerfeld identity. Since the derivation of the spatial-domain Green's function by using the closed-form Green's function technique involves only exponential approximation and analytical transform, the computational burden is significantly alleviated.

The matrix fill process is also a computationally intensive process in the MoM because it involves the evaluation of quadruple reaction integrals for each matrix element. Consequently, it imposes a severe computational burden when the number of unknowns N is large since the CPU time, as well as the memory requirement, grows as $O(N^2)$ [7].

In the past, different techniques have been proposed to speed up the impedance matrix generation process. In [8], quadruple integrals for the rooftop basis and testing functions are reduced to double integrals by reordering the former, and replacing the integral between the basis and testing functions by polynomials. Next we use analytical manipulations to also reduce the above double integrals. The spatial-domain Green's function, which is derived by using the closed-form Green's function technique, is approximated in terms of a Taylor series expansion, and the matrix elements for the rooftop basis and testing function are evaluated analytically in [9,10]. Alatan and Aksun

[11] approximated the Green's function for distances greater than a threshold via polynomials of the radial distance between the source and the field points, and carried out the reaction integrals involving rooftop basis and testing functions by using simple algebraic expressions. In [12], the possibility of replacing the integrals for the Green's functions – as well as for the potentials – by the products of these quantities at the centroids and the area of the triangular cells, was briefly mentioned in the context of the impedance matrix calculations involving the RWG basis and testing functions that are well separated. In [13], the electric field integrals for each cell are first replaced by values of the potential at the center of the cell multiplied by the area of the cell; the potential integrals are performed by using a parametric evaluation and interpolation.

Often the frequency response of the microwave circuits contain one or more resonances, a feature that requires the evaluation of the response over a large number of frequency points within a given frequency band, to capture the resonance behaviors accurately. In some cases, hundreds of frequency points can be involved in the analysis, and this demands a prohibitively large computation time. An approach for speeding up the impedance matrix generation over a frequency band is the impedance matrix interpolation, for which various techniques have been proposed in the past. In [17], Newman and Forrai have suggested an impedance matrix interpolation using three pre-calculated impedance matrices, and have applied it to the scattering analysis of a microstrip patch on a grounded dielectric slab. Later, Newman [18] improved this technique by using two different interpolation schemes for the imaginary parts of the matrix elements, depending on the separation distance between the source and the field points. In addition, the phase variation was factored out from the impedance matrix

element if the separation distance was large. Virga and Rahmat-Samii [19] have applied the technique in [18] to the analysis of personal communication antennas. In their follow-up paper [20], they have compared interpolation schemes for [Z] and [Y] matrices, showing that [Y] matrix interpolation is highly dependent upon the resonant characteristics of the structure. In [21] and [22], Barlevy and Rahmat-Samii have modified the algorithms in [19] and [20], and have applied them to FSS and EGB structures. Wei and Li [23] have employed the Pade approximation to interpolate the impedance matrix for the MoM part of the geometry in the MoM-PO method. However, the interpolation schemes in these papers have been examined only for structures in free space, except for [17], where simple quadratic interpolation has been used for real and imaginary parts of the impedance matrix. Recently, Yeo and Mittra [24] have proposed an interpolation technique for layered structures that employs different interpolation schemes, depending on the separation distance between the source and field points. However, the schemes described in [24] sometimes produce discrepancies between the matrix element computed by the direct and interpolation methods, even for the intermediate distance range; hence an accurate and robust algorithm for the analysis of general layered structures is still desirable.

The size of the MoM matrix grows very rapidly as the dimension of the circuit being modeled becomes large in terms of the wavelength. This can also occur when a fine mesh is used to model a complex structure accurately, which in turn places an inordinately heavy burden on the memory and CPU time requirements for the direct solution of the matrix equation, since they increase as $O\left(N^2\right)$ and $O\left(N^3\right)$, respectively, where N is the number of unknowns.

In the past, many researchers have attempted to reduce the complexity and accelerate the computational speed of the solution of the matrix equation. For instance, the Fast-Multipole Method (FMM) [29] has been proposed to reduce the computational cost of matrix-vector multiplication when using an iterative solver, though primarily for perfectly conducting objects. The impedance matrix localization (IML) method [30] for matrix sparsification has been developed, again for a limited class of scattering problems involving PEC bodies, to expedite matrix-vector multiplication. Wavelet transform [31] has also been used to yield sparse matrices that can be solved rapidly, although it is not as robust an approach as might be desirable.

Another emerging approach for efficient MoM analysis of a microstrip structure is based on the concept of segmentation or domain decomposition, for which several techniques have been proposed. For instance, in [32], the modified diakoptic theory [33], originally proposed for antenna problems, has secondarily been applied to microstrip structures, although its use has been relatively limited. The same is true for the diakoptic-theory-based Multilevel Moments Method (MMM) [34], which carries out an iterative basis function refinement to solve passive planar structure problems. The Subdomain Multilevel Approach (SMA), which utilizes the so-called Macro Basis Functions (MBFs) [35], is a novel technique for reducing the matrix size associated with large planar antenna array problems. However, the above methods attempt to correct the mutual coupling terms recursively to improve the convergence of the solution by defining the MBFs on basic blocks and then extending the procedure to groups of blocks in an iterative way.

Iterative techniques are often used for an efficient solution of large systems of linear equations arising from the MoM formulation, often in conjunction with efficient algorithms for matrix–vector multiplication. Although the use of the latter helps reduce the solution time considerably by reducing the time for each iteration, the overall time is governed by the number of iterations needed to achieve convergence. To accelerate convergence, one often turns to preconditioning, a topic that has been extensively covered in the literature [39–41], and is beyond the scope of this work. Another important topic that is seldom discussed in the literature is the choice of the initial guess that plays a significant role in determining the speed of convergence of an iterative procedure.

Numerous attempts have been made in the past [42] to derive a good guess for the solution via extrapolation (though not in the context of iteration), which is derived from the solutions at previous frequencies. The procedure outlined in [42] can be quite complex because it is necessary to first express the induced current in terms of a set of constituent waves that have their unique frequency behaviors that must be extrapolated individually. Although such an extrapolation approach has been successfully applied to a number of scattering problems – mostly two-dimensional in nature – the method is not as robust as desired for a general problem since there is no obvious way to split up the induced current into constituent waves that can be conveniently extrapolated as functions of frequency. Yet another strategy is to extrapolate the solutions derived at previous frequencies by using a polynomial fitting [43]. Although this approach is considerably more general than the one in [42], it, too, has difficulty in dealing with structures that exhibit a resonance behavior.

1.1 Research Objectives

In this thesis, we first propose a new and fast impedance matrix generation scheme called the Fast Matrix Generation (FMG) for the analysis of printed layered structures, which employs different impedance matrix generation strategies based on the separation distance between the basis and testing functions. In this method, conventional and rigorous numerical methods are still used for generating the impedance matrix elements that are associated with the near-field interactions, while a more efficient scheme is employed where the separation distance between basis and testing functions exceeds a threshold value. Since the above approach only requires simple arithmetic, such as addition and multiplication of the Green's function and the interpolated impedance matrix elements, it circumvents the need to evaluate the quadruple integrals as in conventional methods. Hence, the latter approach is faster than the rigorous method by orders of magnitude in computation time.

Second, we present a novel approach for the impedance matrix interpolation that can be readily incorporated into existing codes. For a frequency window, the impedance matrices are directly computed at selected frequencies, and the frequency variations of the matrix elements in the frequency window are modeled by interpolating polynomials. The coefficients of the interpolating polynomials are determined by using the above impedance matrices. For matrix elements associated with the near-region interaction, this procedure is directly applied, while the phase extraction is first performed before the application of the interpolation scheme for the interactions beyond this range. Since the computation of the impedance matrix only involves the evaluation of the interpolating

polynomials, significant timesaving can be achieved for the analysis of the layered structure over a wide frequency range. By employing this approach, the accuracy of the interpolation has been improved over previous works, which in turn has improved the accuracy of the final parameters of interest.

Next, an efficient technique for microstrip MMIC analysis, called the Characteristic Basis Function Method (CBFM), is described. In this method, the problem geometry is first segmented into sections, for which high-level basis functions, called the Characteristic Basis Functions (CBFs), aggregations of the conventional subdomain bases, are generated. These CBFs not only represent the unique electromagnetic characteristic of each section but also include the mutual coupling effects between different sections.

The CBFM is different from some of the other domain decomposition methods in several ways. First, in this method, the parasitic coupling is taken into account in a systematic and efficient manner by using the secondary CBFs, rather than via the use of iterative refinement. The application of the CBFM leads to a reduced matrix, which is much smaller than the original one, and this obviates the need for iterative solution of problems requiring a large number of unknowns. Second, unlike in [9], which aggregates upper-level bases of two adjacent sections to form a single basis, the CBFM approach defines the bases for each individual section, and this provides increased flexibility during the segmentation process.

Finally, we present a simple and efficient technique for generating the initial guess for the iterative solution of a large dense system of linear equations arising in the Method of Moments (MoM) formulation of layered structure problems. The proposed

approach involves estimation of the solution vector based on the solutions at previous frequencies. The computational time involved in generating the estimate is negligible when compared to that of the MoM matrix generation and iterative solution. We demonstrate the effectiveness of the proposed technique in accelerating the convergence of the iterative procedure via its application to the microstrip patch array antennas, and discuss the stopping criterion of the iteration procedure.

1.2 Outline of the Thesis

In Chapter 2, basic electromagnetic theories, along with the integral equation formulation and the method of moments (MoM), are presented for understanding the remainder of the thesis.

Chapter 3 presents details of the Fast Matrix Generation (FMG) technique, and verifies its effectiveness through several numerical examples to illustrate that a significant saving in computations time can be achieved without sacrificing the accuracy of the parameters of interest.

In Chapter 4, theoretical background and details of the impedance matrix interpolation algorithm are provided. Also, the criteria for choosing the sampling frequency step, as well as an appropriate threshold for the application of phase extraction, are outlined. The efficiency of this technique is demonstrated by showing the numerical results for a variety of sample problems.

Chapter 5 presents the CBFM method, including the concept of high-level basis functions, generation of the primary and secondary CBFs, and construction of the

reduced matrix. In addition, the criterion for thresholding the secondary CBFs, to include only those that represent dominant couplings between sections, is provided. Numerical results for several examples are given.

In Chapter 6, the iterative solution process by the conjugate-gradient (CG) method in conjunction with the extrapolated initial guess is presented. The effectiveness of the proposed technique in accelerating the convergence of the iterative procedure is demonstrated by applying this technique to microstrip patch array antennas

Finally, Chapter 7 presents a summary and conclusions of the research and suggestions for further development of the research presented in this thesis.

In Fig. **1.1**, the block diagram of the MoM process is illustrated with corresponding techniques proposed in this thesis to improve the numerical efficiency of each step.

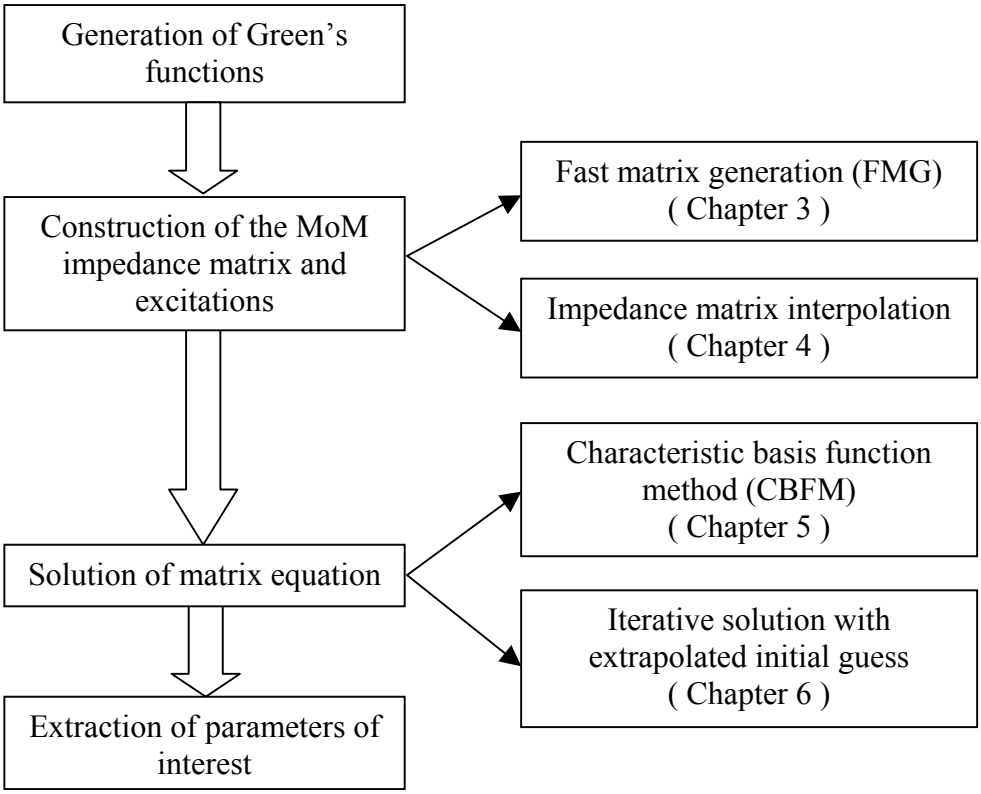

Fig. **1.1**: Block diagram illustrating the MoM process and associated techniques proposed.

Chapter 2

BASIC BACKGROUND FOR ELECTROMAGNETIC ANALYSIS OF PLANAR STRUCTURES

In this chapter, we provide the basic background needed to carry out a full-wave electromagnetic analysis of printed structures. We begin with the Maxwell's equations and briefly sketch the physical principles that govern the electromagnetic behavior of planar structures. This chapter then discusses the formulation of integral equation for the unknown induced currents, and the application of the Method of Moments (MoM) technique for the solution of these currents. The notations and definitions introduced in this chapter are used throughout this thesis.

2.1 Maxwell's equations

In the analysis of a planar-layered structure throughout this thesis, we will assume that the inhomogeneity exists only in the direction perpendicular to the layers and that the materials are homogeneous, and isotropic within each layer. Under these assumptions, the constitutive relations take the simple form

$$\mathbf{D} = \varepsilon \mathbf{E} \tag{2.1}$$

$$\mathbf{B} = \mu \mathbf{H} \tag{2.2}$$

where ε and μ are the permittivity and permeability of the layer, respectively. If the sinusoidal time dependence $e^{j\omega t}$ is suppressed, the Maxwell's equations for time-

harmonic fields in the presence of electric source $\mathbf{J}$ and magnetic source $\mathbf{M}$, either impressed and/or equivalent, are expressed as follows:

$$\nabla \times \mathbf{E} = -j\omega\mu\mathbf{H} - \mathbf{M} \tag{2.3}$$

$$\nabla \times \mathbf{H} = j\omega\varepsilon\mathbf{E} + \mathbf{J} \tag{2.4}$$

$$\nabla \cdot \mathbf{J} + j\omega\rho_e = 0 \tag{2.5}$$

$$\nabla \cdot \mathbf{M} + j\omega\rho_m = 0 \tag{2.6}$$

where ω is the angular frequency, $\mathbf{E}$ is the electric field intensity, $\mathbf{H}$ is the magnetic field intensity, $\mathbf{D}$ is the electric flux density, $\mathbf{B}$ is the magnetic flux density, and ρ_e and ρ_m are the electric and the magnetic charge density, respectively.

2.2 Boundary conditions

Consider a boundary between two materials having dissimilar electromagnetic properties as shown in Fig. 2.1. By applying Maxwell's equation to the boundary of

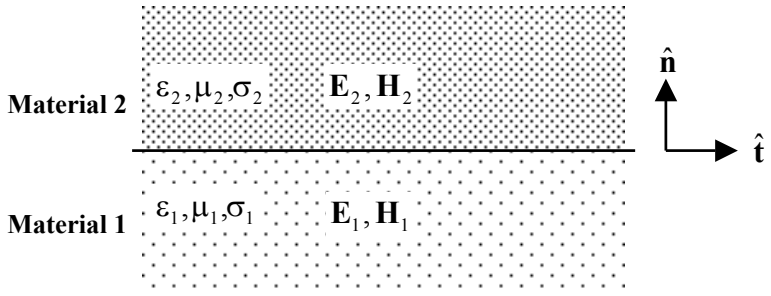

Fig. 2.1: Boundary between two layers

material discontinuity, we get the following relations:

$$\hat{\mathbf{n}} \cdot \left(\mathbf{B}_2 - \mathbf{B}_1\right) = \rho_m \tag{2.7}$$

$$\hat{\mathbf{n}} \cdot \left(\mathbf{D}_2 - \mathbf{D}_1\right) = \rho_e \tag{2.8}$$

$$\hat{\mathbf{n}} \times \left(\mathbf{E}_2 - \mathbf{E}_1\right) = -\mathbf{M} \tag{2.9}$$

$$\hat{\mathbf{n}} \times \left(\mathbf{H}_2 - \mathbf{H}_1\right) = \mathbf{J} \tag{2.10}$$

where $\hat{\mathbf{n}}$ and $\hat{\mathbf{t}}$ are outgoing vectors normal and tangential to the surface of the boundary. If there is no charge or current at the interface, (2.7-10) become

$$\mu_1 \mathbf{H}_1^{\perp} = \mu_2 \mathbf{H}_2^{\perp} \tag{2.11}$$

$$\mathbf{H}_1^{\parallel} = \mathbf{H}_2^{\parallel} \tag{2.12}$$

$$\varepsilon_1 \mathbf{E}_1^{\perp} = \varepsilon_2 \mathbf{E}_2^{\perp} \tag{2.13}$$

$$\mathbf{E}_1^{\parallel} = \mathbf{E}_2^{\parallel} \tag{2.14}$$

where $\perp$ refers to the component of the field perpendicular to the surface, while $\parallel$ refers to the component parallel to the surface. The tangential component of the electric field at the interface between a dielectric and a good conductor is of great importance in the analysis of a planar-layered structure. The tangential component of the electric field on the surface of the conductor is related to the electric current density by

$$\mathbf{E}_t = Z_s \mathbf{J}_s = (1 + j)\sqrt{\frac{\omega\mu}{2\sigma}}\mathbf{J}_s \tag{2.15}$$

where Z_s is the surface impedance of the conductor, $\mathbf{J}_s$ is the surface current and σ is the conductivity of the conductor. For the special case of a perfect electric conductor, $\sigma \to \infty$ and the tangential electric field vanishes on the surface.

2.3 Auxiliary potentials

In the analysis of electromagnetic boundary-value problems, it is common to use auxiliary vector potentials. We choose the magnetic vector potential $\mathbf{A}$ and the electric vector potential $\mathbf{F}$ for the analysis of the layered structures. In a source-free region, the magnetic flux density $\mathbf{B} = \mu\mathbf{H}$ is always solenoidal, that is $\nabla \cdot \mathbf{B} = 0$, and it can be represented as the curl of another vector quantity. Thus, a vector $\mathbf{A}$ can be defined, satisfying

$$\mathbf{B}_A = \mu\mathbf{H}_A = \nabla \times \mathbf{A} \tag{2.16}$$

where subscript $_A$ indicates the fields due to the $\mathbf{A}$ potential. By employing the *Lorentz condition*,

$$\nabla \cdot \mathbf{A} = -j\omega\mu\varepsilon\phi_e \tag{2.17}$$

$\mathbf{E}_A$ can be expressed as

$$\mathbf{E}_A = \frac{1}{j\omega\varepsilon}\nabla \times \mathbf{H}_A = \frac{1}{j\omega\varepsilon}\nabla \times \nabla \times \mathbf{A} \tag{2.18}$$

or

$$\mathbf{E}_A = -j\omega\mathbf{A} - \nabla\phi_e = -j\omega\left(\bar{\mathbf{I}} + \frac{1}{k^2}\nabla\nabla\right) \cdot \mathbf{A} \tag{2.19}$$

where ϕ_e the electric scalar potential, $k = \omega\sqrt{\mu\varepsilon}$ is the wavenumber and $\bar{\mathbf{I}}$ is the unit dyad. Analogously, in a source-free region, the electric flux density is always solenoidal and can be represented as the curl of another vector potential $\mathbf{F}$. Similar to the discussion

above, the fields due to the vector potential $\mathbf{F}$ (indicated by a subscript) in a homogeneous (or piecewise homogeneous) and source-free region can be written as

$$\mathbf{D}_F = \varepsilon \mathbf{E}_F = -\nabla \times \mathbf{F} \tag{2.20}$$

$$\mathbf{H}_F = -\frac{1}{j\omega\mu} \nabla \times \mathbf{E}_F = \frac{1}{j\omega\varepsilon\mu} \nabla \times \nabla \times \mathbf{F} \tag{2.21}$$

$$\mathbf{H}_F = -j\omega \mathbf{F} - \nabla \phi_m = -j\omega \left(\bar{\mathbf{I}} + \frac{1}{k^2} \nabla\nabla \right) \cdot \mathbf{F} \tag{2.22}$$

where ϕ_m is the magnetic scalar potential. Finally, the total field is obtained by the superposition of the individual fields due to the $\mathbf{A}$ and $\mathbf{F}$ vector potentials

$$\mathbf{E} = \mathbf{E}_A + \mathbf{E}_F = -j\omega \left(\bar{\mathbf{I}} + \frac{1}{k^2} \nabla\nabla \right) \cdot \mathbf{A} - \frac{1}{\varepsilon} \nabla \times \mathbf{F} \tag{2.23}$$

$$\mathbf{H} = \mathbf{H}_A + \mathbf{H}_F = \frac{1}{\mu} \nabla \times \mathbf{A} - j\omega \left(\bar{\mathbf{I}} + \frac{1}{k^2} \nabla\nabla \right) \cdot \mathbf{F} \tag{2.24}$$

2.4 Green's function

The auxiliary vector potentials $\mathbf{A}$ and $\mathbf{F}$ produced by (impressed or equivalent) volume or surface currents radiating into a homogeneous medium of permittivity ε and permeability μ must satisfy the wave equations

$$\nabla^2 \mathbf{A} + k^2 \mathbf{A} = -\mu \mathbf{J} \tag{2.25}$$

$$\nabla^2 \mathbf{F} + k^2 \mathbf{F} = -\varepsilon \mathbf{M} \tag{2.26}$$

The above equation can be separated into three scalar wave equations that take the form

$$\nabla^2 \varphi + k^2 \varphi = s \tag{2.27}$$

where s is the source term for the scalar component φ. The Green's function of a partial differential equation is defined as the solution of the equation for a point source

$$\nabla^2 g(r,r') + k^2 g(r,r') = -\delta(r-r') \tag{2.28}$$

where $g(r,r')$ is the Green's function, and $\delta(r-r')$ is a point source located at r'. Once the Green's function has been found, φ can be easily obtained from the principle of linear superposition, since $g(r,r')$ is the solution for a point source.

$$\varphi(r) = -\int g(r,r')s(r')dr' \tag{2.29}$$

For an unbounded and homogeneous medium, the Green's function satisfying equation (2.28) is easily found to be

$$g(r,r') = \frac{e^{-jk|r-r'|}}{4\pi|r-r'|} \tag{2.30}$$

2.5 Integral equation

The integral equation (IE) technique has been widely used to solve electromagnetic problems in which a partial differential equation is cast into an integral equation whose integrand includes the Green's function and the unknown quantity. The integral equation formulation starts with the representation of the fields as a linear superposition of the fields produced by a point source, followed by the imposition of the appropriate boundary conditions, depending on the geometry and the material parameters of the medium. The electric field integral equation, in which the electric field is expressed by the convolution of the Green's function and the unknown current distribution, is the

most common way of formulating the problem involving printed conductors in a layered structure.

The total tangential electric field on the surface of a conductor is related to the surface impedance and the current on the conductor, introduced in the previous section.

$$\mathbf{E}_t(r) = Z_s \mathbf{J}_s(r) \tag{2.31}$$

The total electric field is the sum of the impressed and the scattered fields, the later being produced by the induced current, *i.e.*,

$$\mathbf{E}_i(r) + \mathbf{E}_s(r) = Z_s \mathbf{J}_s(r) \tag{2.32}$$

From (2.19) and the definition of the *Lorentz gauge*, the scattered field can be written

$$\mathbf{E}_s(r) = -j\omega\mathbf{A} - \nabla\phi = -j\omega\left(\bar{\mathbf{I}} + \frac{1}{k^2}\nabla\nabla\right)\cdot\mathbf{A} \tag{2.33}$$

The vector potential is expressed in terms of the vector potential Green's function, which

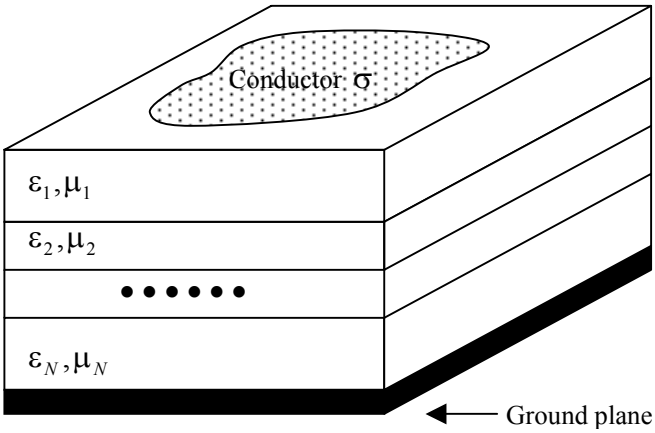

Fig. 2.2: Geometry of general layered structure

is defined as the vector potential induced by the point current source, and the current

$$\mathbf{A} = \int \overline{\mathbf{G}}_A(r, r') \cdot \mathbf{J}_s(r') dr' \qquad (2.34)$$

where $\overline{\mathbf{G}}_A(r, r')$ is the dyadic Green's function for vector potential $\mathbf{A}$. By substituting (2.34) into (2.33), the scattered electric field is represented as an integral equation involving the dyadic Green's function for $\mathbf{A}$, as follows:

$$\mathbf{E}_s(r) = -j\omega \int \overline{\mathbf{G}}_A(r, r') \cdot \mathbf{J}_s(r') dr' - \frac{j\omega}{k^2} \nabla \int \left[\nabla \cdot \overline{\mathbf{G}}_A(r, r')\right] \cdot \mathbf{J}_s(r') dr' \qquad (2.35)$$

Substituting (2.35) into (2.32) yields a new equation, in which the electric field is expressed in terms of vector potential Green's function and the unknown current distribution.

$$\mathbf{E}_i(r) = j\omega \int \overline{\mathbf{G}}_A(r, r') \cdot \mathbf{J}_s(r') dr' - \frac{j\omega}{k^2} \nabla \int \left[\nabla \cdot \overline{\mathbf{G}}_A(r, r')\right] \cdot \mathbf{J}_s(r') dr' + Z_s \mathbf{J}_s(r) \qquad (2.36)$$

The Mixed-Potential Integral Equation (MPIE) is used throughout this thesis because the singularity of potentials is of lower order than those for the fields (r^{-1} instead of r^{-3}), which makes the numerical computation of the reaction integrals more accurate than if we dealt with the fields instead. Using the relation (See [15])

$$\frac{j\omega}{k^2} \nabla \cdot \overline{\mathbf{G}}_A(r, r') = \frac{1}{j\omega} \nabla' G_\phi(r, r') \qquad (2.37)$$

where G_ϕ is the scalar potential Green's function, the second integral on the right-hand side of (2.36) can be written

$$\frac{j\omega}{k^2} \nabla \int \left[\nabla \cdot \overline{\mathbf{G}}_A(r, r')\right] \cdot \mathbf{J}_s(r') dr' = \frac{1}{j\omega} \nabla \int G_\phi(r, r') \nabla' \cdot \mathbf{J}_s(r') dr' \qquad (2.38)$$

with the assumption that the current either vanishes on the perimeter of the surface of the conductor or is perpendicular to the normal vector. Using (2.38), (2.36) can be written

$$\mathbf{E}_i(r) = j\omega\int \overline{\mathbf{G}}_A(r,r')\cdot\mathbf{J}_s(r')dr' - \frac{1}{j\omega}\nabla\int G_\phi(r,r')\nabla'\cdot\mathbf{J}_s(r')dr' + Z_s\mathbf{J}_s(r) \qquad (2.39)$$

Note that the divergence operator is cast inside the integral and directly operating on the current, thus reducing the singularity of the Green's function. For a perfect electric conductor, (2.39) can be reduced to

$$\mathbf{E}_i(r) = j\omega\int \overline{\mathbf{G}}_A(r,r')\cdot\mathbf{J}_s(r')dr' - \frac{1}{j\omega}\nabla\int G_\phi(r,r')\nabla'\cdot\mathbf{J}_s(r')dr' \qquad (2.40)$$

2.6 Method of Moments

Consider a linear system, for instance, the integral equation (2.40), which can be written in the following form:

$$Lf = g \qquad (2.41)$$

where L is a linear operator, which is an integral for IE formulation, and g is a known function and f is the unknown function to be determined. To solve the equation numerically, the unknown function is approximated by the superposition of known functions, called the basis functions, as follows

$$f = \sum_{j=1}^{N}\alpha_j f_j \qquad (2.42)$$

where N is the number of basis functions, α_j's are the coefficients to be determined, and f_j's are the basis functions. By substituting (**2.42**) into (**2.41**), the following expression is obtained:

$$\sum_{j=1}^{N} \alpha_j L f_j = g \tag{2.43}$$

To transform (**2.43**) into a matrix equation, we take the inner product of (**2.43**) with a set of suitable functions called the testing or weighting functions, to get

$$\sum_{j=1}^{N} \alpha_j \langle w_i, L f_j \rangle = \langle w_i, g \rangle \qquad i = 1,2,3,\cdots,N \tag{2.44}$$

where w_i's are the testing functions. The original equation (**2.41**) is finally cast into a linear matrix equation in the following form:

$$\begin{bmatrix} \langle w_1, Lf_1 \rangle & \langle w_1, Lf_2 \rangle & \cdots & \langle w_1, Lf_N \rangle \\ \langle w_2, Lf_1 \rangle & \langle w_2, Lf_2 \rangle & \cdots & \langle w_2, Lf_N \rangle \\ \vdots & \vdots & \ddots & \vdots \\ \langle w_N, Lf_1 \rangle & \langle w_N, Lf_2 \rangle & \cdots & \langle w_N, Lf_N \rangle \end{bmatrix} \begin{bmatrix} \alpha_1 \\ \alpha_2 \\ \vdots \\ \alpha_N \end{bmatrix} = \begin{bmatrix} \langle w_1, g \rangle \\ \langle w_2, g \rangle \\ \vdots \\ \langle w_N, g \rangle \end{bmatrix} \tag{2.45}$$

In a simpler notation, (**2.45**) can be written as

$$[\mathbf{Z}][\mathbf{I}] = [\mathbf{V}] \tag{2.46}$$

where $z_{i,j} = \langle w_i, L f_j \rangle$, $i_i = \alpha_i$ and $v_i = \langle w_i, g \rangle$. Equation (**2.46**) can be solved for the coefficients by using various techniques for solving linear matrix equations, such as the direct method and the iterative method.

Chapter 3

IMPEDANCE MATRIX GENERATION BY USING THE FAST MATRIX GENERATION (FMG) TECHNIQUE

3.1 Introduction

The analysis of a printed layered structure via the electric field integral equation (EFIE) technique applied in conjunction with the Method of Moments (MoM) involves a series of numerical procedures, including derivation of the spatial-domain Green's function, the generation of an impedance matrix, and the solution of a matrix equation.

The spatial-domain Green's function is given in the form of the Fourier integral of its spectral-domain counterpart, which is readily obtainable in an analytical form for planar-layered structures. The evaluation of this Fourier integral, also known as the Sommerfeld integral [4], is a time-consuming task since it involves the integration of a complex, oscillatory, and slowly decaying function over an infinite domain, and has thus been a computational bottleneck in the spatial-domain MoM technique. Recently, a new approach called the closed-form Green's function [5,6] was proposed to accelerate the derivation of the spatial-domain Green's function. In this technique, the spectral-domain Green's function is first approximated by a linear combination of complex exponentials; then, a closed-form spatial-domain Green's function is obtained by performing Hankel transform analytically with the aid of the Sommerfeld identity. Since the derivation of the spatial-domain Green's function by using the closed-form Green's function technique involves only exponential approximation and analytical transform – as opposed to

extensive integration over an infinite range – the computational burden is significantly alleviated.

The matrix fill process is also a computationally intensive process in the MoM, because it involves the evaluation of quadruple reaction integrals between each combination of basis and testing functions. Since the CPU time as well as the memory requirement grow as $O(N^2)$ [7], where N is the number of unknowns, a substantial portion of the CPU time in the MoM analysis of the printed layered structure is associated with this step for problems with a large number of unknowns. In the past, different techniques have been proposed to speed up the impedance matrix generation process. In [8], quadruple integrals for rooftop basis and testing functions are reduced to double integrals by reordering the integrals and introducing the correlation function between the basis and testing functions. These double integrals are subsequently reduced to single ones by using analytical manipulations. The above technique is further improved in [9,10], by approximating the spatial-domain Green's function in terms of a Taylor series expansion and involving only the analytical evaluation of double integrals. Alatan and Aksun [11] approximated the Green's function for distances greater than a threshold via polynomials of the radial distance between the source and the field points, and carried out the reaction integrals involving rooftop basis and testing functions by using simple algebraic expressions. In [12], the possibility of replacing the integrals for the Green's functions as well as the potentials, by the products of these quantities at the centroids, and the area of the triangular cells was briefly mentioned in the context of the impedance matrix calculations involving the RWG basis and testing functions that are separated by a considerable distance. In [13], the electric field integrals for each cell are

first replaced by the potential values at the center of the cell multiplied by the area of the cell; the potential integrals are performed by using a parametric evaluation and interpolation.

In this chapter, we propose a new and fast impedance matrix generation scheme, called the Fast Matrix Generation (FMG), for the analysis of printed layered structures that employs different impedance matrix generation strategies based on the separation distance between the basis and testing functions. In this method, conventional and rigorous numerical methods are still used for generating the impedance matrix elements that are associated with the near-field interactions, while a more efficient scheme is employed where the separation distance between basis and testing functions exceeds a threshold value. Since the above approach only requires simple arithmetic operations, such as addition and multiplication of the Green's function and the interpolated impedance matrix elements, it circumvents the need to evaluate the quadruple integrals as in the conventional methods. Hence, the latter approach is faster than the rigorous method by orders of magnitude in computation time.

The following sections present the details of this technique, and verify its effectiveness via several numerical examples that illustrate the fact that a significant timesaving can be achieved without sacrificing the accuracy of the parameters of interest.

3.2 Theory and algorithm

The integral equation formulation, employed in conjunction with the Method of Moments, has been the most widely used full-wave technique for the analysis of printed

layered structures, and has been successfully applied to a wide variety of problems. The first step in this approach is to construct an electric field integral equation by expressing the electric field as a convolution integral involving the surface current and the electric field Green's function. However, it is well known that the electric field Green's function has a highly singular spatial dependence, varying as r^{-3} where r is the separation distance between the source and the field points. This behavior makes it very difficult to accurately evaluate the impedance matrix element when the distance between the field and the source points is relatively small. The Mixed-Potential Integral Equation (MPIE) [14,15] has been used as an alternative to EFIE to alleviate the problem mentioned above. In the MPIE, the contributions to the electric field from a current source are separated into two parts, *viz.,* one attributable to the magnetic vector potential and the other to the scalar potential, respectively, and this serves to reduce the singular behavior of the Green's function from r^{-3} to r^{-1} in the process.

After formulating the MPIE, the unknown induced current is expanded as a superposition of suitable basis functions and their weight coefficients are next determined from the solution of the integral equation. Towards this end, the Galerkin method is applied by taking the inner products of the electric field with the same set of functions as those used for the basis functions, and this transforms the original integral equation into a matrix equation. The next step is to determine the unknown coefficients by applying the matrix equation solution techniques, such as a direct or an iterative procedure, depending upon the nature of the problem. Finally, the desired results, *e.g*., the [S] parameters, are computed from the solution of the matrix equation to complete the process.

In the following sections, the derivation of the closed-form Green's function is outlined; next, the formulation of the MPIE is presented; and, finally, the details of the FMG technique are discussed.

3.2.1 Closed-form Green's function

In the MPIE technique for printed layered structure, both the vector and scalar potential Green's functions are required, and it is necessary to derive a specific set of Green's functions prior to formulating the integral equation. Among the possible sets of Green's functions that may be used for this purpose, the traditional choice, namely one based on the Sommerfeld's formulation in [16], is the preferred one, and will be used in this thesis. For the vector potential, this Green's function takes the form

$$\overline{\mathbf{G}}_A = (\hat{x}\hat{x} + \hat{y}\hat{y})G_{xx}^A + \hat{z}\hat{x}G_{zx}^A + \hat{x}\hat{y}G_{xy}^A + \hat{z}\hat{z}G_{zz}^A \qquad (3.1)$$

Two other scalar potentials, *viz.*, G_x^q and G_z^q, are needed to supplement $\overline{\mathbf{G}}_A$ for the horizontal and vertical sources, respectively. The derivation of the spatial-domain Green's function for a printed layered structure involves time-consuming evaluation of Fourier integrals containing oscillatory and slowly decaying functions. The use of the closed-form Green's function technique [5,6] helps expedite the calculation of the spatial-domain Green's function quite significantly. In this technique, the spectral-domain Green's function is sampled along an integration path of the Hankel transform that is deformed from the original path of the Sommerfeld integration (See Fig. 3.1), and then

approximated in terms of complex exponentials using techniques such as Prony's or the generalized pencil-of-function (GPOF) method, in the form

$$\widetilde{G}_{A,\phi} \cong \sum_{i=1}^{M} a_i e^{-b_i k_z} \tag{3.2}$$

where N is the number of exponential terms. The spatial-domain Green's function is obtained from its spectral-domain counterpart via a Hankel transform, and the final form of the closed-form spatial-domain Green's function is written as

$$G_{A,\phi} \cong \sum_{i=1}^{N} a_i \frac{e^{-jkr_i}}{r_i} \tag{3.3}$$

where $r_i = \sqrt{x^2 + y^2 - b_i^2}$ and k is the propagation constant. The MPIE is derived and solved by using the Method of Moments technique, once the Green's functions mentioned above have been calculated.

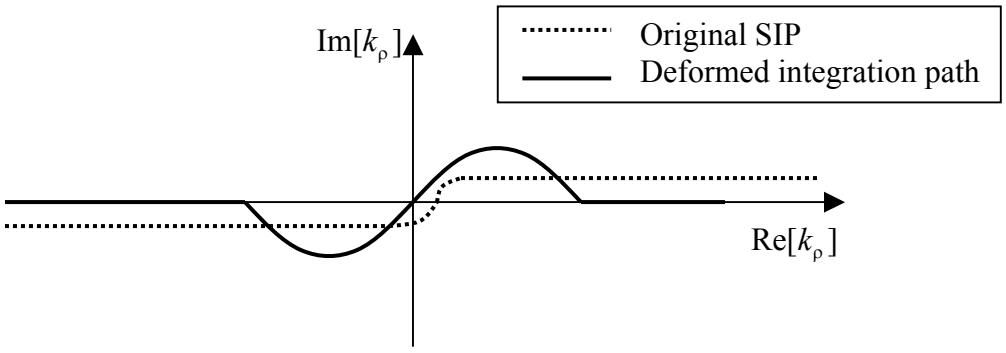

Fig. **3.1**: Original Sommerfeld integration path (SIP) and its deformed version in the spectral domain.

3.2.2 Mixed-Potential Integral Equation (MPIE) and the Method of Moments

The first step in the formulation of the electric field MPIE for a printed layered structure is the imposition of the boundary condition on the surface of the printed conductors

$$\mathbf{E}_t(r) = \mathbf{E}_i(r) + \mathbf{E}_s(r) = Z_s \mathbf{J}(r) \tag{3.4}$$

where $\mathbf{E}_t(r)$ is the total tangential electric field; $\mathbf{E}_i(r)$ and $\mathbf{E}_s(r)$ are the incident and scattered electric fields, respectively; $\mathbf{J}(r)$ is the induced current on the surface of conductor; and, Z_s is the surface impedance as defined in Chapter 2. If we assume that the conductor has an infinite conductivity, the tangential electric field vanishes on the surface of the conductor, leading to the equation

$$\mathbf{E}_i(r) = j\omega \int \overline{\mathbf{G}}_A(r,r') \cdot \mathbf{J}(r') dr' - \frac{1}{j\omega} \nabla \int G_\phi(r,r') \nabla' \cdot \mathbf{J}(r') dr' \tag{3.5}$$

where $\overline{\mathbf{G}}_A(r,r')$ and $G_\phi(r,r')$ are the dyadic vector and scalar potential Green's functions, respectively. The current in (3.5) can be expanded as a linear combination of known basis functions as follows:

$$\mathbf{J}(r) = \sum_{q=1}^{N} \alpha_q \mathbf{B}_q(r') \tag{3.6}$$

where N is the total number of the basis function; α_q is the coefficient to be determined by solving the equation; and, $\mathbf{B}_q(r')$ is the basis function. Substituting (3.6) in (3.5) yields

$$\mathbf{E}_i(r) = j\omega \sum_{q=1}^{N} \alpha_q \int \overline{\mathbf{G}}_A(r,r') \cdot \mathbf{B}_q(r') dr' - \frac{1}{j\omega} \sum_{q=1}^{N} \alpha_q \nabla \int G_\phi(r,r') \nabla' \cdot \mathbf{B}_q(r') dr' \tag{3.7}$$

One of the most commonly used subdomain basis function for the analysis of printed layered structures is the rooftop, which has a triangular behavior in the longitudinal direction and is a constant in the transverse direction (See Fig. **3.2**). The current J_i on the positive and negative rectangular cells C_i^+ and C_i^-, is modeled by using a rooftop function, and the charge q_i associated with this current is represented by a pulse doublet. The explicit form of a rooftop function in x direction, for instance, is expressed separately in x- and y-directions as

$$B_x(x)=\begin{cases}1-\dfrac{|x|}{l^+} & -l^+ < x < 0\\ 1-\dfrac{|x|}{l^-} & 0 < x < l^-\\ 0 & otherwise\end{cases} \qquad (3.8)$$

$$B_x(y)=\begin{cases}\dfrac{1}{w} & 0 < y < w\\ 0 & otherwise\end{cases}$$

The charge associated with the rooftop basis function is readily derived using the relation $q_i = -j\omega\nabla\cdot\mathbf{J}_i$. Also, the definitions for the rooftop basis functions in y- and z-directions are defined in an analogous manner. When using the rooftop basis function, a geometry is first partitioned into rectangular cells, and the current on each cell is modeled as a superposition of overlapped rooftop functions, as illustrated in Fig. **3.3**. Since there is no normal component of the current along the boundary of the rooftop basis function, no line charge is accumulated along the boundary of the rooftop function. After the current is expanded in terms of the basis functions, the Galerkin process is applied by performing the inner products between the electric field and the testing functions.

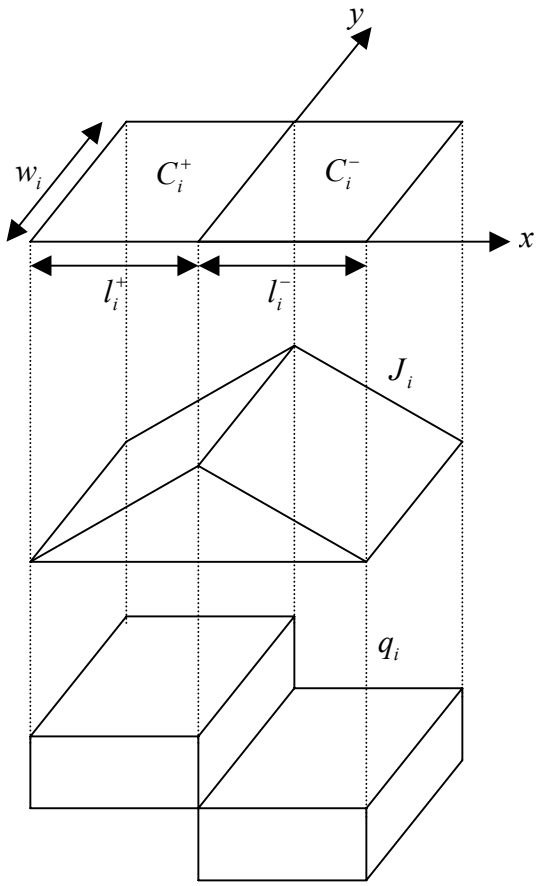

Fig. **3.2**: x-directed rooftop basis function for current and associated charge density.

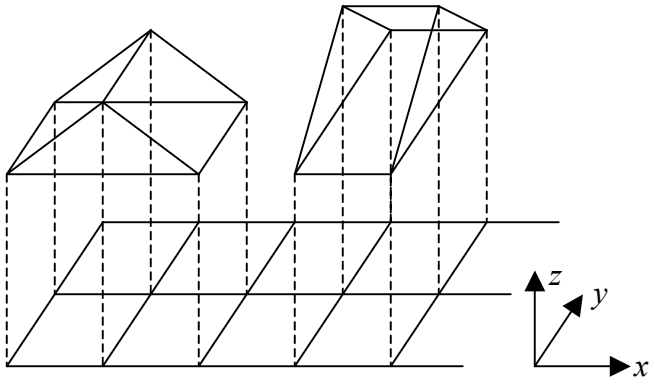

Fig. **3.3**: Surface current of a conductor modeled by the rooftop basis functions.

This process transforms the original integral equation into a linear system of equations, which can be expressed in a matrix notation as

$$[\mathbf{Z}][\mathbf{I}] = [\mathbf{V}] \tag{3.9}$$

where $[\mathbf{Z}]$ is the $N \times N$ impedance matrix, $[\mathbf{I}]$ is the $N \times 1$ current coefficient vector, and $[\mathbf{V}]$ is the $N \times 1$ excitation vector. The entries of the impedance matrix are written as

$$z_{p,q} = j\omega \left\langle \mathbf{T}_p(r), \int \overline{\mathbf{G}}_A(r,r') \cdot \mathbf{B}_q(r') dr' \right\rangle - \frac{1}{j\omega} \left\langle \mathbf{T}_p(r), \nabla \int G_\phi(r,r') \nabla' \cdot \mathbf{B}_q(r') dr' \right\rangle \tag{3.10}$$

where $z_{p,q}$ denotes the impedance matrix element for the interaction between the basis and testing functions with indices q and p, respectively.

The filling of the impedance matrix for problems involving printed layered structures is a computationally expensive process, since the calculation of an impedance matrix element requires the evaluation of quadruple integrals, and the process has to be repeated for each of the basis/testing function pairs. To compute the impedance matrix elements that represent the couplings between the rooftop basis and testing functions, the original quadruple integrals are reduced to double integrals by changing the order of the integrations, and replacing the double integrals – which involves the basis and the testing functions – with the correlation function between these two functions [9]. If, for instance, this process is applied to the impedance matrix element for the x-directional basis and testing functions, the first inner product in (3.10), which is a quadruple integral, can be simplified as follows:

$$\left\langle \mathbf{T}_p(r), \int \overline{\mathbf{G}}_A(r,r') \cdot \mathbf{B}_q(r') dr' \right\rangle = \int\int G_{xx}^A(u,v) f(u) g(v) du dv \tag{3.11}$$

where $f(u)$ and $g(v)$ are the polynomials representing the correlation function between the basis and the testing functions. The second inner product in (**3.10**), which is related to the scalar potential, can be simplified similarly. Since the quadruple integrals are reduced to double integrals, and the correlation function between the basis and testing functions can be calculated analytically in a very short time, considerable computation time can thus be saved by employing this method. However, even with the application of this technique, the impedance matrix filling is a time-consuming task. Therefore, it is desirable to devise a way to further improve the efficiency of this process. This is especially true when the field point is in the vicinity of the source point, and a numerically intensive process is required to accurately evaluate the reaction integrals for the impedance matrix elements owing to the singularity of the Green's function at the source point. However, the Green's function behavior becomes very smooth with an increase in the separation distance between the field and source points. This, in turn, makes it possible to employ an efficient and faster impedance matrix generation scheme as outlined below.

We now present a new and efficient impedance matrix generation algorithm, called the Fast Matrix Generation (FMG) scheme, in which we employ tailored matrix generation schemes that depend on the separation distance r, measured from the center point of the basis function to that of the testing function, as shown in Fig. **3.4**. The FMG algorithm employs a rigorous method, such as a high-order numerical quadrature, to compute the impedance matrix elements when the separation distance between the basis

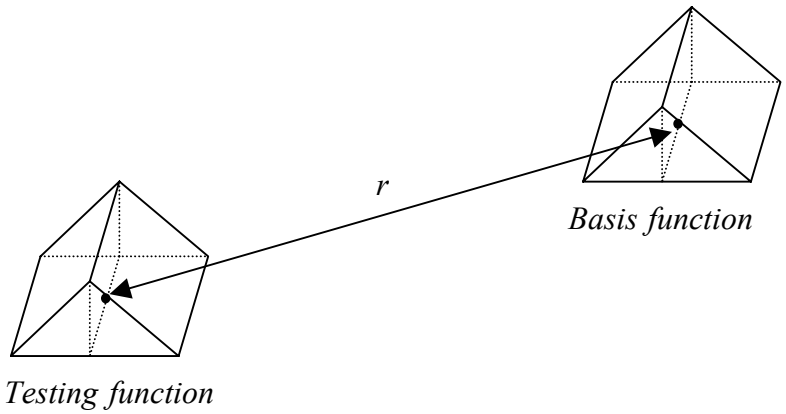

Fig. 3.4: Basis and testing function pair with a separation distance r.

and testing function is smaller than a threshold value r_0, while two fast and efficient schemes are used for the generation of the remaining matrix elements.

In the following sections, the procedures describing these methods are detailed; the guideline for determining the threshold is outlined; and their effectiveness is demonstrated by presenting the simulation results for several example problems.

3.2.3 Fast matrix generation: Method-1

To illustrate the algorithm, we first return to the formulation for the impedance matrix element for the case where both the basis and testing functions are oriented in the x-direction, and express it as

$$Z = -j\omega\langle \mathbf{T}, \mathbf{A} \rangle - \langle \mathbf{T}, \nabla\phi \rangle \qquad (3.12)$$

where A and ϕ are the magnetic vector and scalar potentials, respectively. For the sake of brevity of notation, the indices associated with the basis and testing functions have been omitted in the above representation. Equation (**3.12**) is an alternative form of (**3.10**), obtained by replacing the potential integrals with the vector and scalar potentials. The first inner product in (**3.12**), which represents the contribution of the vector potential, is written

$$\langle \mathbf{T}, \mathbf{A} \rangle = \iint_{\Omega_T} \mathbf{T}(r) \cdot \mathbf{A}(r) dr \tag{3.13}$$

where Ω_T is the surfaces of the testing function. If the separation distance between the basis and testing functions is large, the Green's function behaves very smoothly within the range of integration, as does the electric field. Then, by using the potential values at the centroids of each half of the testing function, we can rewrite (**3.13**) as

$$\langle \mathbf{T}, \mathbf{A} \rangle = \mathbf{A}\left(r_c^{T_+}\right) \cdot \iint_{\Omega_{T_+}} \mathbf{T}(r) dr + \mathbf{A}\left(r_c^{T_-}\right) \cdot \iint_{\Omega_{T_-}} \mathbf{T}(r) dr \tag{3.14}$$

where $r_c^{T_+}$ and $r_c^{T_-}$ are the centroids for the positive and negative halves of the testing function, respectively. Using the definition of the rooftop function and, carrying out the integration in (**3.14**), we get

$$\langle \mathbf{T}, \mathbf{A} \rangle = \frac{l_t^+}{2} A\left(r_c^{T_+}\right) + \frac{l_t^-}{2} A\left(r_c^{T_-}\right) \tag{3.15}$$

where $l_t^{\pm}$ is the length of positive/negative half of the testing function. Next, we calculate the vector potentials at the centroid of the positive half of the testing function to get:

$$A\left(r_c^{T_+}\right) = \iint_{\Omega_{B_+}} \mathbf{G}_A^{xx}\left(r_c^{T_+} - r'\right) \cdot \mathbf{B}(r') dr' + \iint_{\Omega_{B_-}} \mathbf{G}_A^{xx}\left(r_c^{T_+} - r'\right) \cdot \mathbf{B}(r') dr' \tag{3.16}$$

where Ω_{B_+} and Ω_{B_-} are the domains of the positive and negative halves of the basis function, respectively. Since the Green's function behaves very smoothly within the range of integration, (**3.16**) can be further simplified to:

$$A\left(r_c^{T_+}\right)=\frac{l_b^+}{2}G_A^{xx}\left(r_c^{T_+}-r_c^{B_+}\right)+\frac{l_b^-}{2}G_A^{xx}\left(r_c^{T_+}-r_c^{B_-}\right) \tag{3.17}$$

where $l_b^{\pm}$ is the length of the positive/negative half of the basis function and $r_c^{B_+}$ and $r_c^{B_-}$ are the centroids of the positive and negative halves of the basis functions, respectively. The vector potential corresponding to the negative half of the basis function can be computed similarly, and the resulting final form of (**3.14**) can be written:

$$\begin{aligned}\langle T,A\rangle=\frac{l_t^+}{2}&\left\{\frac{l_b^+}{2}G_A^{xx}\left(r_c^{T_+}-r_c^{B_+}\right)+\frac{l_b^-}{2}G_A^{xx}\left(r_c^{T_+}-r_c^{B_-}\right)\right\}\\&+\frac{l_t^-}{2}\left\{\frac{l_b^+}{2}G_A^{xx}\left(r_c^{T_-}-r_c^{B_+}\right)+\frac{l_b^-}{2}G_A^{xx}\left(r_c^{T_-}-r_c^{B_-}\right)\right\}\end{aligned} \tag{3.18}$$

Note that the original formulation, which required quadruple integrals, has now been reduced to a very simple form that only requires the evaluation of four Green's function values and simple arithmetic operations.

The procedure for the second inner product in (**3.12**), related to the contribution from the scalar potential, is similar to the one for the vector potential, and we begin this process by considering the following equation:

$$\langle \mathbf{T}(r),\nabla\phi\rangle=\iint_{\Omega_T}\mathbf{T}(r)\cdot\nabla\phi\,dr \tag{3.19}$$

If the testing function is a full rooftop function, we can use vector calculus together with the condition that the current component normal to the boundary of the rooftop must vanish, to write (**3.19**) as

$$\langle \mathbf{T}(r), \nabla\phi \rangle = -\iint_{\Omega_T} \phi \nabla \cdot \mathbf{T}(r) dr \tag{3.20}$$

Following a similar procedure to the one used for the vector potential, (**3.20**) can be cast in a simpler form as follows:

$$\langle \mathbf{T}(r), \nabla\phi \rangle = -\phi\left(r_c^{T_+}\right) + \phi\left(r_c^{T_-}\right) \tag{3.21}$$

Assuming, once again, that the Green's function is very smooth within the range of integration, the scalar potential at the centroid of the positive half of the testing function can be expressed as

$$\phi\left(r_c^{T_+}\right) = \iint_{\Omega_{B_+}} G_\phi\left(r_c^{T_+} - r'\right) \frac{\partial B(r')}{\partial x'} dr' + \iint_{\Omega_{B_-}} G_\phi\left(r_c^{T_+} - r'\right) \frac{\partial B(r')}{\partial x'} dr' \tag{3.22}$$

Next, we use the definition of the rooftop basis function and replace the integral with the values of the Green's function at the centroids multiplied by the area of each half of the rooftop function. We can then rewrite (**3.22**) as

$$\phi\left(r_c^{T_+}\right) = G_\phi\left(r_c^{T_+} - r_c^{B_+}\right) - G_\phi\left(r_c^{T_+} - r_c^{B_-}\right) \tag{3.23}$$

The scalar potential at the centroid for the negative half of the testing function is calculated similarly, and the final form of (**3.19**) is given by

$$\langle \mathbf{T}(r), \nabla\phi \rangle = -G_q\left(r_c^{T_+} - r_c^{B_+}\right) + G_q\left(r_c^{T_+} - r_c^{B_-}\right) + G_q\left(r_c^{T_-} - r_c^{B_+}\right) - G_q\left(r_c^{T_-} - r_c^{B_-}\right) \tag{3.24}$$

We note that, once again, the original quadruple integrals have been simplified in the form of a sum of four scalar potentials, and that significant computational saving can be achieved by using this form.

To compare the impedance matrix elements calculated via the rigorous method with those obtained by using the FMG-1 method, we choose a typical layered medium problem, as shown in Fig. **3.5**. We begin by comparing the interaction between the basis and testing functions, when both are oriented along the x-direction. We consider a simple geometry, as depicted in Fig. **3.6**, in which the location of the testing function is fixed and that of the basis function is varied along a straight line. For each pair of basis and testing functions, the corresponding impedance matrix element is calculated by using both the rigorous and the FMG-1 method. Their values are plotted in Fig. **3.7**(a) as functions of the separation distance normalized to the cell size. In Fig. **3.7**(b), we plot the normalized difference as a function of the separation distance, defined by $\left|Z_{Rigorous} - Z_{FMG}\right| / \left|Z_{Rigorous}\right|$,

Fig. **3.5**: Example of a printed layered structure for impedance matrix comparison.

where $Z_{Rigorous}$ and Z_{FMG} are the matrix elements generated by the rigorous and the FMG-1 method, respectively. As expected, the above difference becomes smaller as the separation distance grows, since the Green's function becomes smoother at large distances. A comparison of the matrix elements associated with the interaction between the basis function oriented in the x-direction and the testing function in the y-direction is carried out in a similar manner, by varying the location of the basis function along a line while the testing function remains stationary (See Fig. **3.8**). In Fig. **3.9**, a comparison of the impedance matrix elements and normalized difference are plotted as a function of the separation distance. In common with the case of the interaction between the basis and testing function both oriented in the x-direction, the difference between the two results becomes smaller as the separation distance grows. We conclude, then, that for both *xx* and *xy* cases, the matrix element generated by the FMG approach shows good agreement with the direct computation provided the separation distance is larger than a threshold value, for instance, 15 cells (0.07λ in this example).

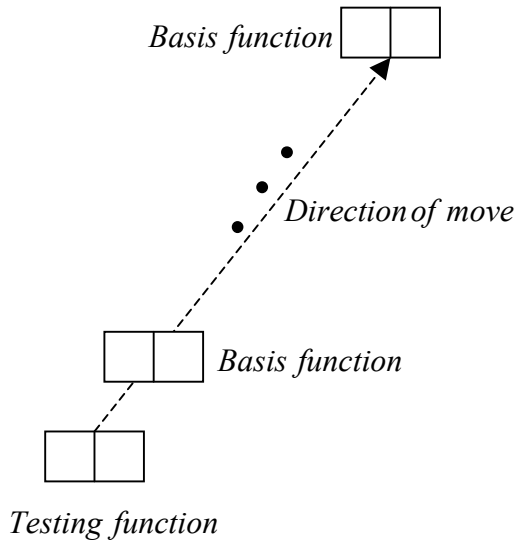

Fig. **3.6**: Geometry for the impedance matrix element comparison for the interaction between basis and testing functions both in x-direction.

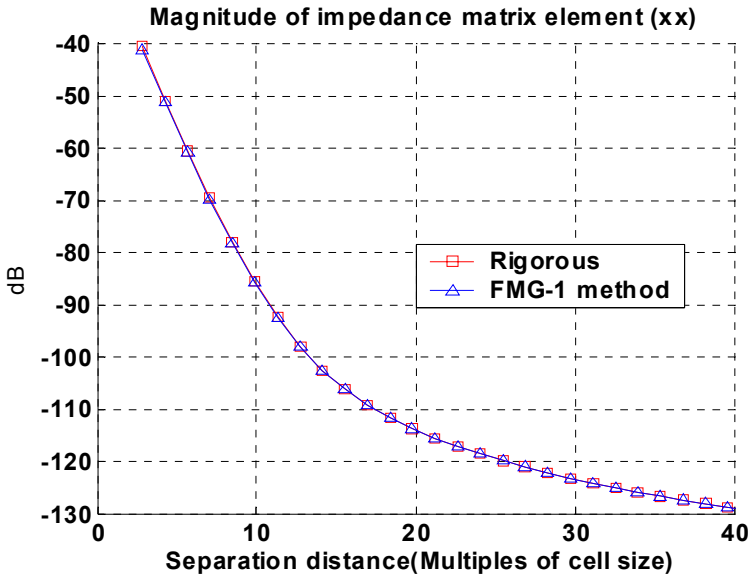

(a)

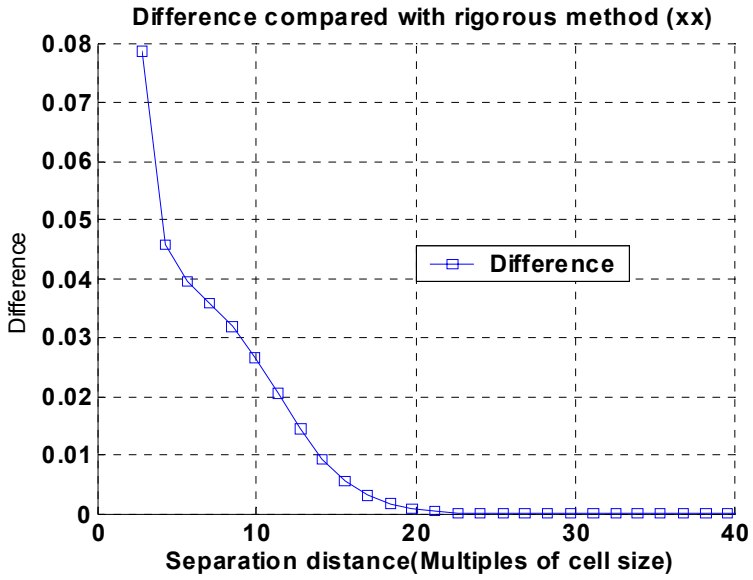

(b)

Fig. **3.7**: (a) Impedance matrix comparison for the *xx* interaction generated by the rigorous and FMG-1 methods. (b) Relative difference between the matrix elements generated by these two methods.

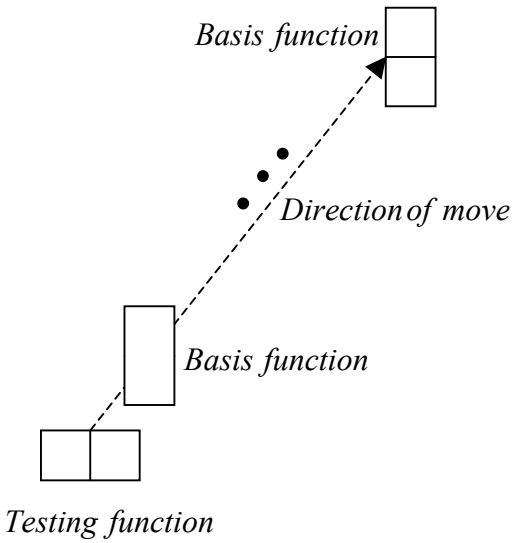

Fig. **3.8**: Geometry for the impedance matrix element comparison for the interaction between basis and testing functions in x- and y-directions, respectively.

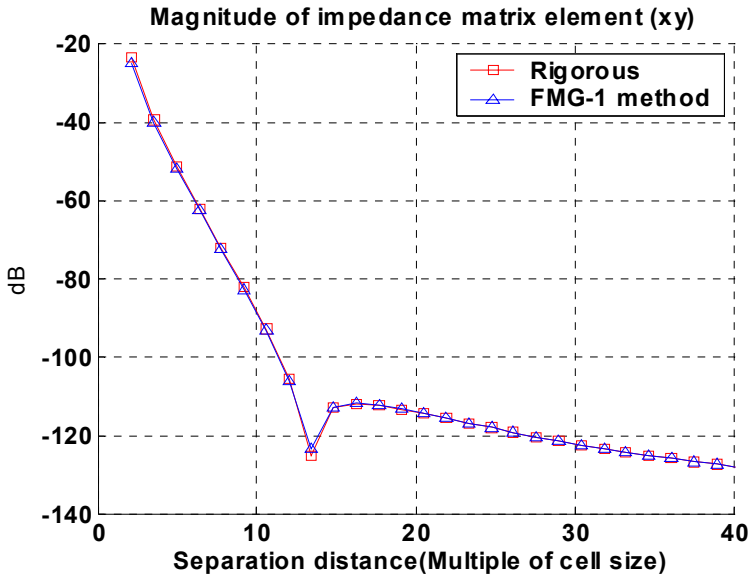

(a)

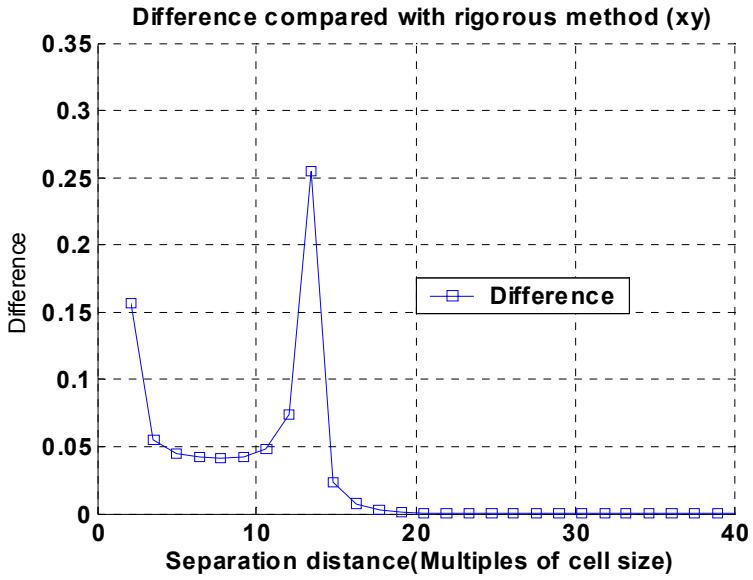

(b)

Fig. **3.9**: Impedance matrix comparison for the *xy* interaction generated by the rigorous and FMG-1 methods. (b) Relative difference between the matrix elements generated by these two methods.

3.2.4 Fast matrix generation: Method-2

In the FMG-1 method, the complexity of the impedance matrix generation was significantly reduced by replacing the integration of the Green's function with the product of its values at the centroids, and the area of each half of the rooftop functions. Since the resulting expression for the impedance matrix element required only simple arithmetic operations, this served to improve the efficiency of the impedance matrix generation significantly.

For basis and testing function pairs with large separation distances between them, it is possible to represent them as equivalent dipoles moments, a fact that can be explored in order to further reduce the time for the impedance matrix generation. Consider a basis and testing function pair with a separation distance as indicated in Fig.3.10, where $\vec{\rho}$ is a

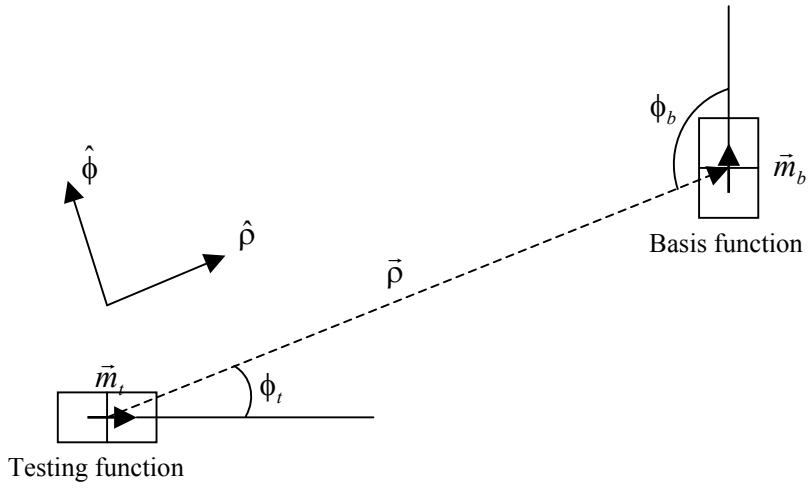

Fig. 3.10: A pair of basis and testing functions with their equivalent dipole moments and key parameters indicated.

vector from the center of the testing function to the center of the basis function; $\vec{m}_{t/b}$ is the equivalent dipole for the testing/basis function; and, ϕ_t and ϕ_b are the angles between the vector $\vec{\rho}$ and equivalent dipoles for the testing and basis functions, respectively. The equivalent dipole moments for the basis and testing functions are only dependent on the geometrical parameters of these functions, and are defined as follows:

$$\begin{aligned} \vec{m}_t &= w_t \vec{l}_t \\ \vec{m}_b &= w_b \vec{l}_b \end{aligned} \tag{3.25}$$

where $\vec{l}_{t/b}$ is the vector joining two centroids of the positive and negative halves of the testing(basis) function. Since the electric field components parallel and normal to vector $\vec{\rho}$ are orthogonal to each other, the equivalent dipoles for the basis and testing functions can be separated into components that are parallel and normal to this vector

$$\begin{aligned} m_t^{\rho} &= |\vec{m}_t||\vec{\rho}|\cos\phi_t \\ m_t^{\phi} &= |\vec{m}_t||\vec{\rho}|\sin\phi_t \\ m_b^{\rho} &= |\vec{m}_b||\vec{\rho}|\cos\phi_b \\ m_b^{\phi} &= |\vec{m}_b||\vec{\rho}|\sin\phi_b \end{aligned} \tag{3.26}$$

where $m_{t/b}^{\rho}$ is the component of the equivalent dipole parallel to $\vec{\rho}$ for the basis (testing) function, and $m_{t/b}^{\phi}$ is the corresponding component normal to $\vec{\rho}$. Since the components of the impedance matrix parallel and normal to $\vec{\rho}$ are independent, an impedance matrix element can be separated into these two components as follows:

$$Z = Z_{\rho} + Z_{\phi} \tag{3.27}$$

where Z_ρ and Z_ϕ are the impedance matrix element components representing the interaction in the $\hat{\rho}$ and $\hat{\phi}$ directions, respectively. For the component parallel to $\vec{\rho}$ in (**3.27**), the impedance matrix is expressed as

$$Z_\rho = m_t^\rho m_b^\rho Z_{\rho,ref}(\rho) c_\rho \qquad (3.28)$$

where c_ρ is a coefficient, and $Z_{\rho,ref}(\rho)$ is the impedance matrix element for the reference basis and testing functions, arranged as shown in Fig. **3.11**. As already discussed, the impedance matrix element varies very smoothly with distance ρ, when this separation distance is large, and an interpolation technique, for instance the quadratic interpolation, can be used to calculate $Z_{\rho,ref}(\rho)$ from a set of pre-computed impedance matrix elements, thus bypassing the Green's function computation. The component of the impedance matrix parallel to $\hat{\phi}$ appearing in (**3.27**) can be expressed as

$$Z_\theta = m_t^\phi m_b^\phi Z_{\phi,ref}(\rho) c_\phi \qquad (3.29)$$

where c_ϕ is a coefficient, and $Z_{\phi,ref}(\rho)$ is the impedance matrix element associated with

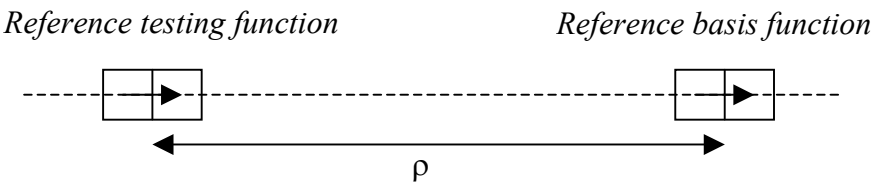

Fig. **3.11**: Arrangement of basis and testing function for calculating $Z_{\rho,ref}(\rho)$ and their equivalent dipoles.

the reference basis and testing functions, arranged as shown in Fig. **3.12**. Again, $Z_{\phi,ref}(\rho)$ is calculated by interpolating the values of a set of pre-computed impedance matrix elements. Adding these two components, the final form of (**3.27**) can be

$$Z = m_t^{\rho} m_b^{\rho} Z_{\rho,ref}(\rho) c_{\rho} + m_t^{\phi} m_b^{\phi} Z_{\phi,ref}(\rho) c_{\phi} \qquad (3.30)$$

with $m_t^{\rho}, m_b^{\rho}, m_t^{\phi}$ and m_b^{ϕ} as defined in (**3.26**). We note that the above form of the impedance matrix only involves an addition of the interpolated impedance matrix values multiplied by the equivalent dipoles and coefficients. Hence, the process above requires considerably less computation time as compared to the rigorous process. This is because the evaluation of the closed-form Green's function–which consumes substantial computation time owing to the extensive complex arithmetic operations for each of the complex images–is obviated by directly calculating the impedance matrix element using the interpolation technique.

We now carry out a comparison of the impedance matrix elements computed via

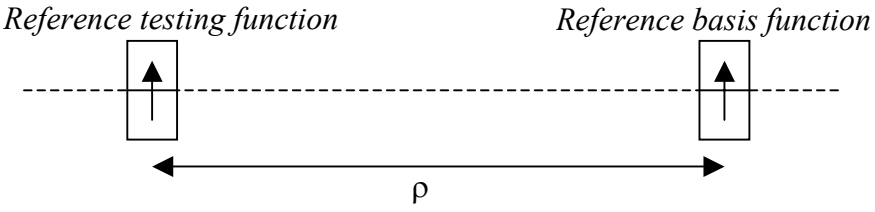

Fig. **3.12**: Arrangement of basis and testing functions for computing $Z_{\phi,ref}(\rho)$ and their equivalent dipole moments.

the rigorous and FMG-2 methods, for the same printed layered structure and geometry that were previously used for the FMG-1 method. Once again, we find that, as with the results for the FMG-1 method, the impedance matrix elements calculated from the rigorous approach and the FMG-2 method agree with each other, provided that the separation distance between the basis and testing functions are greater than 15 cell sizes, as indicated in Fig. **3.13** and **3.14**. For the *xy*-interaction between the basis and testing functions, the relative difference between the FMG-1 and -2 results is small over the entire distance range, except in the very near region. For the *xx*-interaction, the relative error in the result obtained by the FMG-1 is smaller when the distance is less than 12 cells; however, the performances of the two methods are comparable for all larger distances. For the impedance matrix elements generation with a separation distance larger than a threshold value, for example 20 cell distances, both the FMG-1 and -2 are very fast and efficient since they only require simple arithmetic operations. However, they still produce very accurate result, with differences from the direct calculation that are only on the order of 10^{-3}.

In the last two sections, we have detailed two fast and efficient impedance matrix element generation schemes for basis and testing function interactions for separation distances greater than a threshold value. The details of the algorithms have been presented along with comparisons of the impedance matrix elements for two simple geometries generated by the rigorous method and the two FMG techniques. In the following section, we demonstrate the numerical efficiency of FMG algorithms via some numerical examples for a variety of printed layered structures.

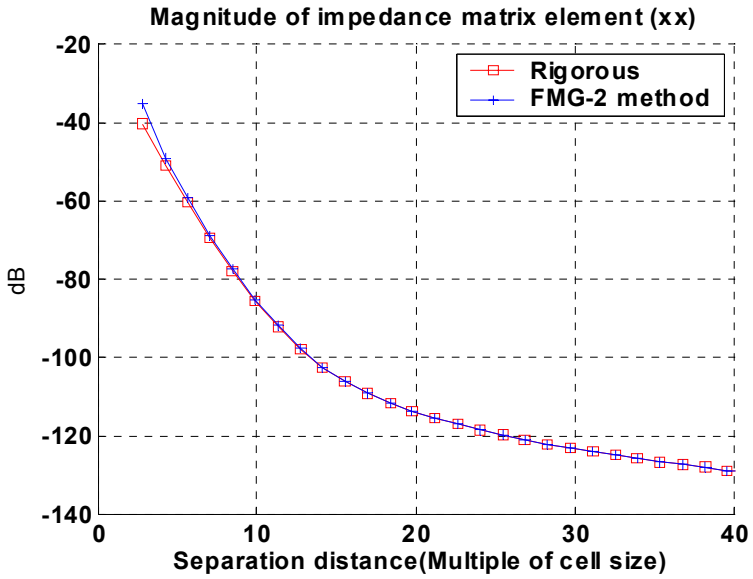

(a)

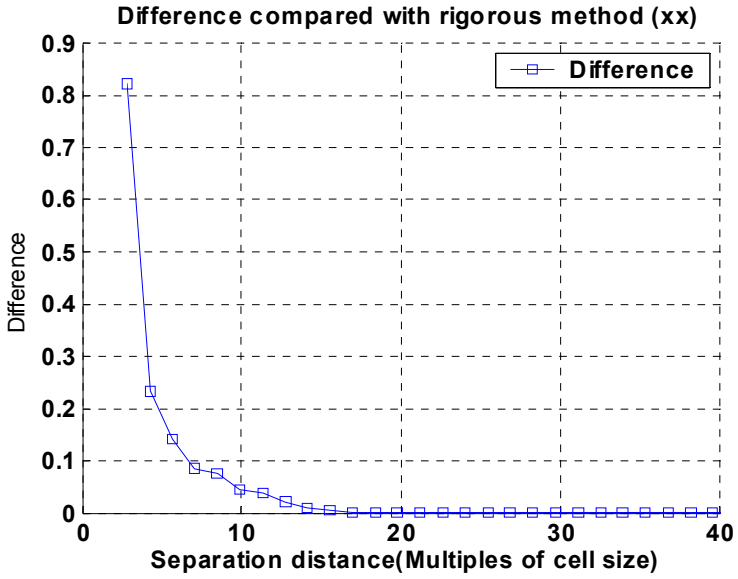

(b)

Fig. **3.13**: (a) Impedance matrix comparison for the *xx* interaction generated by the rigorous and the FMG-2 methods. (b) Relative difference between the matrix elements generated by these two methods.

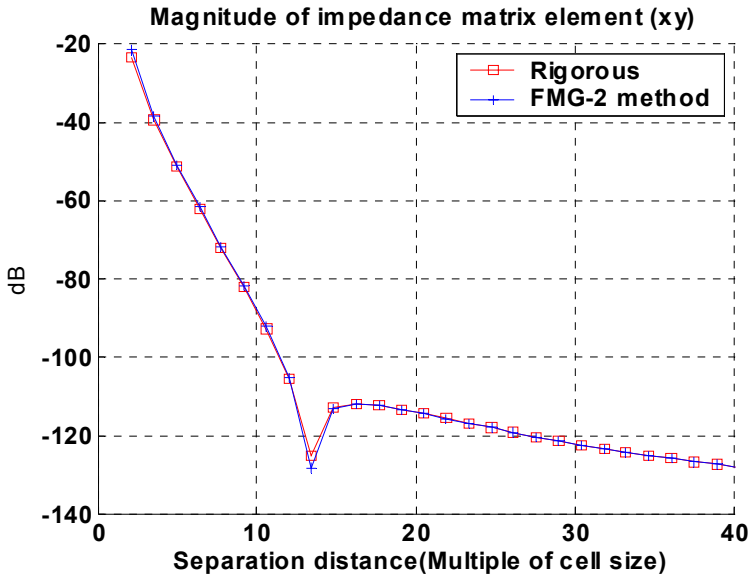

(a)

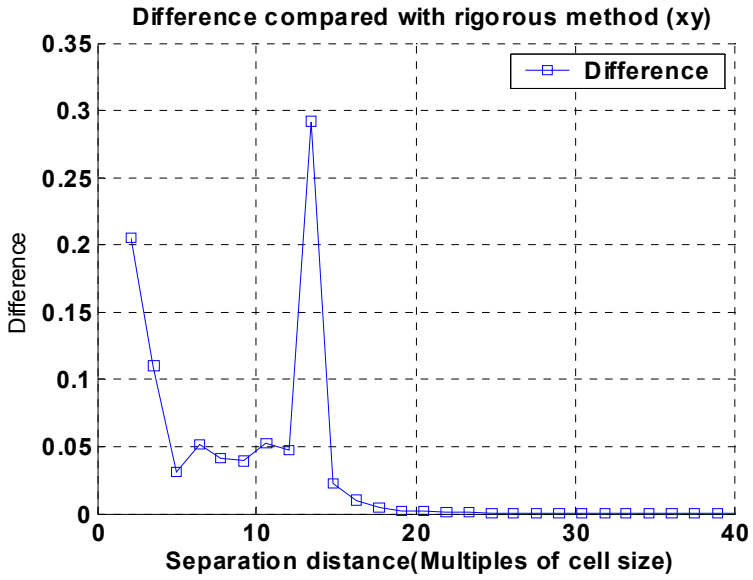

(b)

Fig. **3.14**: (a) Impedance matrix comparison for the *xy* interaction generated by the rigorous and FMG-2 methods. (b) Relative difference between the matrix elements generated by these two methods.

3.3 Numerical results

The Fast Matrix Generation technique, as discussed in previous sections, is very fast and efficient in calculating the impedance matrix elements corresponding to basis/testing function pairs whose separation distances exceed a threshold value. Since the smoothness of the Green's function within the integration range for the basis/testing function pair is the key factor that governs the feasibility of this technique, the threshold distance is closely related to the cell size, as well as to the separation distance. For example, it is observed that for problems with a smaller cell size, the threshold distance is also smaller than for those with a larger cell size. Thus, it is reasonable to define the threshold distance in terms of the cell size of the geometry After extensive experimentation with a variety of printed layered structure problems, we have determined that the threshold value of a 10 to 15-cell distance, measured from the center of the basis function to the center of the testing function, is a practical value that can be used for most printed layered structures. To illustrate this, we present numerical results for three representative geometries: (i) bandpass filter; (ii) four-pole elliptic bandpass filter, and (iii) rectangular resonator.

3.3.1 Bandpass filter

The first example is a bandpass filter implemented on a dielectric layer with $\varepsilon_r = 9.8$, backed by a PEC ground plane. The geometry of this layered structure is shown in Fig. 3.15 together with its dimensions: $w = 0.2406\,mm$, $l_1 = 1.8045\,mm$,

$l_2 = 1.5038\,mm$, $d_1 = 1.2632\,mm$, $d_2 = 1.5037\,mm$, $g_1 = 0.1805\,mm$, $g_2 = 0.3008\,mm$, and $g_3 = 0.1203\,mm$. The filter consists of 6 isolated components that are discretized into 532 cells, resulting in 786 unknowns. The simulation is carried out over a frequency range of 11 GHZ to 13 GHz, and the MoM simulations are performed for 41 frequencies by using 3 different methods, *viz.*, the rigorous, the FMG-1 and the FMG-2 methods. 10-cell distance is used as the threshold value, implying that the FMG technique is employed for the basis and testing function pairs, with a separation distance greater than 10Δ, where Δ is the cell size. The analysis was performed on a Pentium IV PC with a 3 GHz processor and a 2 Gbyte RAM.

First, we applied the rigorous and FMG-1 methods to simulate the filter geometry, and the resulting S-parameters are plotted as functions of the frequency in Fig. **3.16**. The two curves for the magnitude of S_{11} in Fig. 3.16(a) are almost indistinguishable for the entire frequency range, and the curves for the magnitude of S_{21} in Fig. 3.16(b) also indicate very good agreement with each other. The computation time required for a single frequency MoM simulation by the FMG-1 method was 13 sec, whereas the same process by the rigorous method required 155 sec. Thus, the timesaving was approximately 92% when the FMG-1 method was used.

Next, the FMG-2 method, using the same threshold value as that for FMG-1 method, was applied for the simulation of the bandpass filter geometry, and the S-parameters derived by the two methods are compared in Fig. **3.17**. As in the first case, the S-parameters obtained from the rigorous and FMG-2 methods agree very well with each other over the entire frequency range. The computation time for the impedance matrix

generation by using the FMG-2 method was 12 sec for a single frequency, indicating that a significant saving in the computation time is achieved once again. Since the portion of the impedance matrix that is subject to the application of the FMG approach is expected to grow with the increase in the dimension of the geometry, there exists a great potential for realizing even more timesavings when dealing with larger geometries.

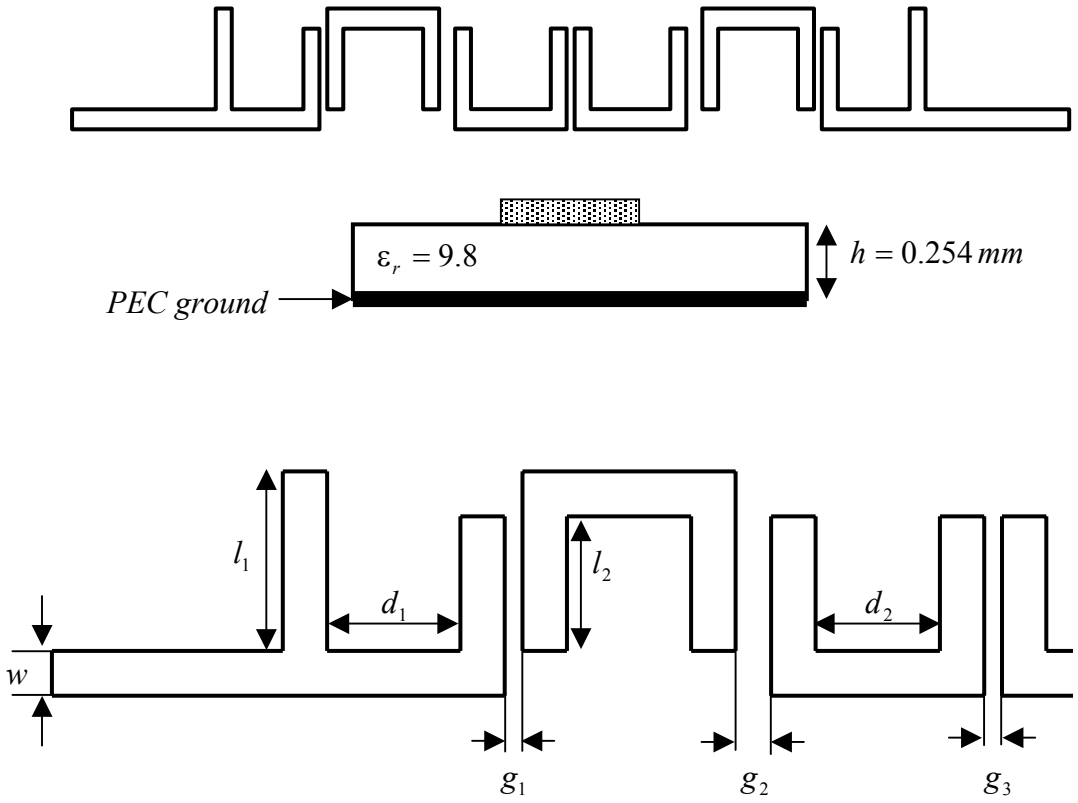

Fig. **3.15**: Geometry of the bandpass filter: (a) entire geometry. (b) One-half of the geometry with the definitions of the relevant geometrical parameters.

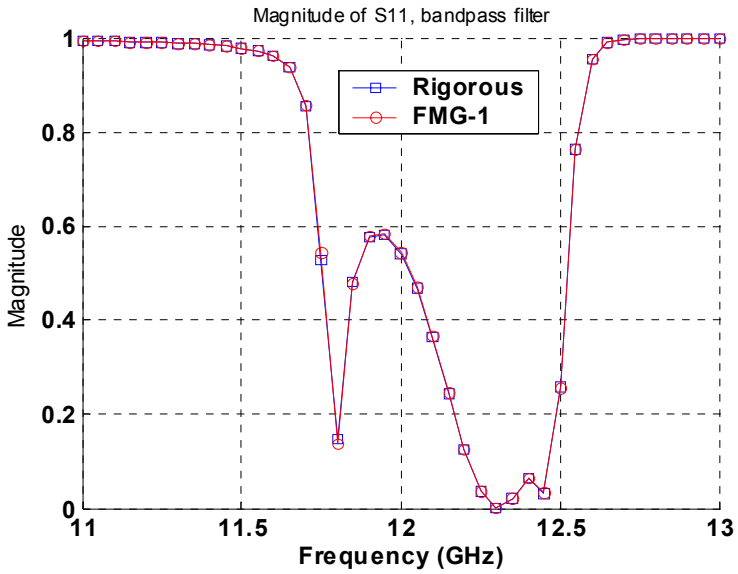

(a)

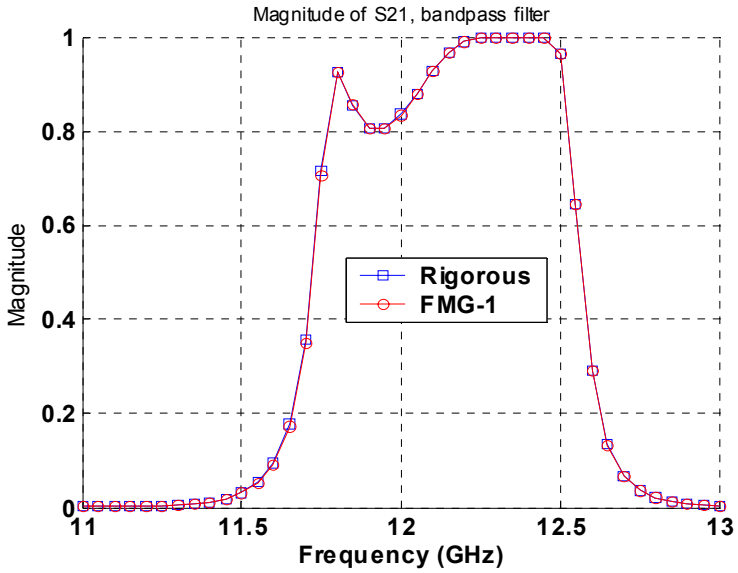

(b)

Fig. **3.16**: Comparison of the S-parameters for the bandpass filter derived by using the rigorous and FMG-1 methods: (a) S_{11}; (b) S_{21}.

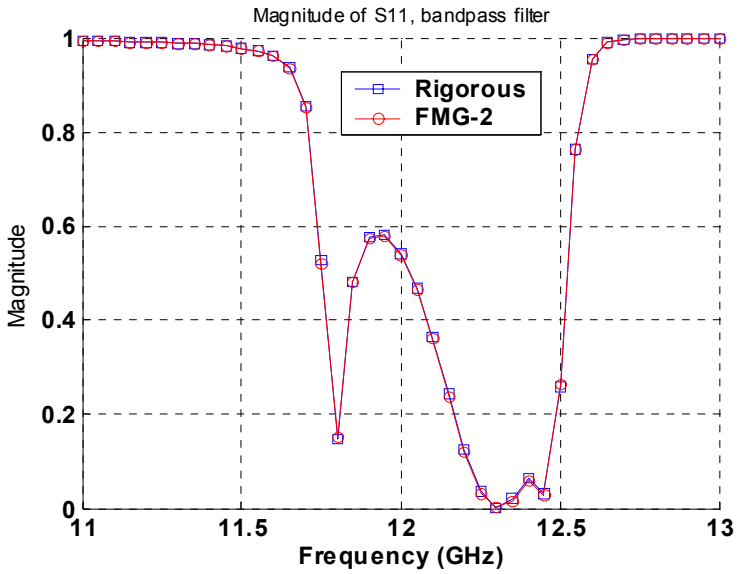

(a)

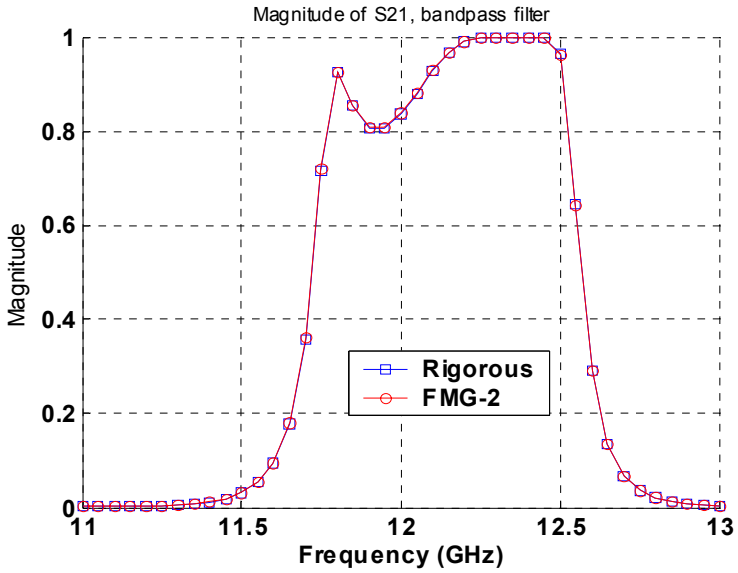

(b)

Fig. **3.17**: Comparison of the S-parameters for the bandpass filter derived by using the rigorous and FMG-2 methods: (a) S_{11}; (b) S_{21}.

3.3.2 Four-pole elliptic bandpass filter

For the second example of the application of the FMG technique, we consider a four-pole elliptic bandpass filter, realized by four coupled resonators on a dielectric layer with $\varepsilon_r = 10.8$ and $h = 1.7\,mm$ (See Fig. **3.18**). The geometry is divided into 966 cells, and the rooftop basis functions are used to model the surface currents, resulting in 1598 unknowns. The geometry was analyzed by using the rigorous impedance matrix generation method, over a frequency range of 2.4 GHz to 2.8 GHz, with a frequency step $\Delta f = 0.01\,\text{GHz}$. The time required to generate the impedance matrix was 380 sec on a Pentium IV PC, with a 3 GHz processor and 2 Gbyte RAM. Then, the same geometry was simulated via the FMG-1 method with using a threshold value of 15Δ and the computation time for the impedance matrix generation for 41 frequencies was now only 42 sec. The curves of the magnitudes of S_{11} and S_{21}, extracted from the simulation results by both the rigorous method and the FMG-1 method, are plotted in Fig. **3.19**, and they show good agreement with each other. Next, the same geometry was again analyzed via the FMG-2 method using the same threshold value(15Δ), and the computation time required for the impedance matrix generation for 41 frequencies was 44 sec, which is comparable to that of the FMG-1 method. The S-parameters obtained by using the rigorous and FMG-2 methods are plotted in Fig. **3.20**, and, once again, we observe that the two curves match very well. In both cases, approximately 89% of timesaving was achieved over the direct method, when the FMG techniques was used.

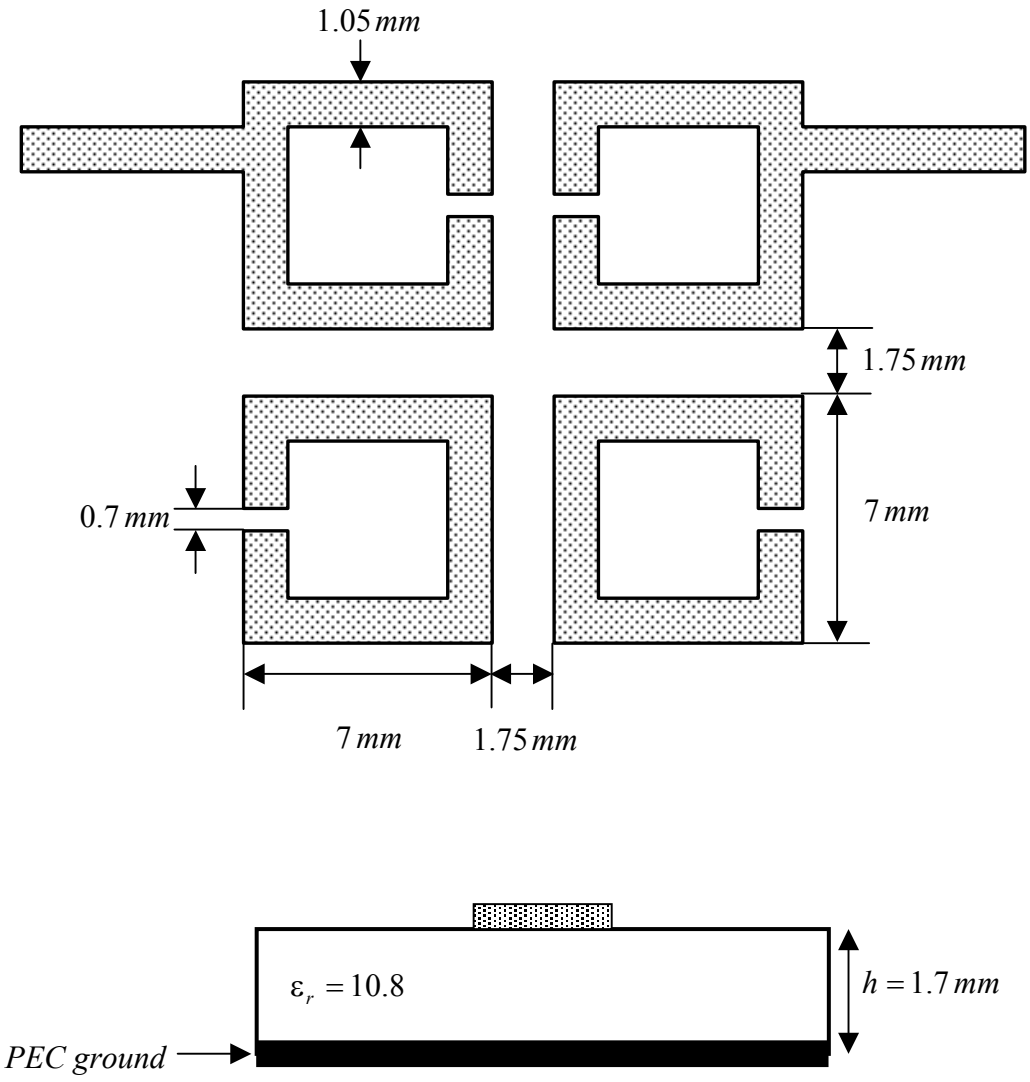

Fig. **3.18**: Geometry of the four-pole elliptic bandpass filter.

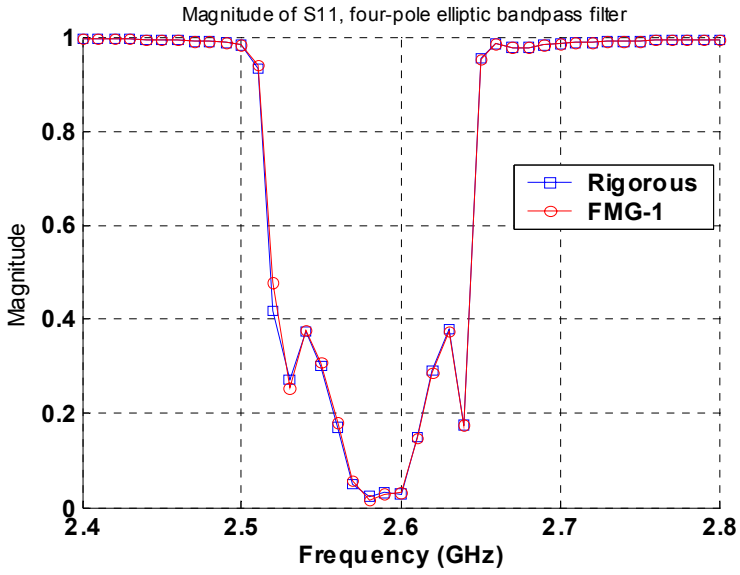

(a)

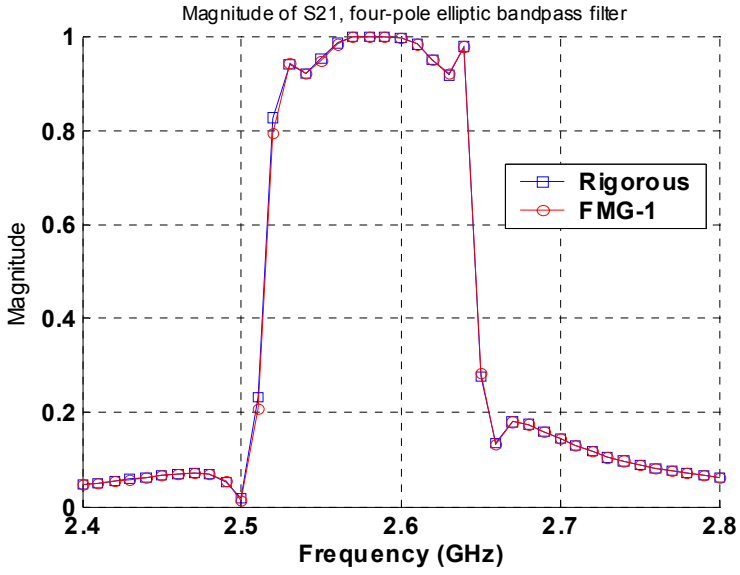

(b)

Fig. **3.19**: Comparison of the S-parameters of a four-pole elliptic bandpass filter, derived by using the rigorous and FMG-1 methods: (a) S_{11}; (b) S_{21}.

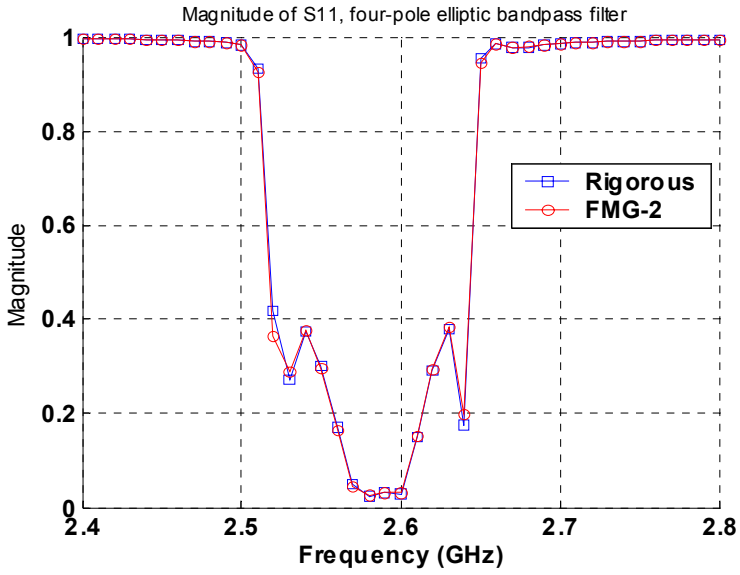

(a)

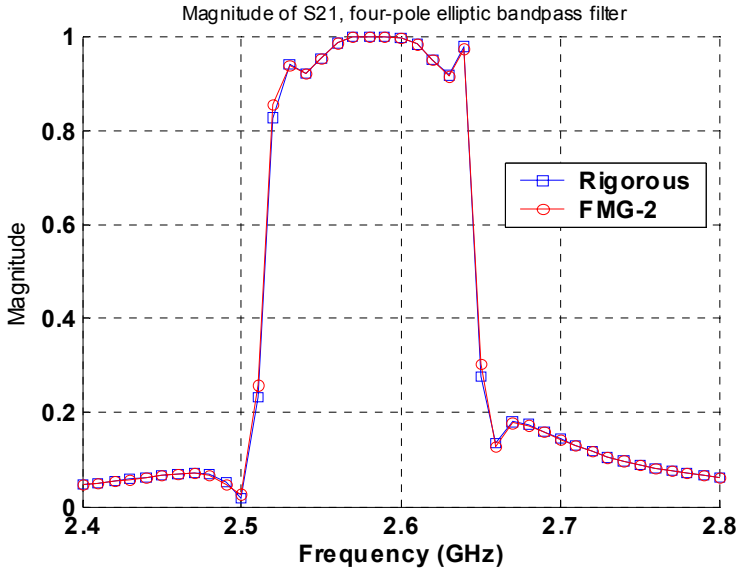

(b)

Fig. **3.20**: Comparison of the S-parameters of a four-pole elliptic bandpass filter, derived by using the rigorous and FMG-2 methods: (a) S_{11}; (b) S_{21}.

3.3.3 Rectangular resonator

The last example is a rectangular resonator with a resonant frequency of 5.15 GHz that is printed on a PEC-backed dielectric layer, as illustrated in Fig. **3.21**. The geometry is discretized into 579 cells, and the total number rooftop type of unknowns is 962. As in the previous examples, the MoM simulation is performed via three techniques, for 41 frequencies over the frequency range 4.5 GHz to 5.5 GHz. Similar to the previous examples, the geometry was first analyzed by the rigorous method over the operating frequency range and, then, the S-parameters were extracted from the current coefficients. With the rigorous method, the CPU time required for the impedance matrix generation was 233 sec on a Pentium IV PC with a 3 GHz processor and 2 Gbyte RAM. Next, the simulation was repeated by using both the FMG-1 and -2 methods, with the threshold set equal to 15Δ, and the S-parameters were calculated once again. The results obtained by using the rigorous and FMG-1 methods are shown in Fig. **3.22** and they are seen to be in very good agreement with each other throughout the entire frequency range. In Fig. **3.23**, the S-parameters calculated by the rigorous and FMG-2 methods are shown and, once again, these two curves exhibit a very good match. The CPU times required for the FMG-1 and -2 methods were 16 and 27 sec, respectively, leading to 93% and 88% savings in computation time. In Table **3-1**, we present the comparison of the impedance matrix computation times for the sample geometries investigated in this chapter by using the rigorous as well as the two FMG methods.

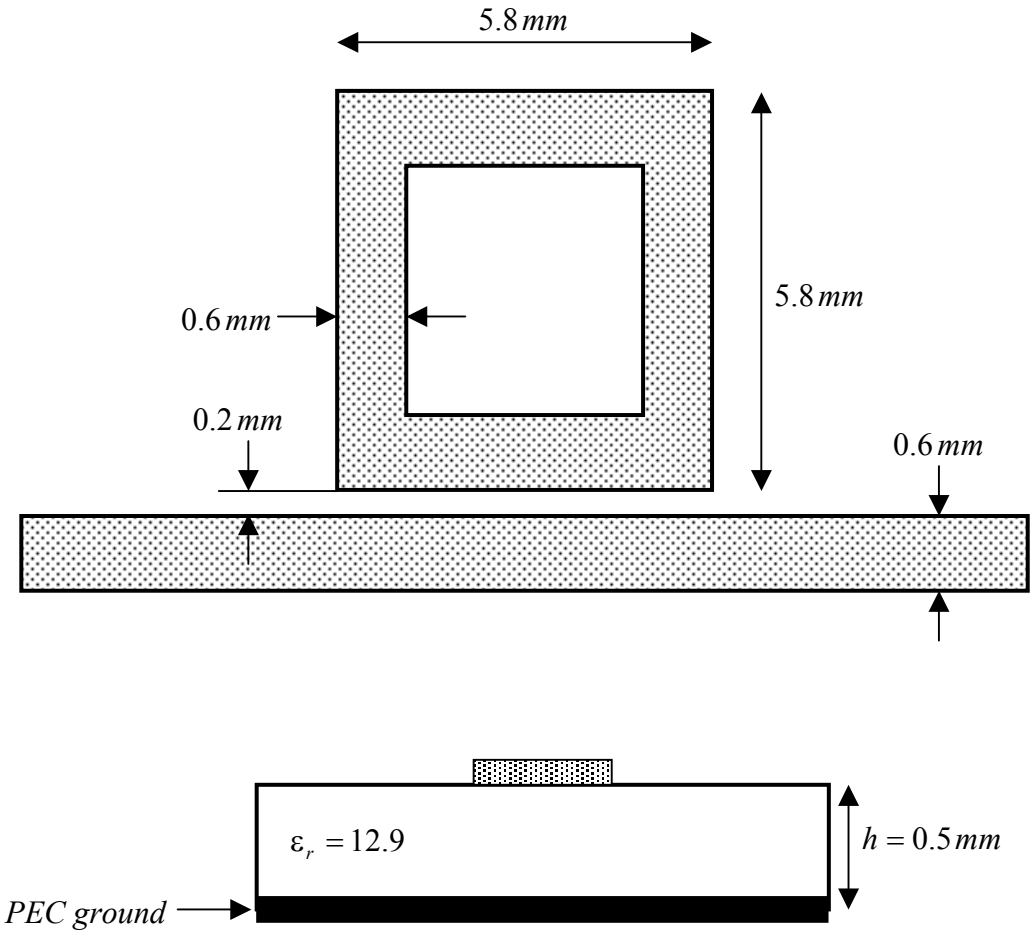

Fig. **3.21**: Geometry of a rectangular resonator.

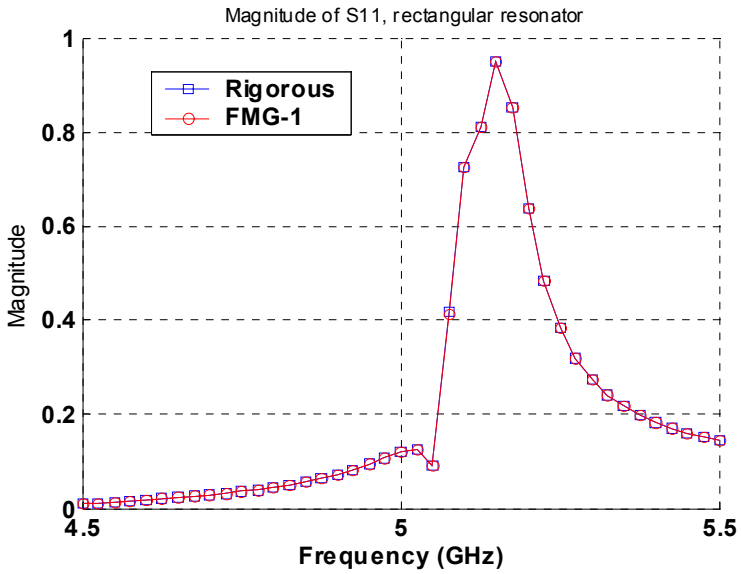

(a)

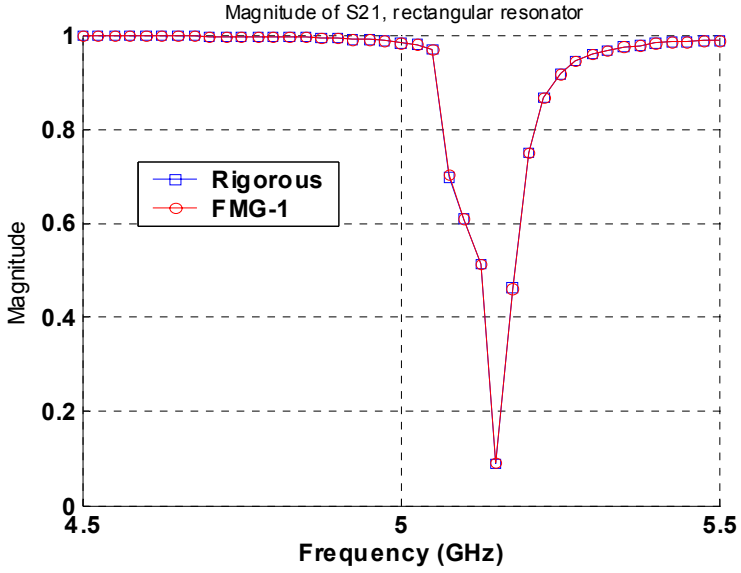

(b)

Fig. **3.22**: Comparison of the S-parameters of a rectangular resonator, derived by using the rigorous and FMG-1 methods: (a) S_{11}; (b) S_{21}.

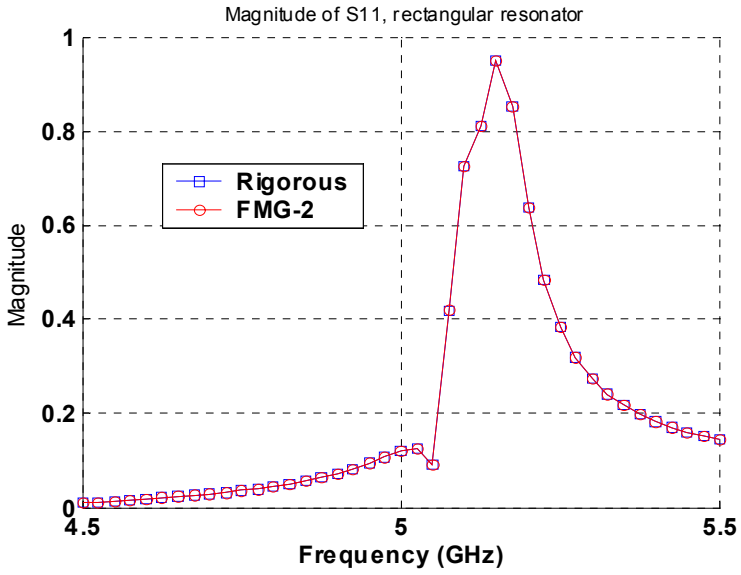

(a)

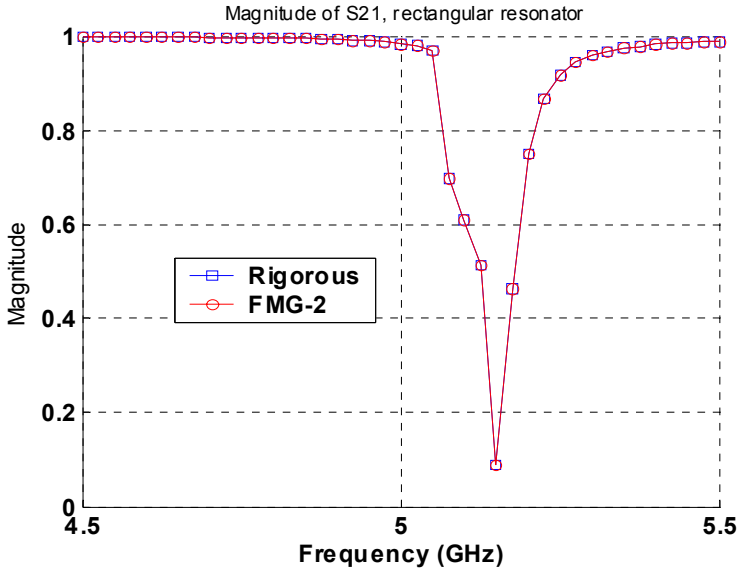

(b)

Fig. **3.23**: Comparison of the S-parameters of a rectangular resonator, derived by using the rigorous and FMG-2 methods: (a) S_{11}; (b) S_{21}.

Table 3-1: Comparison of the impedance matrix generation times for example problems (Pentium IV 3 GHz, 2 GByte RAM)

Geometry	Number of unknowns	Time (sec)		
		Rigorous method	FMG-1	FMG-2
Bandpass filter	786	6355	533	492
Four-pole elliptic bandpass filter	1598	380	42	44
Rectangular resonator	962	233	16	27

3.4 Conclusions

In this chapter, we have presented a numerically efficient impedance matrix generation algorithm called the Fast Matrix Generation (FMG), and have introduced two matrix generation schemes that make use of the smooth behavior of the Green's function, and the concept of the equivalent dipole, for computing the matrix elements. In this approach, the elements corresponding to the basis/testing function pairs with the separation distance larger than a threshold value are evaluated by using the FMG technique, while the remainder is computed by using the rigorous method. Since the evaluation of the impedance matrix element by the use of the FMG technique only

involves simple arithmetic operations, the CPU time required for the impedance matrix generation is reduced significantly. Numerical results for several example problems for printed layered structures are presented, verifying that the FMG technique reduces the impedance matrix computation time substantially, while maintaining the accuracy of the parameters of interest. Note that, in some examples studied in this chapter, the FMG-2 method required more computation time than FMG-1, simply because the implementation of FMG-2 needs further improvement, and not because of the algorithm itself. Though not discussed in this chapter, the algorithm is very general, and it is possible to extend it to other applications, such as the solutions of three-dimensional scattering problems.

Chapter 4

EFFICIENT IMPEDANCE MATRIX INTERPOLATION TECHNIQUE FOR THE ANALYSIS OF PRINTED LAYERED STRUCTURE

4.1 Introduction

Today, the wireless communications market and industry are growing at an unprecedented rate, which, in turn, has stimulated the development of faster and more efficient techniques for the design and analysis of printed layered structures, for instance, microstrip and stripline. Full-wave field solvers based on techniques such as the Finite Difference Time Domain (FDTD) [1], Finite Element Method (FEM) [2], and the Method of Moments (MoM) [3] are commonly used for analysis of layered structure problems. Among these, the MoM has been the most commonly used because its problem domain only includes the surface of the conductor where the current densities are defined. However, MoM includes a series of computationally intensive processes – a derivation of Green's function, impedance matrix filling, and the solution of a matrix equation – and consumes considerable resources such as the CPU time and memory, even for moderate-size problems.

The efficiency of the derivation of the spatial-domain Green's function has been significantly improved by employing the closed-form Green's function technique [5,6]. With this technique, the spectral domain Green's function, which is readily derived in an analytical form, is first approximated by complex exponentials and, then, the spatial-domain counterpart is obtained via the Sommerfeld identity.

The impedance matrix filling is another time-consuming process of MoM since it requires the evaluation of reaction integrals for each matrix element, and since the number of matrix elements grows as $O(N^2)$, where N is the number of unknowns. Moreover, the analysis of the layered structures is typically performed over a band of frequency, and the impedance matrix-filling process needs to be repeated for each frequency point. For instance, the analysis of a microstrip filter may require the application of MoM for more than 100 frequency points to pick up the fine features of the frequency response; therefore, the computation time can be prohibitively large.

An approach for speeding up the impedance matrix generation over a frequency band is the impedance matrix interpolation, for which various techniques have been proposed in the past. In [17], Newman and Forrai suggested an impedance matrix interpolation using three pre-calculated impedance matrices and applied it to the scattering analysis of a microstrip patch on a grounded dielectric. Later, Newman improved this technique by using two different interpolation schemes for the imaginary part of the matrix elements, depending on the separation distance between the source and the field points [18]. In addition, the phase variation was factored out from the impedance matrix element if the separation distance was large. Virga and Rahmat-Samii applied the technique in [18] to the analysis of personal communication antennas [19]. In their follow-up paper [20], they compared interpolation schemes for [Z] and [Y] matrices, showing that [Y] matrix interpolation is highly dependent upon the resonant characteristics of the structure. In [21] and [22], Barlevy and Rahmat-Samii modified the algorithms in [19] and [20], and applied them to FSS and EGB structures. Wei and Li [23] employed Pade approximation to interpolate the impedance matrix for the MoM part

of the geometry in the MoM-PO method. However, the interpolation schemes in these papers have been studied only for structures in free space, except for [17] where simple quadratic interpolation was used for real and imaginary parts of the impedance matrix. Recently, Yeo and Mittra [24] proposed an interpolation technique for layered structures that employs different interpolation schemes, depending on the separation distance between the source and field points. However, the schemes in [24] produce considerable discrepancies between the matrix element computed by the direct and interpolation methods even for the intermediate distance range, and a more accurate and robust algorithm is desired for the analysis of general layered structures.

In this chapter, we present a novel approach for the impedance matrix interpolation that can be readily incorporated into existing codes. In this method, the accuracy of the interpolation has been improved over previous works and this, in turn, has improved the accuracy of the final parameters of interest. In the remainder of this chapter, the theory and details of the technique are discussed and the efficiency of the proposed technique is demonstrated by showing the numerical results for a variety of sample problems.

4.2 Theory and algorithm

In this section, we first summarize the formulation of the integral equation technique in conjunction with the MoM, and then discuss the details of the new impedance matrix interpolation technique. The closed-form Green's function technique is used for the derivation of the spatial-domain Green's function due to its efficiency and

versatility, along with the mixed-potential integral equation (MPIE) for its superior performance in reducing the singularity over the electric field integral equation.

4.2.1 Integral equation and the method of moments (MoM)

We begin the formulation of the integral equation by imposing an appropriate boundary condition on the surface of the conductors. If we assume that the conductors have infinite conductivity, the total electric field vanishes on the surface of the conductors, which leads to the following equation:

$$\mathbf{E}_i(r) + \mathbf{E}_s(r) = 0 \tag{4.1}$$

where $\mathbf{E}_i(r)$ and $\mathbf{E}_s(r)$ are the impressed and scattered electric field, respectively. This assumption holds for the remainder of this chapter. The scattered electric field in (4.1) can be expressed in terms of the magnetic vector potential A and the electric scalar potential ϕ as

$$\mathbf{E}_s(r) = -j\omega\mathbf{A} - \nabla\phi \tag{4.2}$$

where ω is the angular frequency. By substituting (4.2) in (4.1) and using the spatial-domain Green's functions for the vector and scalar potentials, we obtain the following equation:

$$\mathbf{E}_i(r) = j\omega\int \overline{\mathbf{G}}_A(r,r')\cdot\mathbf{J}(r')dr' - \frac{1}{j\omega}\nabla\int G_\phi(r,r')\nabla'\cdot\mathbf{J}(r')dr' \tag{4.3}$$

where $\overline{\mathbf{G}}_A(r,r')$ and $G_\phi(r,r')$ are the dyadic vector potential and scalar potential Green's functions, respectively. Then, the current induced on the surface of the conductor is modeled by the superposition of known basis functions

$$\mathbf{J} = \sum_{p=1}^{M} \alpha_p \mathbf{B}_p(r') \tag{4.4}$$

where $\mathbf{B}_p$ is the basis function, α_p is the coefficient, and N is the number of basis functions. Next, the inner product is performed between the induced electric field and suitable testing functions, which yields N linear equations. The testing functions identical to the basis functions are commonly used because of their superior performance. This method, called the Galerkin process, has been widely used for the analysis of printed layered structures. The final form of the matrix equation in matrix notation is written

$$[\mathbf{Z}][\mathbf{I}] = [\mathbf{V}] \tag{4.5}$$

where $[\mathbf{Z}]$ is the $N \times N$ impedance matrix, $[\mathbf{I}]$ is the $N \times 1$ current coefficient vector, and $[\mathbf{V}]$ is the $N \times 1$ excitation vector. The entries of the impedance matrix are expressed as

$$Z = j\omega \left\langle \mathbf{T}(r), \int \overline{\mathbf{G}}_A(r,r') \cdot \mathbf{B}(r') dr' \right\rangle - \frac{1}{j\omega} \left\langle \mathbf{T}(r), \nabla \int G_\phi(r,r') \nabla' \cdot \mathbf{B}(r') dr' \right\rangle \tag{4.6}$$

where Z denotes the impedance matrix element, $\mathbf{T}(r)$ and $\mathbf{B}(r)$ are the testing and basis functions, respectively. For the convenience of numerical processing, we divide both sides of the matrix equation (4.6) by $j\omega$ to get

$$Z = \left\langle \mathbf{T}(r), \int \overline{\mathbf{G}}_A(r,r') \cdot \mathbf{B}(r') dr' \right\rangle + \frac{1}{\omega^2} \left\langle \mathbf{T}(r), \nabla \int G_\phi(r,r') \nabla' \cdot \mathbf{B}(r') dr' \right\rangle \tag{4.7}$$

In (4.7), the first and second terms on the right-hand side account for the contributions from the vector and scalar potentials, respectively. Note that for planar and layered type of configurations, each element of the impedance matrix requires the evaluation of quadruple integrals, and, as already discussed, this operation has to be repeated for all frequency points. Therefore, it is highly desirable to devise an efficient technique for impedance matrix generation over a wide frequency range.

It is well known from previous works [17-24] that while most of the parameters of interest or the surface current of the layered structure vary rapidly with frequency due to the resonance of the structure, the impedance matrix element changes slowly with the frequency. We take advantage of this fact and generate the impedance matrix for a wide range of frequency by using the interpolation technique, rather than doing the same by direct computation.

4.2.2 Interpolation algorithm

We begin the discussion of the impedance matrix interpolation by first revisiting the equation (4.7). Here, it is observed that the frequency variation of the impedance matrix element is intimately related to the frequency characteristics of the vector and scalar potential Green's functions, with the exception of the $1/\omega^2$ factor for the second inner product. The derivation of the spatial-domain Green's function by using the closed-form Green's function technique begins with placing a single source in a layer and expanding the field due to this source by the superposition of infinite plain waves via the Weyl identity. Then, the spectral-domain Green's function is derived in an analytical

form by considering the multiple reflections occurring at each interface due to the inhomogeniety in one direction. Next, the spectral-domain Green's function is approximated by a linear combination of complex exponentials, and, finally, the spatial-domain counterpart is derived via the Sommerfeld identity. The spatial-domain Green's function obtained by this process has the form

$$G = \sum_{i=1}^{M} a_i \frac{e^{-jkr_i}}{r_i} \qquad \left(r_i = \sqrt{\rho^2 - b_i^2}\right) \tag{4.8}$$

where ρ is the radial distance between the source and field points; a_i and b_i are the constants for the complex image i; and k is the wavenumber of the source layer.

In [24], the phase variation $e^{-jk_e r}$, where k_e is the effective wavenumber, is factored out before the interpolation of the matrix elements associated with basis/testing function pairs whose separation distances exceed a certain threshold. However, it is not clear how to determine the effective wavenumber for a geometry since its definition is associated with a specific transmission line, and the Green's function, which governs the frequency characteristics of matrix elements, is independent of the geometry. As discussed above, the spatial-domain Green's derived by the closed-form Green's function technique involves the wavenumber in the source layer, and thus, it is physically more reasonable to use the wavenumber of the source layer than the effective wavenumber.

As shown in (4.7), the frequency characteristics of the spatial-domain Green's function is the key factor that governs the efficiency of the frequency interpolation. Many researchers have studied the frequency variation of the spatial-domain Green's function [25-27]. It turns out that the magnitude of the vector potential Green's function changes little with frequency, while the corresponding variation of the scalar potential Green's

function depends on the distance. The magnitude of the scalar Green's function varies little with frequency in the near region, while its magnitude is proportional to f^2 and f^4 in the intermediate and far region, respectively. However, the above description provides only a rough idea of the frequency characteristics of the Green's functions since the frequency characteristics for a specific geometry depend on factors such as the geometrical parameters and the frequency range, and thus the theoretical prediction of the frequency variation of the spatial-domain Green's function is very difficult, if not impossible. A better strategy for obtaining the expressions that describe the frequency characteristics of the matrix element is to perform extensive experiments by using different polynomials. We derived interpolation schemes that can accurately model the frequency variations of the real and imaginary part of the matrix elements, and present the details of the algorithm in the following.

We illustrate the impedance matrix interpolation algorithm with reference to a sample geometry as shown in Fig. **4.1**. The patch antenna is fed by a microstrip line and discretized by using rectangular cells. The current induced on the surface of the conductor is modeled by the rooftop basis functions. In the previous work for layered structure, impedance matrices are typically computed directly at three frequencies, and the impedance matrices for all other frequency points are obtained by the interpolation technique. However, it is observed that the interpolated matrix elements exhibit discrepancies in the intermediate and far region, even with the extraction of the phase variation. For the analysis of general layered structures, it is therefore highly desirable to develop a more accurate and robust interpolation algorithm that can handle layered

structures' problems in a systematic manner. For the reasons mentioned above, we use four sample impedance matrices instead of three.

The frequency step between sampling frequencies should be chosen judiciously since the efficiency of the interpolation is closely related to this parameter. The interpolation result may not be very accurate with a large frequency step, while a very accurate interpolation result can be obtained with small frequency steps at the expense of additional time to cover the same frequency range. We use the following equation as the guideline for choosing the frequency step

$$\Delta k r_{\max} < \pi \qquad (4.9)$$

where $r_{\max}$ is the maximum distance between the source and the field points. The above relation can be written in a different form as

$$\Delta f < \frac{c}{2 r_{\max}} \qquad (4.10)$$

where Δf is the maximum frequency step and c is the speed of light in the source layer. It is important to note that (4.10) provides an estimation of an upper bound on the frequency step, so the actual step size must be determined within this range. For structures with more than one conductor layer, different values of Δk are involved since the source layers are located in more than one layer, and in this case, the above criterion needs to be modified accordingly. For multi-layer structures, source points are located on different layers, which leads to more than one maximum frequency step. To resolve this, we choose the smallest one as the maximum frequency step for the matrix interpolation. Once the frequency step is determined, a frequency window of width $3\Delta f$ is formed, and

the matrix interpolation algorithm is applied to the frequency points within this window. After performing the analysis for this window, another frequency window is formed and is repeated until the analysis is carried out for the entire frequency range of interest.

First, we consider the matrix elements associated with basis/testing function pairs whose separation distances are small. According to the observations reported in [27], both the vector and scalar potentials vary smoothly in this region, and thus the frequency characteristics of the inner products in (**4.7**) can be accurately modeled by the polynomials of frequency. For the real and imaginary part of the matrix element in the near region, we use

$$Z_r = A\frac{1}{f^2} + B\frac{1}{f} + Cf + D \qquad (4.11)$$

$$Z_i = A\frac{1}{f} + Bf + Cf^2 + D \qquad (4.12)$$

where A, B, C, and D are coefficients of the polynomials, Z_r and Z_i are the real and imaginary part of the matrix element. For each impedance matrix element, the coefficients for the real and the imaginary part are determined by using the four sampled matrix elements. This process is repeated until the coefficients for all the matrix elements are determined. Note that that only the coefficients of the interpolating polynomials need to be saved. To demonstrate the performance of the interpolation schemes for the near-field region, we choose a self-term of the rooftop basis function, and the values computed by the direct and interpolation techniques are plotted as functions of frequency in Figs. **4.2**. and **4.3**. The two curves are indistinguishable, which indicates that both the real and imaginary parts of the matrix elements computed by the interpolation are in very good agreement with those computed by the direct method.

It is known that as the distance r between the source and field points grows, the contribution from e^{-jkr} becomes the dominant frequency variation, which makes it more difficult to interpolate the matrix elements accurately. In this region, we first extract the phase variation by factoring out e^{-jkr} from the matrix element

$$Z' = \frac{Z}{e^{-jkr}} \tag{4.13}$$

where Z' is the matrix element without the phase variation e^{-jkr}. Since the frequency variation of the remaining part Z' is smoother than that of Z, it can be readily modeled by the polynomials. At this point, we need to develop a criterion for choosing the threshold distance for the application of the phase extraction. This parameter must be properly chosen because the accuracy of the interpolation depends on this value. After carrying out extensive numerical experiments, we derived the following condition for the application of e^{-jkr} extraction

$$\Delta k_w \rho > 3/4\pi \tag{4.14}$$

where ρ is the radial separation distance and Δk_w is the variation of the wavenumber in the source layer for a frequency window. We apply the same interpolation schemes used for the near region to the real and imaginary part of Z' as

$$Z'_r = A\frac{1}{f^2} + B\frac{1}{f} + Cf + D \tag{4.15}$$

$$Z'_i = A\frac{1}{f} + Bf + Cf^2 + D \tag{4.16}$$

Again, the coefficients are determined by using the sampled matrix elements, which is repeated until the coefficients for all matrix elements belonging to this region are

determined. The interpolated version of the matrix element Z' is obtained by using (**4.15)** and (**4.16**), and the original matrix element Z is obtained by multiplying the phase variation e^{-jkr} to Z'. The matrix elements representing the interactions in this region, obtained by the direct and interpolation methods, are plotted as functions of frequency in Fig. **4.4**. Similar to the case for the near region, the two curves indicate very good agreement over the entire frequency range.

In this section, we described the details of the impedance matrix interpolation algorithm, and demonstrated its accuracy by three examples that represent different distance ranges. In the following section, the efficiency and versatility of this technique is validated by numerical results for a variety of layered structure problems.

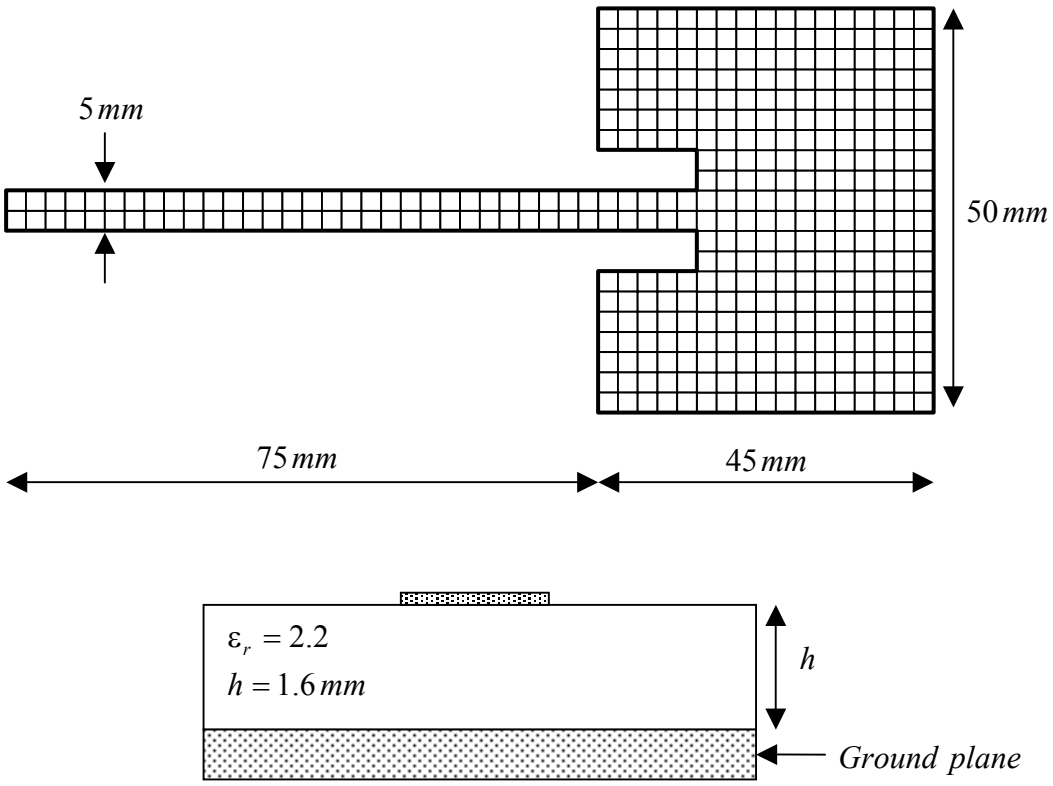

Fig. **4.1**: Geometry of a patch antenna fed by a microstrip line.

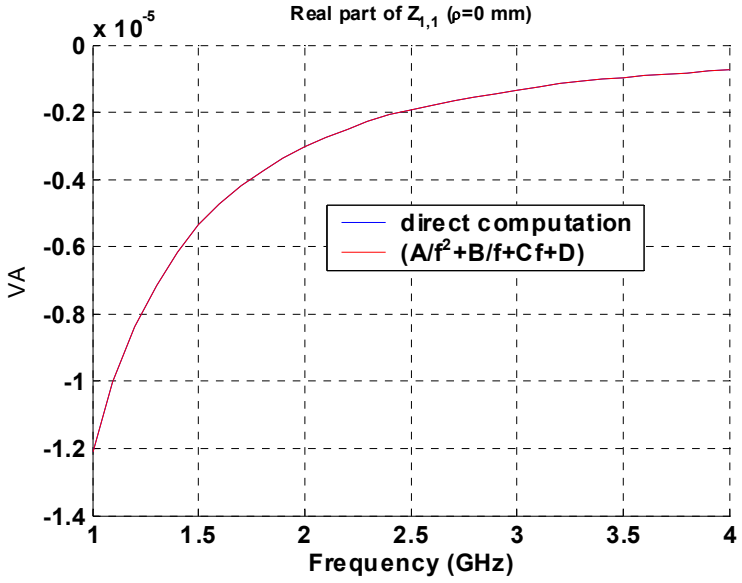

(a)

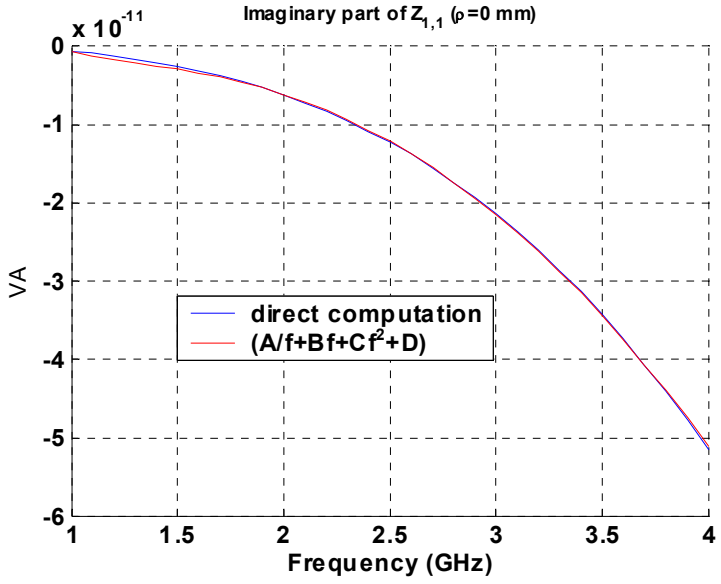

(b)

Fig. **4.2**: Comparison of impedance matrix element derived by using the direct and interpolation methods ($\rho = 0\,mm$). (a) real part; (b) imaginary part.

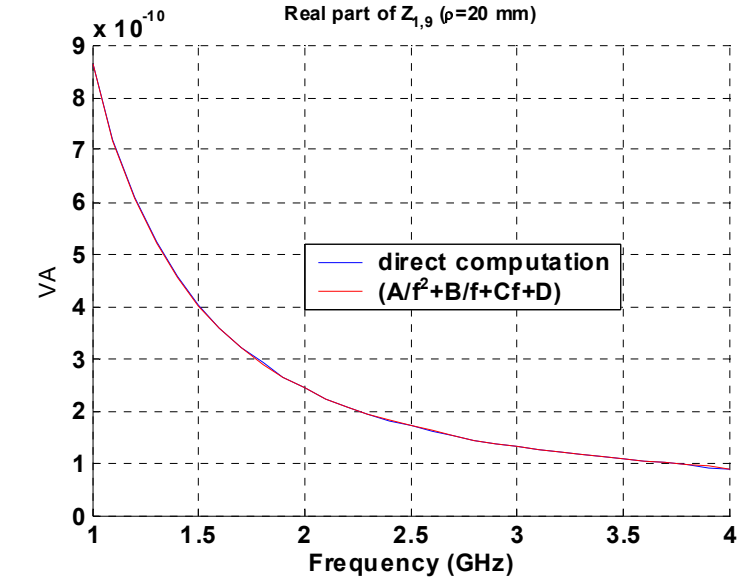

(a)

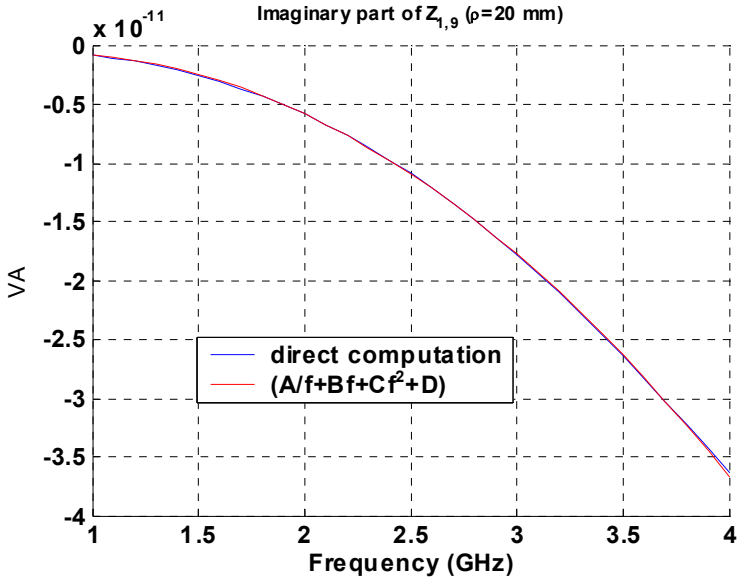

(b)

Fig. **4.3**: Comparison of impedance matrix elements derived by using the direct and interpolation methods ($\rho = 20\,mm$). (a) real part; (b) imaginary part.

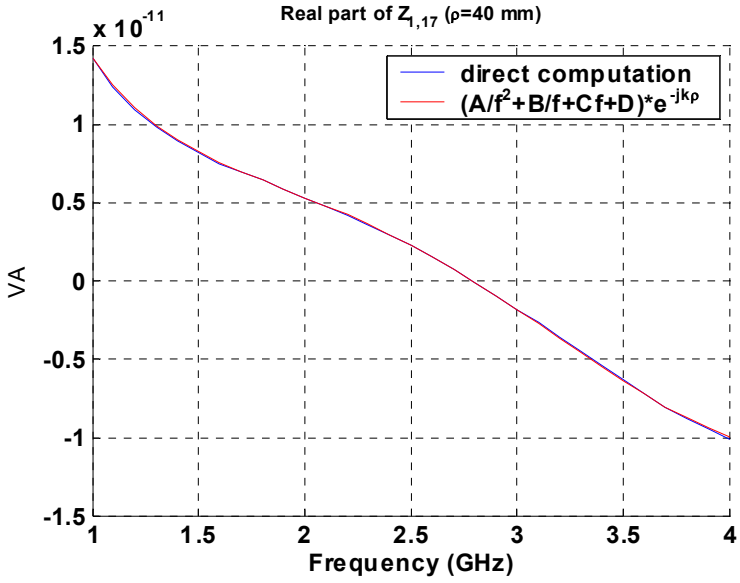

(a)

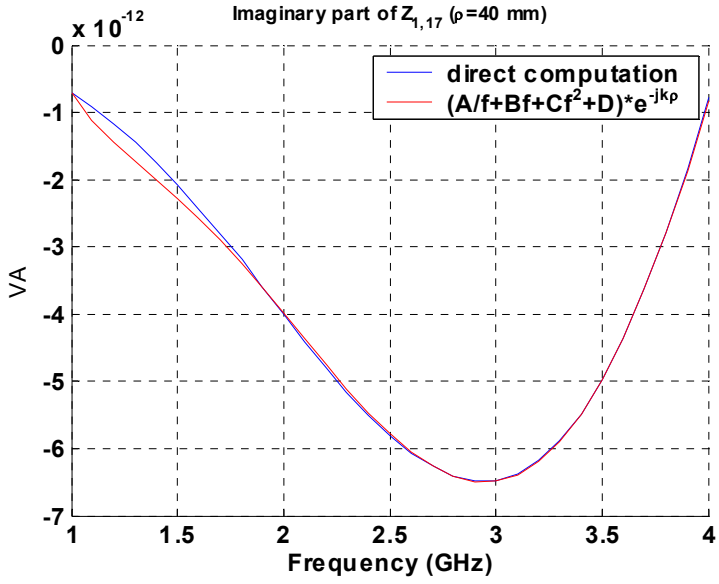

(b)

Fig. **4.4**: Comparison of impedance matrix elements derived by using the direct and interpolation methods ($\rho = 40\,mm$). (a) real part; (b) imaginary part.

4.3 Numerical results

In the previous section, we have presented the matrix interpolation algorithm along with the guidelines for choosing the frequency step and the threshold for phase extraction. The accuracy of the interpolation has been demonstrated by three matrix elements associated with three representative distance ranges. In this section, we apply this algorithm to several layered-structure problems to evaluate its accuracy and efficiency. For each example, we compare the S-parameters derived by using matrices computed by the direct and interpolation methods as well as the time requirements. The geometries chosen are: a patch antenna fed by a microstrip line; an interdigital bandpass filter; a hairpin bandpass filter; and a proximity-coupled patch.

4.3.1 Microstrip patch antenna

As our first example, we choose the patch antenna fed by a transmission line that we used to describe the matrix interpolation algorithm. The geometry is already shown in Fig. **4.1**, and it is discretized into rectangular cells, leading to a total of 730 unknowns. The patch antenna has two resonant frequencies at 2.25 GHz and 4 GHz, respectively, and the analysis is carried out for the frequency range of 1 to 5 GHz. We determine the frequency step by first estimating the upper limit of the frequency step by using (**4.10**). With the maximum separation distance being $119.6\,mm$, the upper limit of the frequency step Δf is about 1.25 GHz. Since this indicates the maximum frequency step allowed, we safely choose 1 GHz as the frequency step for the matrix sampling. In the first frequency

window, we generate impedance matrices directly at 1, 2, 3, and 4 GHz, and compute coefficients of the interpolating polynomials. Then, we slide the frequency window and sample impedance matrices at 2, 3, 4, and 5 GHz, and repeat the same procedure that we did for the first window. Since the matrices for 2, 3, and 4 GHz have been already computed in the first frequency window, only the impedance matrix for 5 GHz needs to be computed in the second frequency window.

Following the interpolation algorithm described in the previous section, the frequency variations of the matrix elements associated with the basis/testing function pair whose separation distance does not satisfy the criterion $\Delta k_w \rho > 3/4\pi$ are modeled directly, using (**4.11**) and (**4.12**). For the remainder of the matrix elements, the phase variation is first factored out, and then the coefficients of interpolating polynomials are calculated. Note that the free space wavenumber was used for this example since the source is located on top of the dielectric layer. Once the coefficients of the interpolating polynomials are computed, we perform the analysis for the entire frequency range. In Fig. **4.5**, the S-parameter of the patch antenna derived by using the direct matrix generation and the matrix interpolation are plotted together as a function of frequency, and we observe an excellent agreement between the two results. On a Pentium IV PC with a 2 GHz processor and a 1 Gbyte RAM, the time required for matrix generation by the direct computation was 256 sec, while that by the interpolation technique was only 35 sec.

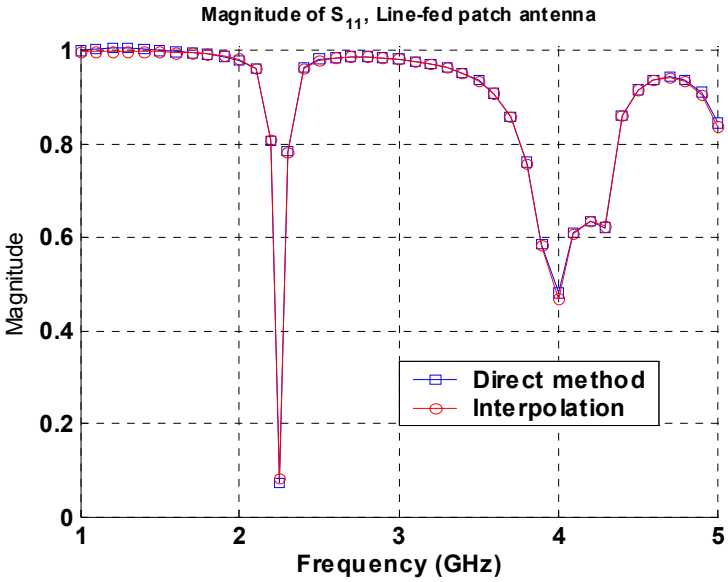

(a)

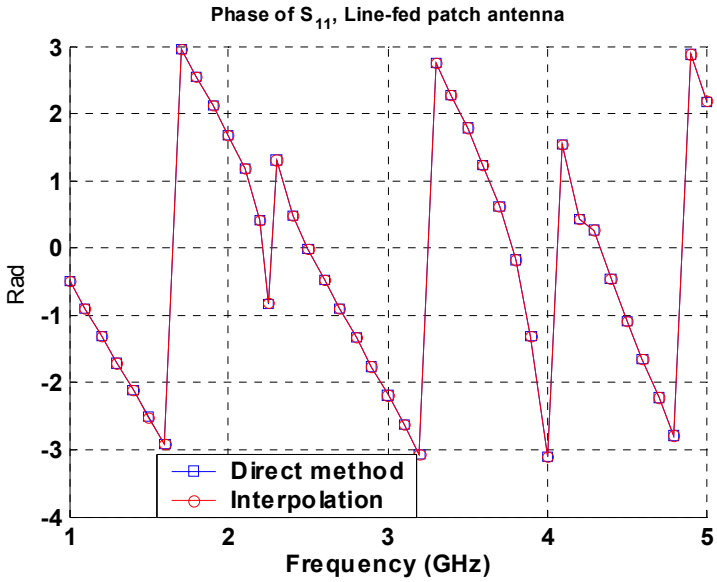

(b)

Fig. **4.5**: Comparison of S_{11} derived by using the direct and interpolation methods. (a) magnitude; (b) phase.

4.3.2 Interdigital bandpass filter

Consider an interdigital bandpass filter implemented on a single dielectric layer as illustrated in Fig. **4.6**. The geometry is divided into rectangular cells and rooftop basis functions are used to model the surface current leading to a total 1536 unknown. The geometry is analyzed for the frequency range of 3 to 6 GHz with 31 frequency points.

For the maximum radial separation distance of 12.6 mm , the maximum frequency step determined by (**4.10**) is 11.9 GHz. Since the entire frequency range is within the interpolation frequency step, we choose 1.0 GHz as the frequency step for the matrix interpolation. The impedance matrices are directly computed at frequencies 3, 4, 5, and 6 GHz, and the coefficients of the interpolating polynomials are determined by using the sampled matrices. Since the entire geometry lies within the threshold distance for the application of phase extraction, calculated by using (**4.14**), only (**4.11**) and (**4.12**) are used for the interpolation.

In Fig. **4.7**, the magnitude of the S-parameters, derived by using the direct and interpolation methods, are plotted as functions of frequency, and it is obvious that these two results are in very good agreement. The phase of the S-parameter derived by the two methods is compared in Fig. **4.8** and, again, indicates a very good match. On a Pentium IV PC with a 2 GHz processor and 1 Gbyte RAM, the time required for the direct computation was 556 sec while interpolation took only 85 sec.

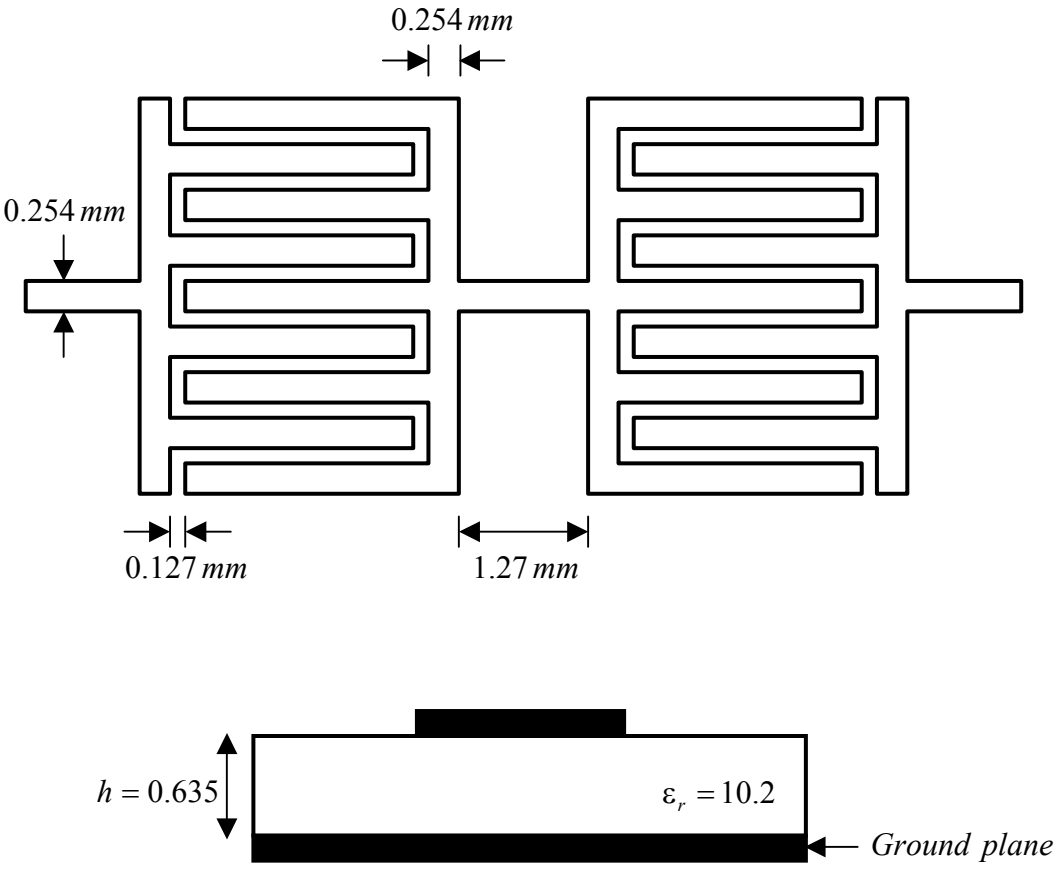

Fig. **4.6**: Geometry of an interdigital bandpass filter.

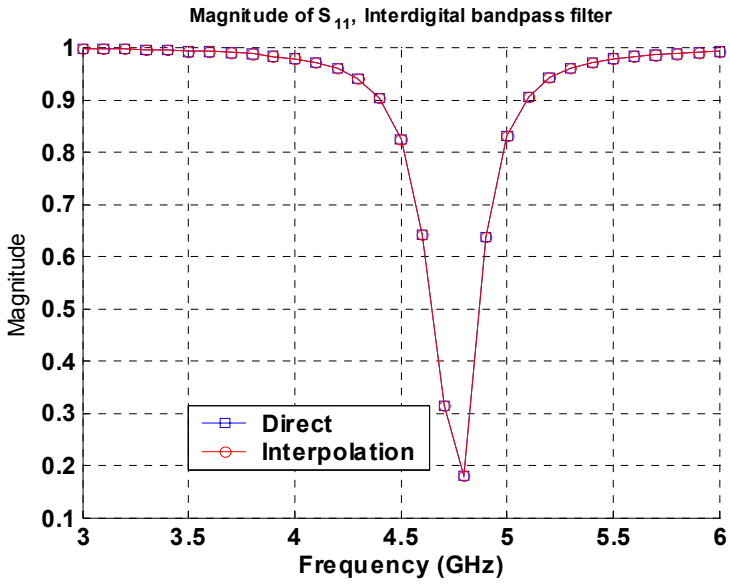

(a)

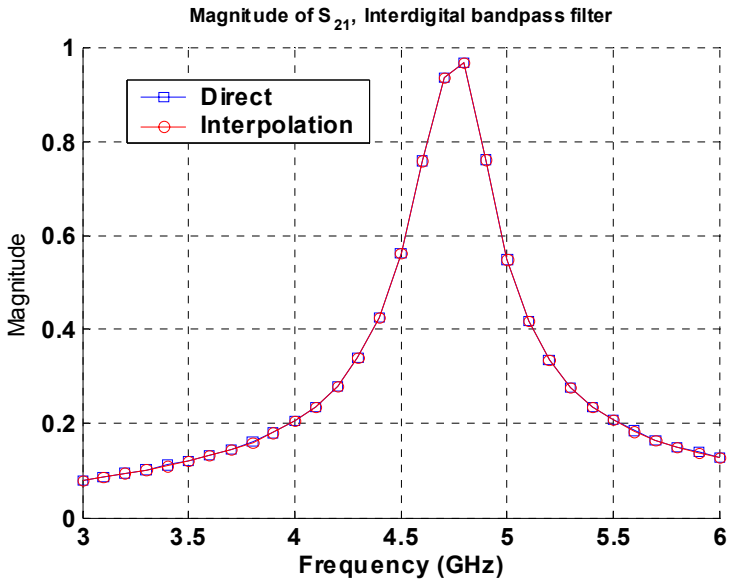

(b)

Fig. **4.7**: Comparison of S-parameters derived by using direct and interpolation methods. (a) magnitude of S_{11}; (b) magnitude of S_{21}.

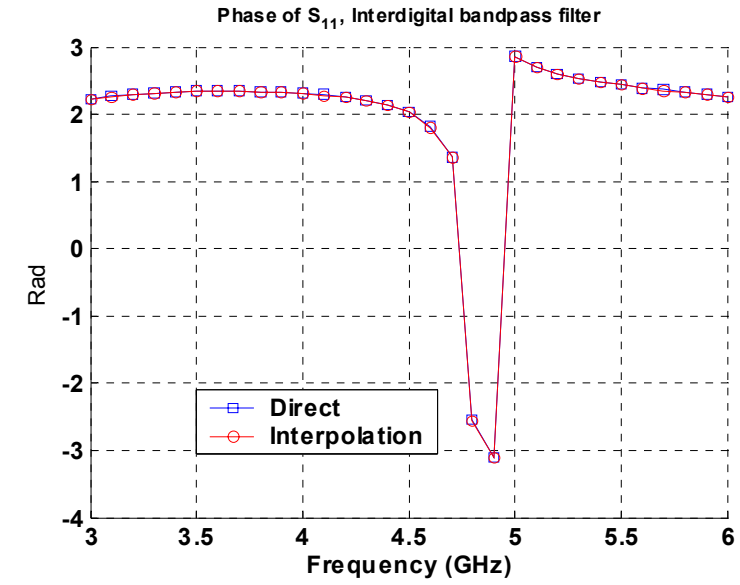

(a)

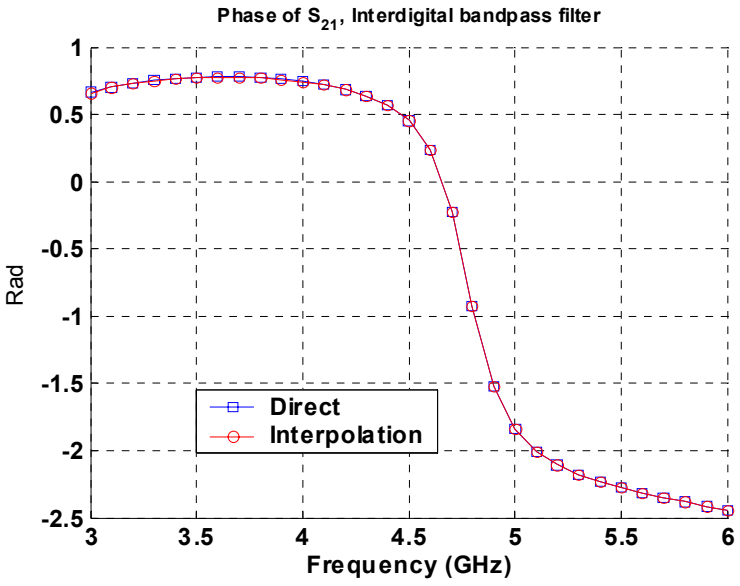

(b)

Fig. **4.8**: Comparison of S-parameters derived by using direct and interpolation methods. (a) phase of S_{11}; (b) phase of S_{21}.

4.3.3 Hairpin bandpass filter

The next example is a hairpin bandpass filter sitting on a dielectric layer with $\varepsilon_r = 9.8$, as shown in Fig. **4.9**. The dimensions are: $w = 0.2406\,mm$, $l_1 = 1.8045\,mm$, $l_2 = 1.5038\,mm$, $d_1 = 1.2632\,mm$, $d_2 = 1.5037\,mm$, $g_1 = 0.1805\,mm$, $g_2 = 0.3008\,mm$, and $g_3 = 0.1203\,mm$. The geometry is discretized into 532 cells, and the surface current is modeled by 786 rooftop basis functions. The analysis is performed for the frequency range of 11 to 13 GHz, and 41 frequencies are involved. Following the matrix interpolation algorithm, we first determine the interpolation frequency step, using (**4.10**). With the maximum distance being $18.7\,mm$, the upper limit for the interpolation frequency step is about 8 GHz. Since this is larger than the entire frequency band of the analysis, we choose 1 GHz as the interpolation frequency step. As in the previous example, the threshold value for the application of the phase extraction, $66.6\,mm$, is larger than the entire geometry, and only (**4.11**) and (**4.12**) are used for the interpolation.

The magnitudes of the S-parameters derived by the direct and interpolation methods are plotted in Fig. **4.10**. Once again, we observe very good agreement in both the magnitude of S_{11} and S_{21}. In Fig. **4.11,** the phase of S_{11} and S_{21} for the same cases are plotted as functions of frequency, and show very good agreement. On a Pentium IV PC with a 2 GHz processor and 1 Gbyte RAM, the time required for the direct computation was 21700 sec, but for the interpolation was 2170 sec.

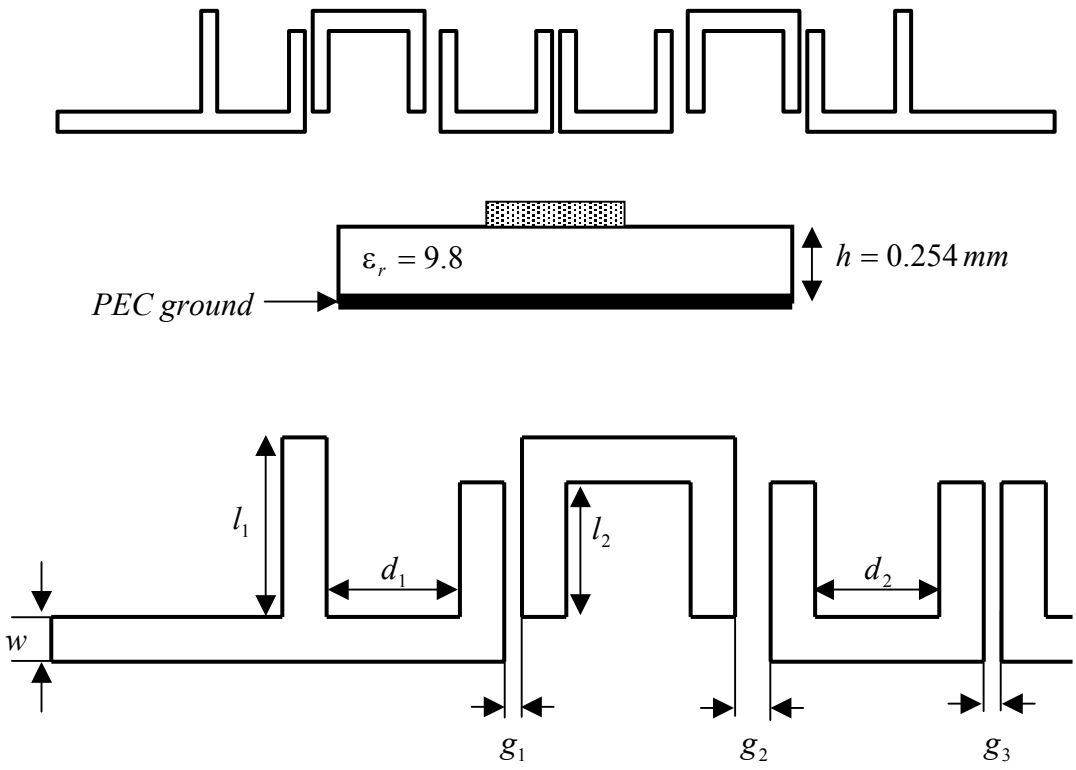

Fig. **4.9**: Geometry of a hairpin bandpass filter.

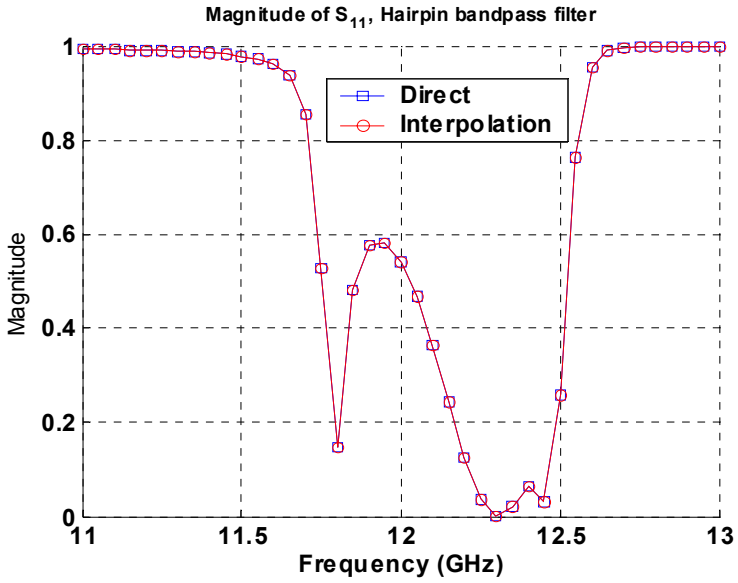

(a)

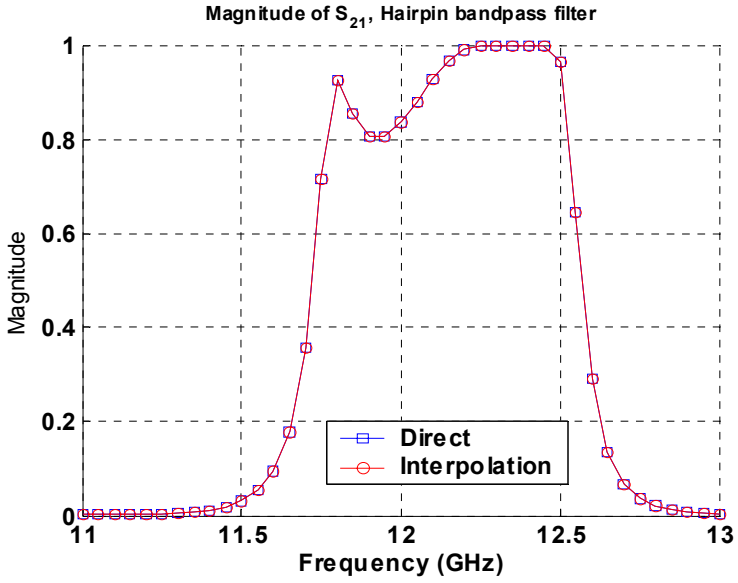

(b)

Fig. **4.10**: Comparison of S-parameters derived by using direct and interpolation methods. (a) magnitude of S_{11}; (b) magnitude of S_{21}.

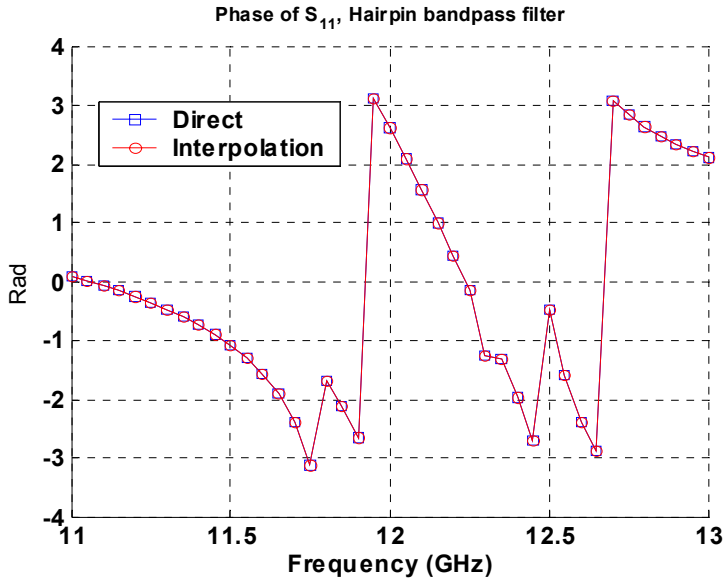

(a)

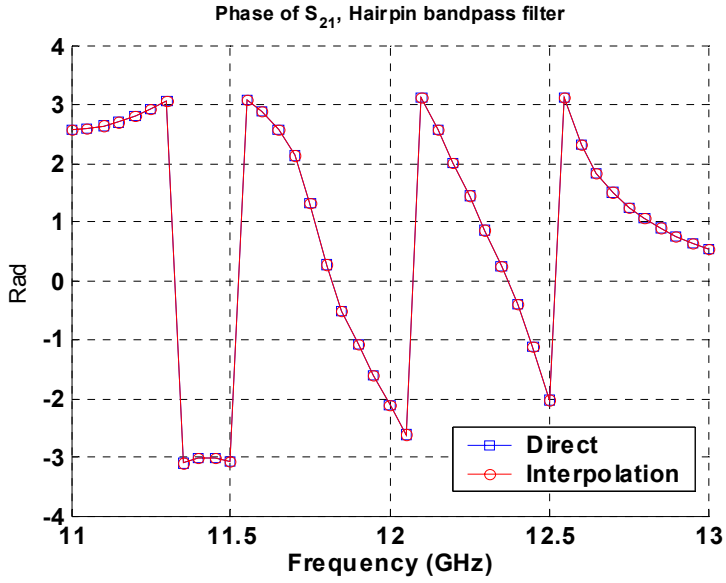

(b)

Fig. **4.11**: Comparison of S-parameters derived by using direct and interpolation methods. (a) phase of S_{11}; (b) phase of S_{21}.

4.3.4 Proximity couple patch

The last example is a proximity-coupled patch antenna with a resonant frequency at 3.6 GHz, whose geometry is depicted in Fig. **4.12**. The feed line is placed inside the dielectric, while the patch is printed on top of it. The antenna is discretized using rectangular cells, and the surface current is modeled by 1207 rooftop basis functions. The analysis is carried out for the frequency range of 2 to 5 GHz, and 31 frequency points are selected. The largest distance between the source and the field points is $77.8\,mm$, and the maximum frequency step derived from this value is about 1.3 GHz. We choose 1 GHz as the interpolation frequency step, and a single frequency window is required to cover the entire frequency range of interest. In the previous examples, the source and field points are located in the same layer, and the threshold distance for phase extraction was uniquely defined. However, in this example, the threshold distance depends on the location of the source points. If the source is located on the patch, the threshold distance is $19\,mm$, and if it is on the feeding line, the threshold is $28\,mm$. The impedance matrices at 2, 3, 4, and 5 GHz are computed by the direct method, and the interpolation coefficients for each matrix element are determined by using them. In Fig. **4.13**, the magnitude and phase of S_{11} derived by the direct and interpolation methods are plotted as functions of frequency and, again, we observe excellent agreement. On a Pentium IV PC with a 2 GHz processor and 1 Gbyte RAM, the time required for matrix computation by the direct method was 453 sec, while the interpolation technique took only 65 sec. Table **4-1** presents a comparison of the computation times for the proposed interpolation

technique and the direct matrix computation for the examples studied in this chapter. The time advantage is obvious.

Table 4-1: Comparison of the impedance matrix generation times for sample problems (Pentium IV 2 GHz, 1 GByte RAM)

Geometry	Number of unknowns	Time (sec)	
		Direct	Matrix interpolation
Line-fed patch	730	256	35
Interdigital bandpass filter	1536	556	85
Hairpin bandpass filter	786	21700	2170
Proximity-coupled patch	1207	453	65

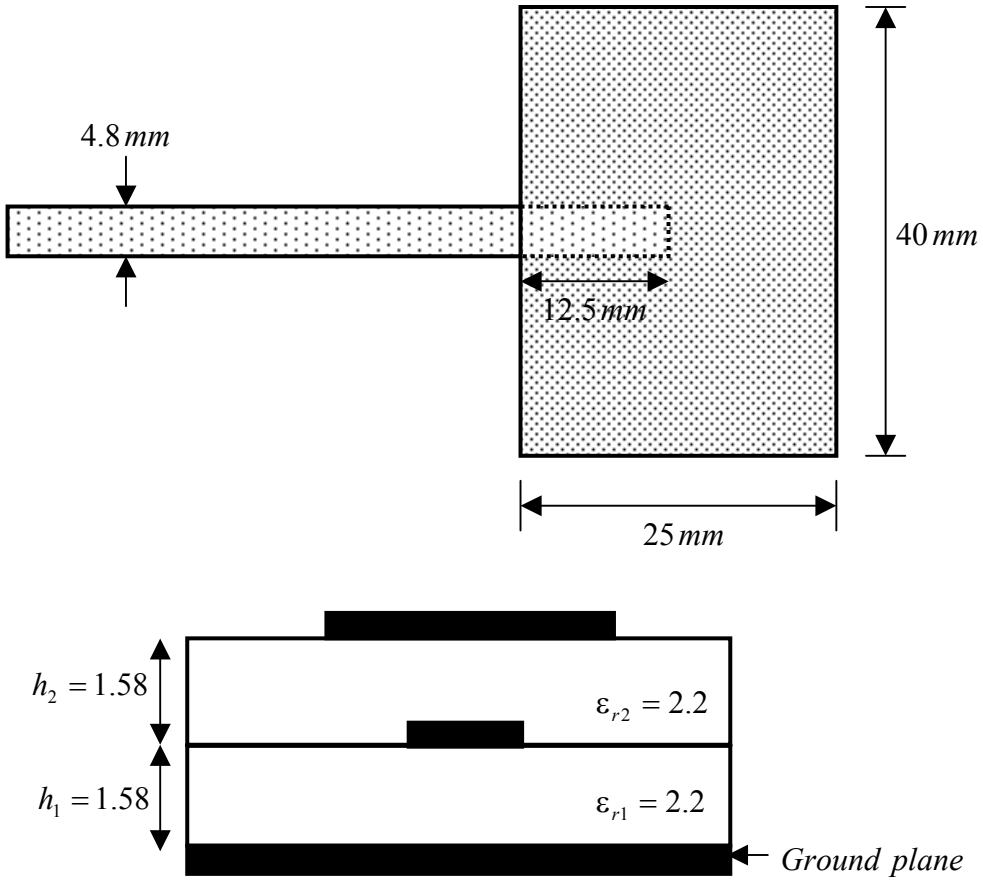

Fig. **4.12**: Geometry of the proximity-coupled patch.

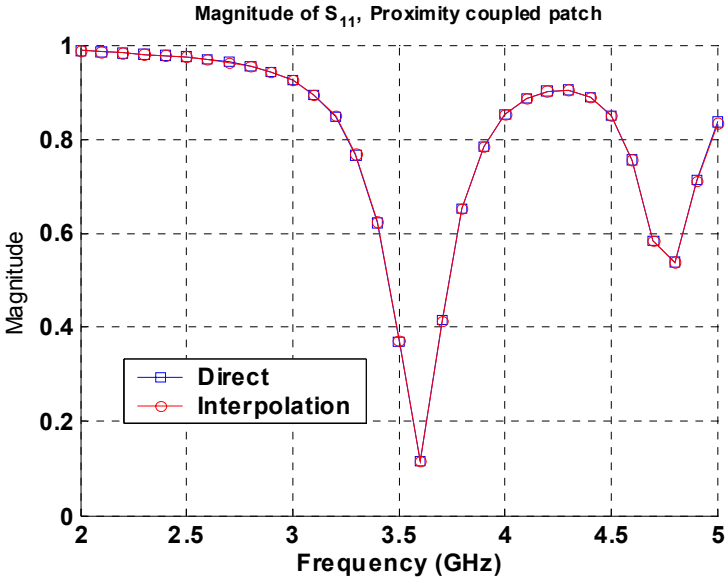

(a)

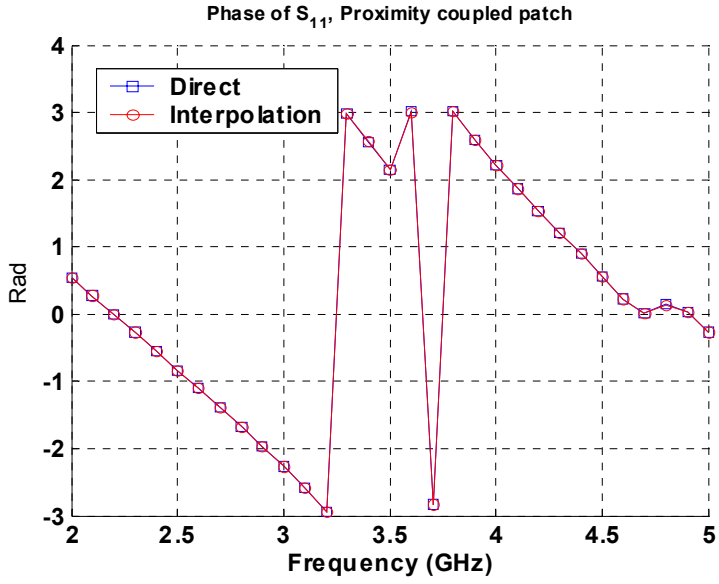

(b)

Fig. **4.13**: Comparison of S_{11} derived by using direct and interpolation methods. (a) magnitude; (b) phase.

4.4 Conclusions

In this chapter, we have presented a new and efficient impedance matrix interpolation scheme for the analysis of printed layered structures. It has been demonstrated that the final parameters derived by using the direct and interpolation methods are in very good agreement as are the impedance matrix elements. Since the proposed algorithm is robust and systematic, it can be readily incorporated into existing codes. It is important to note that once the coefficients of the interpolating polynomials are determined, adding more frequency points in the analysis requires very little additional computation time. Therefore, the time advantage of the matrix interpolation increases with the increase in the number of frequency points. Although this algorithm was applied to layered structures, it is equally applicable to other classes of problems, such as the radiation and scattering in free space.

Chapter 5

CHARACTERISTIC BASIS FUNCTION METHOD (CBFM)

5.1 Introduction

The competitive market environment in the communication industry has fueled the demand for shorter turn-around times for the design of products such as cellular phones. This, in turn, has challenged the development of field solvers and related simulation tools to enhance the efficiency and accuracy of the microwave circuit CAD tools to reduce the time-to-market. One approach to accelerating the design process is to use a circuit simulator, as opposed to a full-wave field solver. In this approach, the microstrip discontinuities are modeled by lumped elements, and the system, which includes active devices in general, is analyzed by using a network-theory-based algorithm. While a network-theory type of circuit simulator requires a much smaller CPU time and memory than its full-wave electromagnetic counterpart, and produces fairly accurate results at low frequencies where the level of coupling between different domains is relatively small, its accuracy degrades rapidly with an increase in the operating frequency, owing to the neglect of the parasitic coupling effects. Thus, it is almost always necessary to validate and iterate on the prototype design based on the network-theory-based circuit simulator, by using a full-wave electromagnetic solver, before the package can be readied for manufacturing.

The most commonly used full-wave EM solver for microstrip circuit design is based on the Method of Moments (MoM) algorithm. Though numerically rigorous, and hence accurate, the MoM is computationally intensive, often requiring CPU time and memory that are orders of magnitude greater than those of the conventional network-theory-based solver [28]. The simulation of a single circuit element by MoM can sometimes take tens of minutes of CPU time per frequency, and this makes it difficult to incorporate the MoM solver into the design process, which often requires repeated modification and analysis of a circuit to achieve the desired performance. For the reasons indicated above, the use of full-wave electromagnetic simulation is often limited either to final design verification, or to a model development of the discontinuity for future use.

In the past, many researchers have attempted to reduce the complexity and accelerate the computational speed of the MoM. For instance, the Fast-Multipole Method (FMM) [29] has been proposed to reduce the computational cost of matrix-vector multiplication when using an iterative solver, though primarily for perfectly conducting objects. The impedance matrix localization (IML) method [30] for matrix sparsification has been developed, again for a limited class of scattering problems involving PEC bodies, to expedite matrix-vector multiplication. Wavelet transform [31] has also been used to yield sparse matrices that can be solved rapidly, though it is not as robust an approach as one might desire.

Another emerging approach for efficient MoM analysis of microstrip structure is based on the concept of segmentation or domain decomposition, and several techniques have been proposed to implement this concept. For instance, in [32], the modified diakoptic theory [33], originally proposed for antenna problems, has been secondly

applied to microstrip structures, though its use has been relatively limited. The same is true for the diakoptic-theory-based Multilevel Moments Method (MMM) [34], which carries out an iterative basis function refinement to solve passive planar structure problems. The Subdomain Multilevel Approach (SMA), which utilizes the so-called Macro Basis Functions (MBFs) [35], is a novel technique for reducing the matrix size associated with large planar antenna array problems.

In this work we present an efficient technique for microstrip MMIC analysis, called the Characteristic Basis Function Method (CBFM), which has been successfully implemented not only for the analysis of planar microstrip antennas in [36] and [37], but also for scattering problems involving arbitrary, three-dimensional, faceted surfaces [38]. In this method, the problem geometry is first segmented into sections, for which high level basis functions, called the Characteristic Basis Functions (CBFs) that are aggregations of the conventional subdomain bases, are generated. These CBFs not only represent the unique electromagnetic characteristic of each section, but also include the mutual coupling effects between different sections.

The CBFM is different from some of the other domain decomposition methods in several ways. First, in this method, the parasitic coupling is taken into account in a systematic and efficient manner by using the secondary CBFs, rather than via the use of iterative refinement. Instead, the CBFM leads to a reduced matrix, which is much smaller than the original one, and this obviates the need for iterative solution of problems requiring a large number of unknowns. Second, unlike in [34], which aggregates upper-level bases of two adjacent sections to form a single basis, the CBFM approach defines the bases for each individual section, allowing increased flexibility and degrees of

freedom for a given segmentation process. In the following, the CBFM method is detailed in Section 2; validation of the CBFM with numerical examples is given in Section 3; finally, some concluding remarks are presented in Section 4.

5.2 Theory and algorithm

5.2.1 Introduction to Characteristic Basis Function Method (CBFM)

As mentioned in the preceding section, the first step in the CBFM is to segment the original geometry into smaller regions – called sections – that are fractional in size of the original geometry, as for instance in the example shown in Fig. **5.1**. Typically, two types of CBFs are defined for each section, *viz.*, the primary and the secondary, though higher-order (for example, tertiary) basis functions may also be included, if necessary. The primary CBFs are solutions for the induced current in the isolated sections, whereas the secondary CBFs account for the field coupling between the sections. The CBFs are generated by solving relatively small-size matrix equations, as compared to the original matrix. These matrices are diagonal blocks, as shown in Fig. **5.2** and, hence, the time needed to generate these CBFs is usually reasonably small. In general, the level of field coupling between the sections is governed by such parameters as the geometry and the frequency, and we can take advantage of this fact by discarding some of the secondary CBFs, in a dynamic manner, using a thresholding scheme. Regardless of whether the thresholding scheme is used or not, the set of primary and secondary CBFs are employed as high level basis and testing functions to generate a reduced matrix via the use of the

Galerkin method. This resulting matrix is typically quite small and, hence, can be solved directly without resorting to iterative procedures, whose convergence can be problematic for some problems, especially in the neighborhood of resonances.

Having introduced the basic concept of the CBFs, we proceed below with the details of their generation.

5.2.2 Generation of CBFs

The generation of primary CBFs begins with the definition of the appropriate interface planes between adjacent sections, followed by placement of each of the sections in an isolated environment, in which the coupling with all other sections are ignored. The number of primary CBFs of a section depends on the connectivity of the sections. For instance, we define two primary CBFs for the example geometry shown in Fig. **5.1**, in which each section has two interfaces with the adjacent sections, with the exception of section-1 and section-8. Next, to minimize the termination at the interface, we deliberately introduce small extensions, which provide overlap/transition regions between the sections, by removing the ports for the individual regions slightly away from the interface. Block diagonal matrices associated with these extended domains are shown pictorially in Fig. **5.2**, for a typical section, say section-*i*.

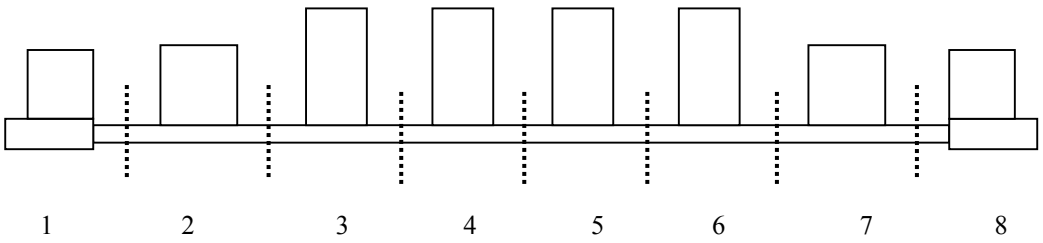

Fig. **5.1**: Segmentation of the lowpass filter. Dotted lines and numbers indicate the borders between sections and the section numbers, respectively.

The matrices relate the voltages and currents in each section via the equation (**5.1)**

$$[Z'_{i,i}][I'_{i,m}]=[V'_{i,m}] \qquad \begin{cases} i=1,2,\cdots,S \\ m=1,2,\cdots,NP_i \end{cases} \tag{5.1}$$

where $[Z'_{i,i}]$ is extended diagonal block matrix of section-*i*, $[I'_{i,m}]$ and $[V'_{i,m}]$ are the m th extended induced current and excitation of section-*i*, respectively; S is the number of sections; and, NP_i is the number of primary CBFs of section-*i*. The isolated problem for this section (extended) is solved and the primary CBFs are derived by retaining only those entries that belong to the original section. Next, the primary CBFs are generated for the other sections by repeating the same procedure for the individual sections. With few exceptions, we need to augment the primary CBFs with secondary CBFs that account for the coupling between the sections. Extensive numerical experiments have shown that the inclusion of second-order coupling (secondary CBFs) is adequate for producing accurate results, though higher-order bases may be added on as-needed basis, if desired.

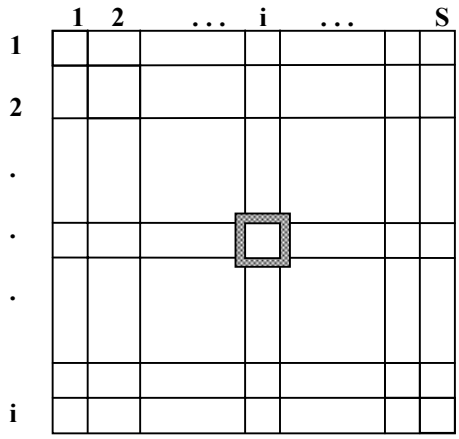

Fig. **5.2**: Block impedance matrix of the original problem. Diagonal matrix for section-i is extended, and this part is indicated by the shaded region.

The secondary CBFs are calculated by solving the equation

$$[Z_{i,i}][I_{i,m}] = [Z_{i,j}][I_{j,exc}] \qquad \begin{cases} i = 1,2,\cdots,S \\ m = NP_i + 1, NP_i + 2, \cdots, NT_i \end{cases} \qquad (5.2)$$

where $[Z_{i,i}]$ is the block diagonal matrix associated with section-*i*; $[Z_{i,j}]$ is the block off-diagonal matrix that describes the interaction between the sections *j* and *i*; $[I_{i,m}]$ is the induced current in section-*i* due to the current in section-*j*; $I_{j,exc}$ is the currents in section-*j* ; and NT_i is the total number CBFs for the section-*i*. Note that the right-hand side of (**5.2**), *i.e.*, the excitation source, may be physically interpreted as the electric field impressed on section-*i* due to the current in section-*j*. The current $I_{j,exc}$, appearing in the same right-hand side, can correspond to either a primary or a secondary CBF, depending on the order of the coupling (secondary or tertiary) that the solution of the equation is

intended to represent; specifically, if $I_{j,exc}$ is the primary (secondary) CBF, the solution of (5.2), *viz.*, $I_{i,m}$, then, is the secondary (tertiary) CBF. In (5.2), the right-hand side is a simple matrix-vector multiplication, and the left-hand side involves a block diagonal matrix, $[Z_{i,i}]$, whose LU decomposition is available from the generation of the primary CBF, which has been carried out previously. Hence, this process is not as time-consuming as that of constructing the primary CBFs.

5.2.3 Thresholding the secondary CBFs

As briefly mentioned during the introduction of the CBFM, the level of field coupling between the sections is governed by such parameters as the geometry and the frequency, and some of the secondary CBFs can be discarded in a dynamic manner by employing a thresholding scheme. The decision whether or not to include a secondary CBF is based on the criterion.

$$\begin{cases} Use & if \quad \|I_{\text{sec}}\| / \|I_{pri}\| \geq \varepsilon \\ Discard & if \quad \|I_{\text{sec}}\| / \|I_{pri}\| < \varepsilon \end{cases} \tag{5.3}$$

where $\|I_{\text{sec}}\|$ is the vector 2-norm of the secondary CBF induced by I_{pri}, $\|I_{pri}\|$ is the vector 2-norm of the primary CBF, and ε is the threshold value. The set of primary and secondary CBFs obtained by applying the above criterion includes only the dominant secondary CBFs, and this process minimizes the number of total CBFs without sacrificing the accuracy. The dimension of the reduced matrix, constructed by using the

set of CBFs as the basis and the testing functions, is relatively small; hence, the matrix can be easily solved by direct methods and it is unnecessary to use iterative techniques.

5.2.4 Construction of reduced matrix and its solution

For a planar microstrip structure, the induced current $\mathbf{J}_s$ satisfies the equation

$$\mathbf{L}\mathbf{J}_s = \mathbf{E}_i \tag{5.4}$$

where $\mathbf{L}$ is the integral operator, and $\mathbf{E}_i$ is the impressed electric field. The induced current can be expanded as

$$\mathbf{J}_s = \sum_{j=1}^{N} \alpha_j \mathbf{f}_j \tag{5.5}$$

where N is the number of basis functions $\mathbf{f}_i$, and α_i is the unknown coefficient to be determined. Using this expansion, (5.4) can be written as

$$\sum_{j=1}^{N} \alpha_j \mathbf{L}\mathbf{f}_j = \mathbf{E}_{exc} \tag{5.6}$$

By taking the inner product with appropriate testing functions, (5.6) is transformed into a linear system

$$\sum_{i=j}^{N} \alpha_j \left\langle \mathbf{w}_i, \mathbf{L}\mathbf{f}_j \right\rangle = \left\langle \mathbf{w}_i, \mathbf{E}_{exc} \right\rangle \quad i = 1,2,\cdots,N \tag{5.7}$$

where $\mathbf{w}_i$ are the testing functions; specifically, $\mathbf{w}_i = \mathbf{f}_i$ when the Galerkin Method is used. Finally, using the matrix notation, (5.7) can be written

$$[\mathbf{Z}][\mathbf{I}] = [\mathbf{V}] \tag{5.8}$$

where $[\mathbf{Z}]$ is the impedance matrix of dimension $N \times N$ with elements $\langle \mathbf{w}_i, \mathbf{Lf}_j \rangle$; $[\mathbf{I}]$ is the solution of dimension $N \times 1$ with elements α_j; and, $[\mathbf{V}]$ is the excitation vector of dimension $N \times 1$ with elements $\langle \mathbf{w}_i, \mathbf{E}_{exc} \rangle$. In the matrix equation (**5.8**), $[\mathbf{I}]$ is now expanded by using the set of CBFs, generated previously by using the process described earlier. We write:

$$[\mathbf{I}] = \sum_{k=1}^{M} \beta_k [\mathbf{I}_k^c] \tag{5.9}$$

with

$$M = \sum_{i=1}^{S} NT_i \tag{5.10}$$

where M is the total number of CBFs including both the primary and the secondary, $[\mathbf{I}_k^c]$ is k th CBF, and β_k is the coefficient of k th CBF. By inserting (**5.9**) into (**5.8**), we get

$$[\mathbf{Z}][\mathbf{I}^c][\boldsymbol{\beta}] = [\mathbf{V}] \tag{5.11}$$

where $[\mathbf{I}^c]$ is the matrix form of CBFs of dimension $N \times M$, $[\boldsymbol{\beta}]$ is the coefficient vector of dimension $M \times 1$. By using the transpose of $[\mathbf{I}^c]$ as the testing function, we obtain the final form of new, reduced matrix equation, which reads

$$[\mathbf{I}^c]^T [\mathbf{Z}][\mathbf{I}^c][\boldsymbol{\beta}] = [\mathbf{I}^c]^T [\mathbf{V}] \tag{5.12}$$

or, in a simpler form

$$[\mathbf{Z}^c][\boldsymbol{\beta}] = [\mathbf{V}^c] \tag{5.13}$$

where $[\mathbf{Z}^c] = [\mathbf{I}^c]^T [\mathbf{Z}][\mathbf{I}^c]$ and $[\mathbf{V}^c] = [\mathbf{I}^c]^T [\mathbf{V}]$. Typically *M*, the dimension of the reduced matrix, is much smaller than that of the original matrix equation (*N)*, and the reduced matrix equation can be solved directly. Once the coefficients of the reduced matrix equation have been obtained, the solution for the original problem is readily recovered from the equation

$$[\mathbf{I}] = [\mathbf{I}_c][\boldsymbol{\beta}] \tag{5.14}$$

Having discussed the derivation of the reduced matrix equation, we next apply it in the next section to some test examples, such as filter and amplifier circuits, to demonstrate its numerical efficacy.

5.3 Numerical results

In this section, the CBFM–developed in the previous two sections is applied to several examples, and numerical results are derived to illustrate its numerical efficiency. In the first example, the CBFM is applied to a microstrip meander line filter for three different threshold values, to demonstrate the use of the thresholding procedure. In the second and third example, we analyze a bandpass filter and the passive components of a two-stage amplifier, respectively. The CBFM is again used for these problems in conjunction with the thresholding scheme.

5.3.1 Meander line

The first example, shown in Fig. 5.3, is a simple meander line on a dielectric substrate ($\varepsilon_r = 2.43$, thickness=0.49 mm) with W=1.41 mm, S=2.82 mm and L=29.61 mm. In the conventional Method of Moments analysis, the geometry is discretized into 624 rectangular cells using rooftop basis functions and this leads to 1039 unknowns. The CBFM is implemented for this geometry over the frequency range 9 to 11.5 GHz, the computational time is determined and the accuracy of S-parameters is evaluated.

We begin by segmenting the geometry into 8 sections as shown in Fig. 5.3, though such a segmentation is by no means unique. Next, we generate the primary and the secondary CBFs, and impose three different thresholding levels on the secondary CBFs. We compare the performances of each of these thresholding schemes in terms of

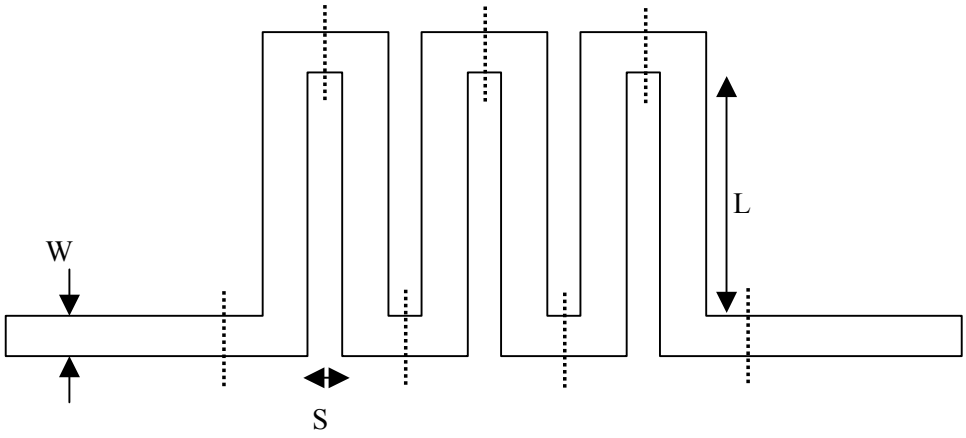

Fig. 5.3: Meander line. Dotted lines separate the sections.

time requirement and accuracy achieved. In the first scheme, we include no secondary CBFs, and this is tantamount to using an infinite threshold value. Fig. **5.4** plots the S-parameters obtained from both the direct solution and the CBFM for the sake of comparison. Except for minor differences near the resonance and at the frequencies below 9.5 GHz, the S-parameters derived from the CBFM match well with those obtained from the direct solution, and this can be attributed to a relatively small level of field coupling between the sections. The numbers of total CBFs are plotted in Fig. **5.7**, as a function of the frequency, and we note that this number remains unchanged over the frequency band. In the second case, we include all of the secondary CBFs, leading to a total of 128, and this corresponds to using a zero threshold value. In Fig. **5.5**, the S-parameters calculated from the CBFM with this threshold value are compared with those from the direct solution.

The various S-parameter plots, derived by the CBFM, are seen to be indistinguishable from those obtained from the direct solution, and this is not totally unexpected since we have now included all the first-order mutual coupling effects. Obviously, the total number of the CBFs used is now considerably larger, and, consequently, the time requirement is also much larger than the first case where no thresholding was used. Finally, we move to the third case, where we use a suitable threshold value and include only those secondary CBFs whose vector norm is larger than this tolerance value; thus, we retain only those CBFs that represent the dominant mutual coupling effects. For the meander line example, we use 0.5 for the threshold value, and the S-parameters and the number of CBFs used are plotted as functions of frequency in Fig. **5.6** and **5.7**, respectively.

Since the thresholding is imposed dynamically in this case, the number of secondary CBFs retained varies with frequency, though typically this number ranges from 42 to 44, as opposed to 128 CBFs in the second case. The S-parameters obtained by using this threshold value and those derived from the direct solution are again seen to essentially coincide with each other–with virtually no noticeable difference between the two–indicating that the chosen thresholding level was adequate for the desired accuracy. Table **5-1** indicates the total solve time for the meander line problem over the operation frequency band for the three cases. It is evident from this table that using a thresholding scheme is the best strategy for determining the number of the secondary CBFs to be retained.

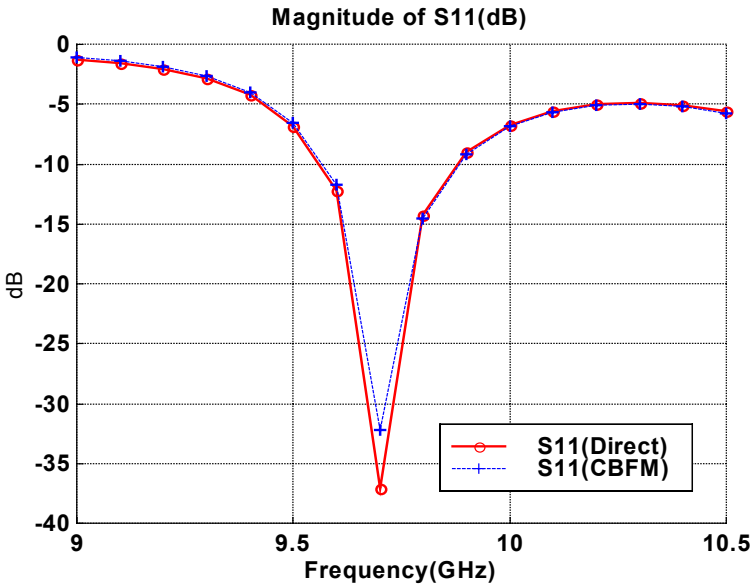

(a)

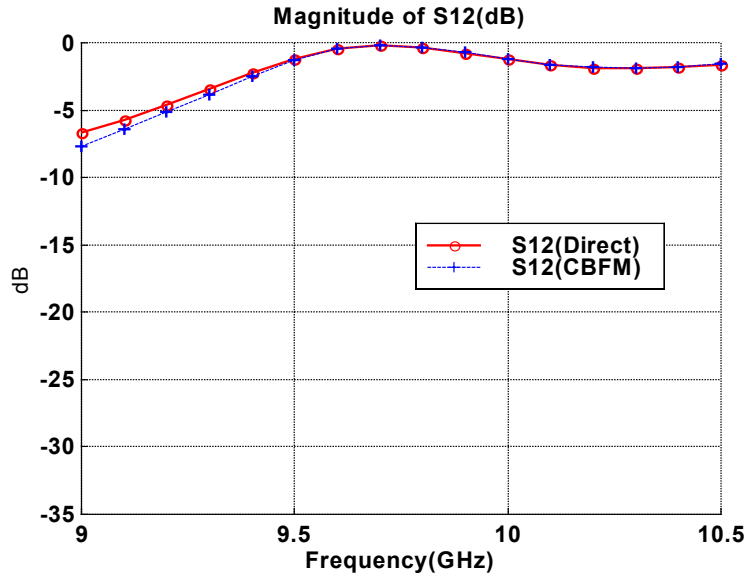

(b)

Fig. **5.4**: Comparison of the S-parameters of the meander line calculated by using the CBFM and the direct method. Only primary CBFs were used. (a) Magnitude of S_{11}; (b) Magnitude of S_{12}.

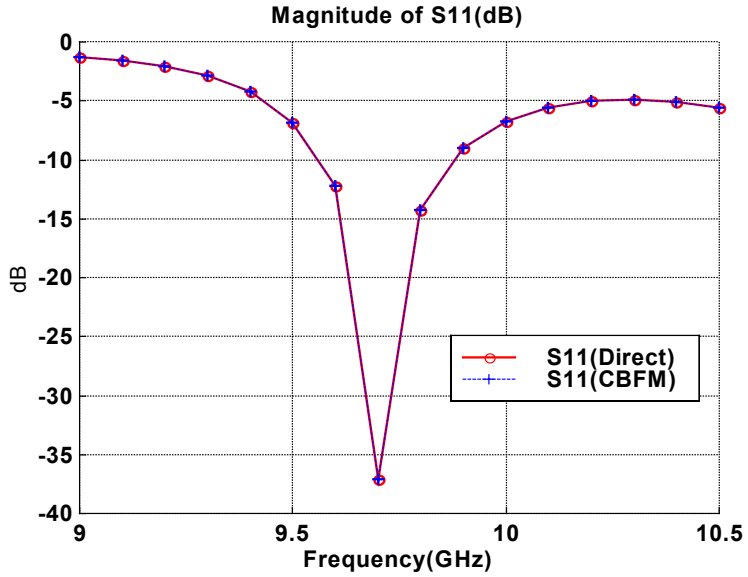

(a)

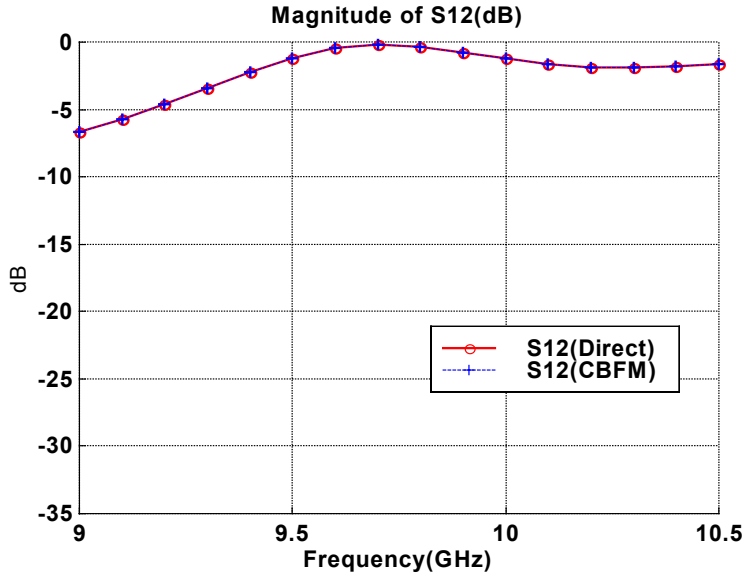

(b)

Fig. **5.5**: Comparison of S-parameters of the meander line calculated by using the CBFM and direct method. Primary CBFs and all of the secondary CBFs were used. (a) Magnitude of S_{11}; (b) Magnitude of S_{12}.

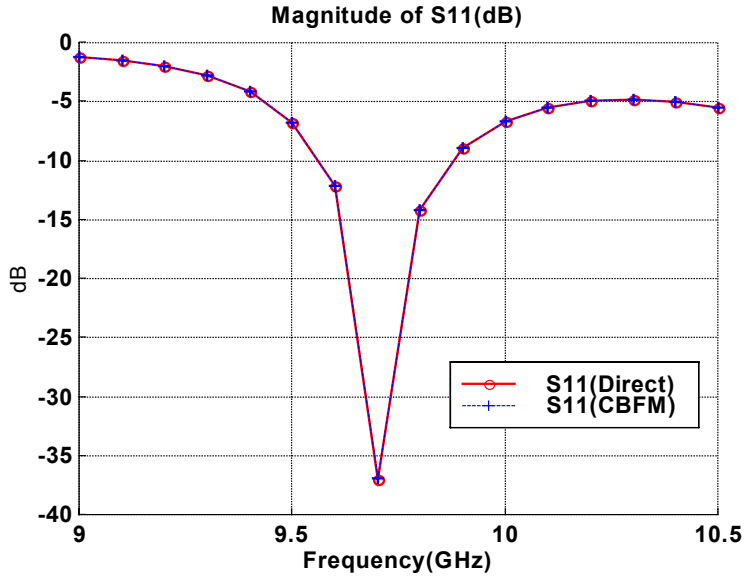

(a)

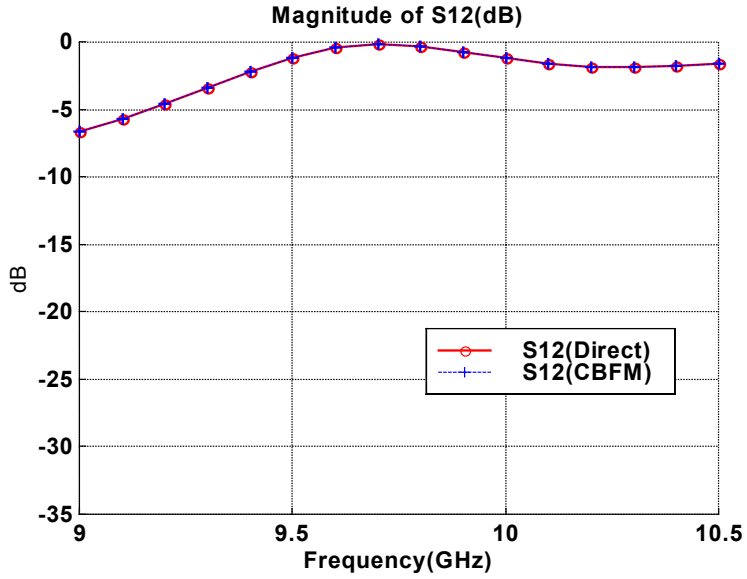

(b)

Fig. **5.6**: Comparison of the S-parameters of the meander line calculated by using the CBFM and the direct method. Primary CBFs and secondary CBFs with thresholding were used. (a) Magnitude of S_{11}; (b) Magnitude of S_{12}.

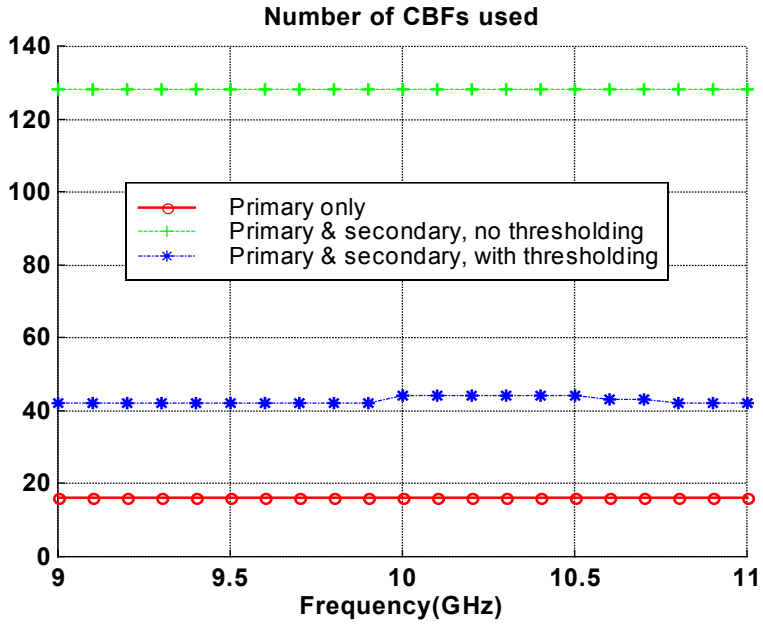

Fig. **5.7**: Number of the CBFs as functions of the frequency for the meander line, when different criteria are used.

Table **5-1**: Comparison of the total solve times for the meander line over the frequency band 9 GHz to 10.5 GHz, when different criteria are used.

	Time (sec)
Primary only	37.12
Primary & secondary, no thresholding	99.71
Primary & secondary, with thresholding	48.54
Direct solving	396

5.3.2 Bandpass filter

Next, we consider a microstrip hairpin filter geometry on a 10 mil (0.254 mm) Alumina ($\varepsilon_r = 9.8$) substrate with W=9.5 mil, S1=9.5 mil, S2=11.4 mil, S3=3.8 mil and L=60.8 mil, as shown in Fig. **5.8**. For this geometry, the conventional Method of Moments requires 1482 unknowns when using the rooftop basis functions. For this geometry, each element of the filter is isolated and, hence, segmentation of the geometry is intuitively obvious. The segmentation is shown in Fig. **5.8**, and it leads to a total of 6 sections. The CBFM is again implemented over the frequency band, 11 GHz to 13 GHz, and the S-parameters derived from both the CBFM and the direct solution are compared in Fig. **5.9**, while the number of total CBFs used is plotted in Fig. **5.10**. For this example, 28 CBFs are used with thresholding, throughout the frequency band, with the exception of three frequencies, and the number increases to 60 when all the secondary CBFs are retained. We note that, as in the previous example, the S-parameters derived from the CBFM show very good agreement with those obtained from the direct solution. Table **5-2** summarizes the time requirements for each of these solutions. We note that we can achieve a ten-fold acceleration of the solve time over the direct method–by using the CBFM with thresholding–without compromising the accuracy of the solution.

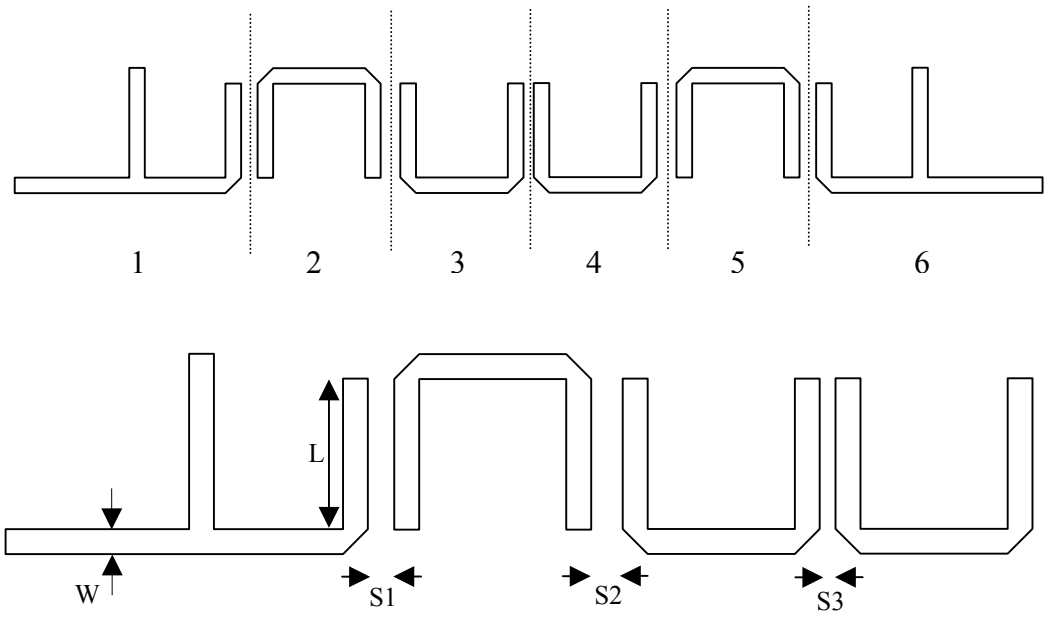

Fig. **5.8**: Bandpass filter. (a) Entire bandpass filter geometry. (b) Designation of geometrical parameters.

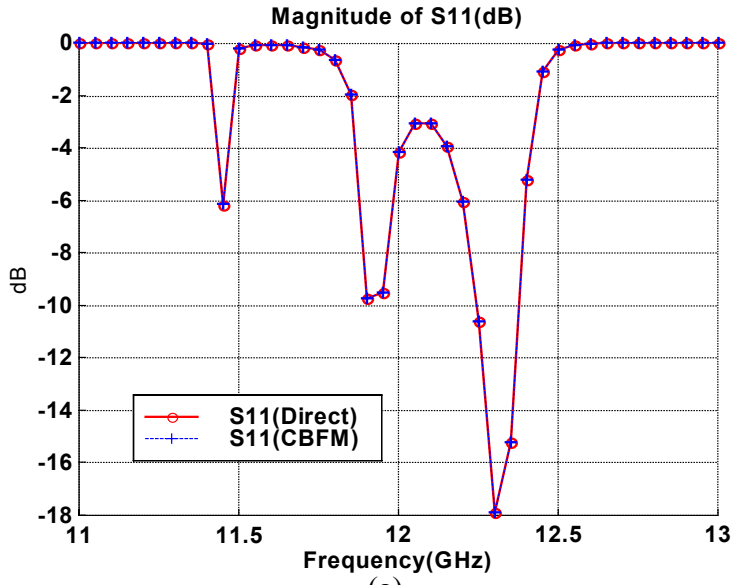

(a)

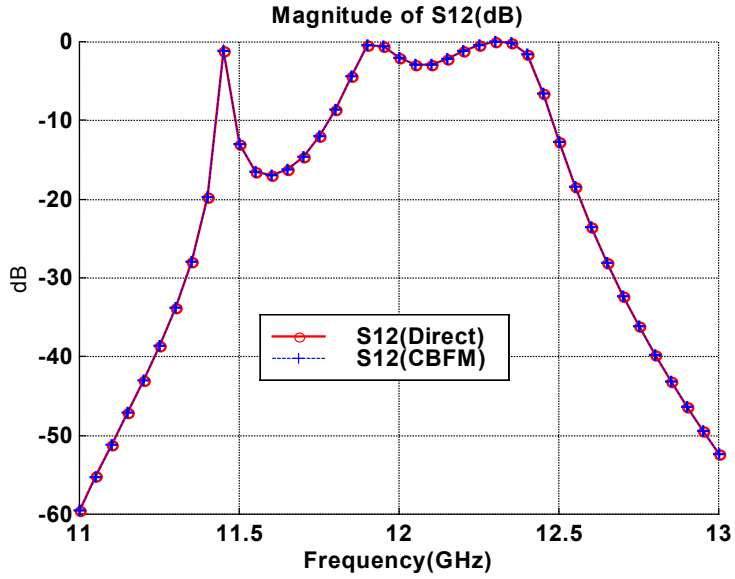

(b)

Fig. **5.9**: Comparison of the S-parameters of the bandpass filter, computed by using the primary and secondary CBFs with thresholding, and the direct method. (a) Magnitude of S_{11}; (b) Magnitude of S_{12}.

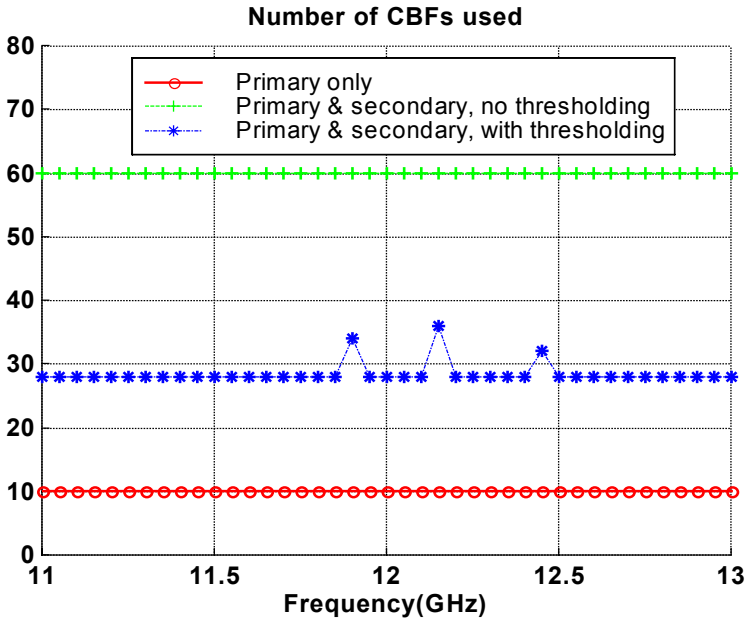

Fig. **5.10**: Number of CBFs as functions of the frequency used to analyze the bandpass filter, when different thresholding criteria are used.

Table **5-2**: Comparison of the total solve times for the bandpass filter over the frequency band of 11 GHz to 13 GHz, between the CBFM using the primary and the secondary CBFs with thresholding, and the direct method.

	Time (sec)
Primary & secondary, with thresholding	207
Direct solving	2561

5.3.3 Two-stage amplifier

For the last example, we present the simulation results of the passive components of a two-stage amplifier circuit on a 10 mil (0.254 mm) Alumina ($\varepsilon_r = 9.8$) substrate, which requires 1819 unknowns when the conventional Method of Moments is used. The geometry is segmented into 7 sections, as shown in Fig. **5.11**, and is simulated over the frequency band of 8 to 14 GHz.

Since this is a multi-port circuit, we plot only a few selected S-parameters, calculated via the CBFM as well as the direct method. Fig. **5.12** presents the plots, and demonstrates that the S-parameters obtained from the CBFM are in good agreement with those derived via the direct solution. In order to calculate the response of the entire amplifier circuit, S-parameters of the passive components are combined with other circuit components such as capacitors, resistors and active devices, and the entire system is subsequently simulated by using the circuit simulator. The gain of the amplifier circuit, which is the most important parameter that characterizes this circuit, is shown in Fig. **5.13**. We note that the gain plot also shows a very good agreement between the CBFM and direct solutions. Fig. **5.14** shows that, with thresholding, 96 CBFs are needed throughout the entire frequency band, as compared to 126 CBFs when all of the secondary CBFs are retained. Table **5-3** summarizes the time requirements for each of these solutions.

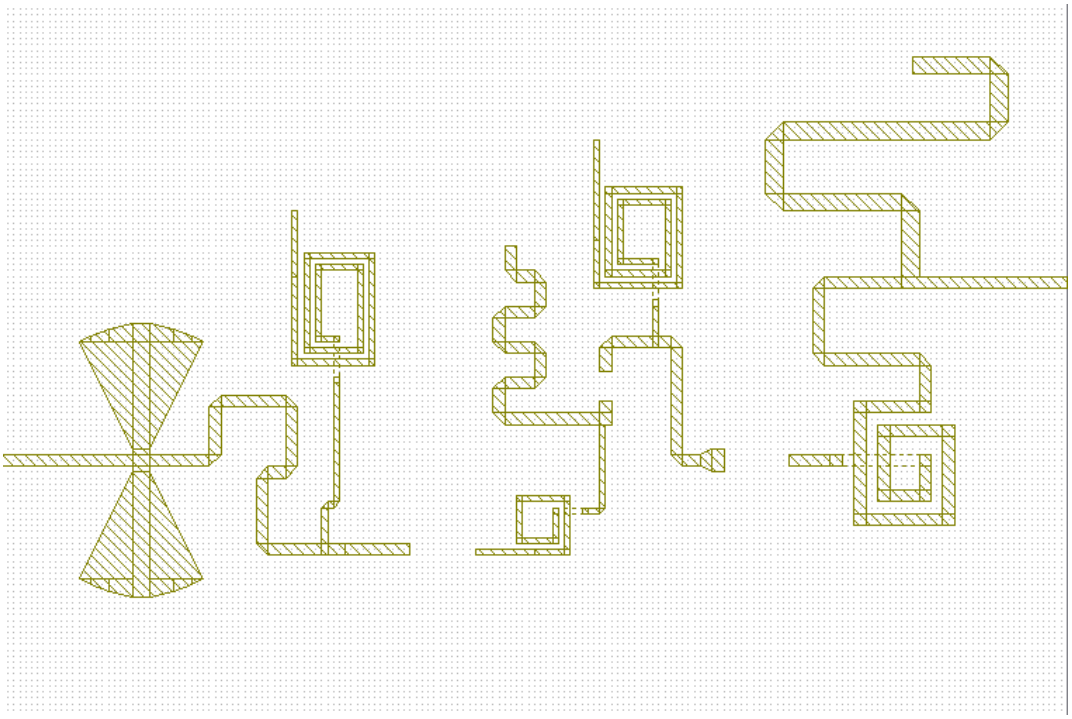

Fig. **5.11**: Passive components of a two-stage amplifier circuit.

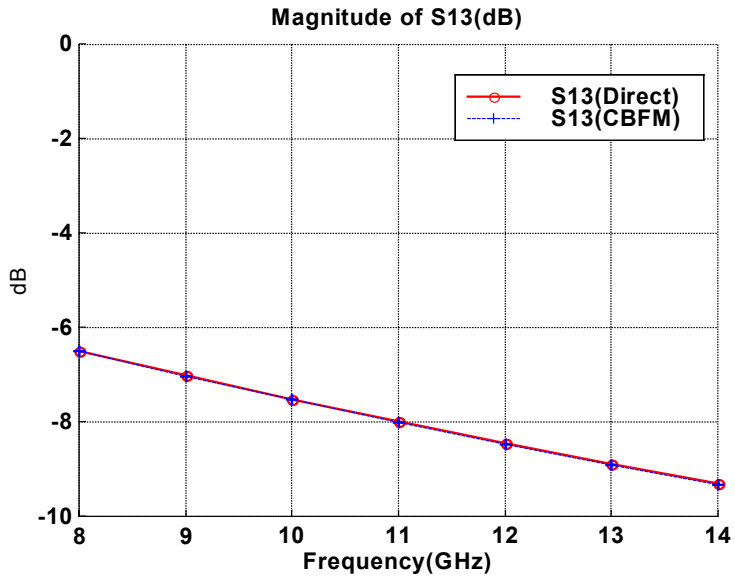

(a)

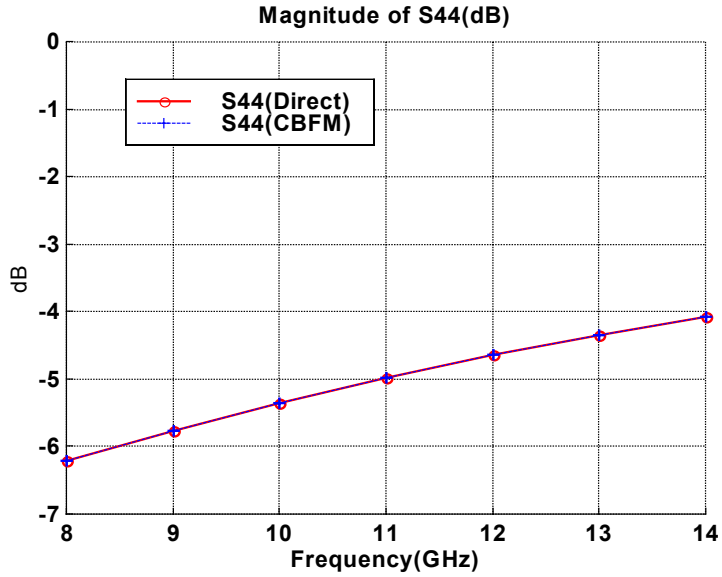

(b)

Fig. **5.12**: Comparison of the S-parameters of the passive components of a two-stage amplifier circuit computed by the CBFM using the primary and the secondary CBFs with thresholding, and the direct method. (a) Magnitude of S_{13}; (b) Magnitude of S_{44}.

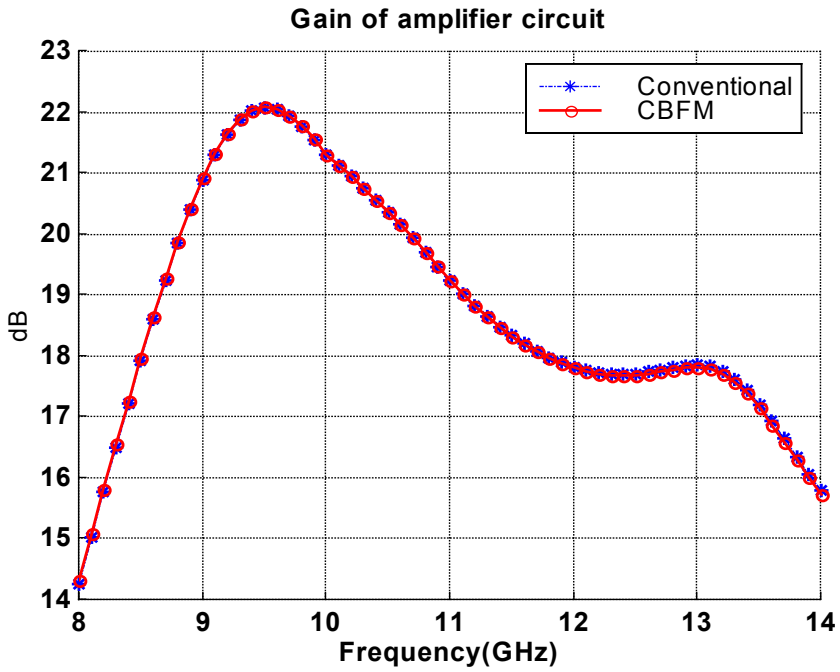

Fig. **5.13**: Comparison of the Gain of the entire two-stage amplifier circuit computed by using the CBFM and the conventional method.

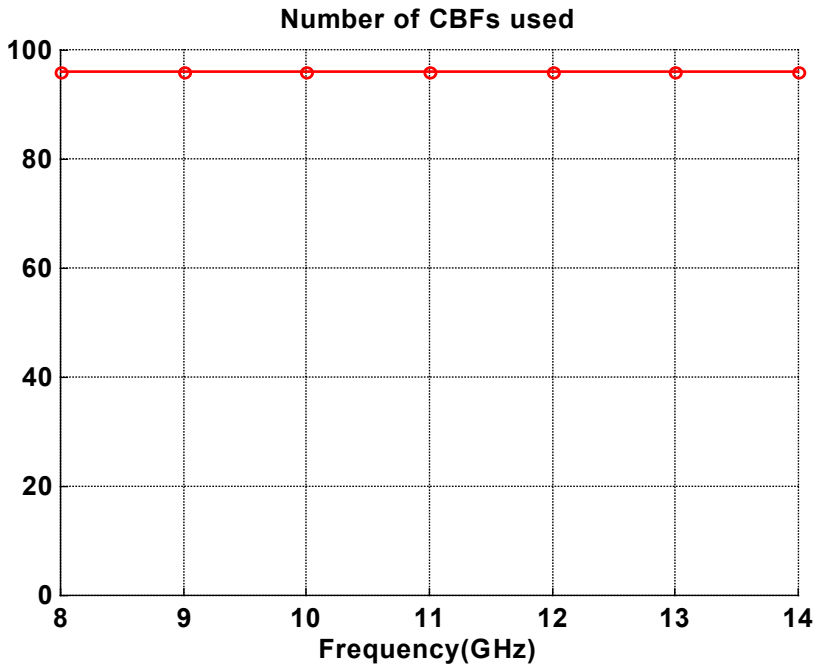

Fig. **5.14**: Number of the CBFs as functions of the frequency for the two-stage amplifier circuit.

Table **5-3**: Comparison of the total solve times for simulating the passive component of a two-stage amplifier over the frequency band 8 GHz to 14 GHz, between the CBFM using the primary and the secondary CBFs with thresholding, and the direct method.

	Time (sec)
Primary & secondary, with thresholding	132
Direct solution	968

5.4 Conclusions

In this chapter, we have presented a numerically efficient procedure–the Characteristic Basis Function Method (CBFM)–for the analysis of planar microstrip structures by combining the concepts of domain decomposition and high-level basis functions. The generation of the Characteristic Basis Functions (CBFs) involves the LU decomposition of only small-size matrices, whose dimensions are a fraction of the original matrix; in addition, the reduced matrix equation is small and well-conditioned. Mutual coupling between the CBFs are efficiently taken into account by using the secondary CBFs and a thresholding scheme that retains only the significant ones. The efficiency and accuracy of the CBFM have been demonstrated by applying it to several example problems, and comparing the resulting circuit parameters with those obtained by using the conventional MoM. The CBFM is a very general approach and we anticipate its applications to a wide variety of EM problems in the future.

Chapter 6

A NOVEL TECHNIQUE FOR ITERATIVE SOLUTION OF MATRIX EQUATION ARISING IN THE METHOD OF MOMENTS FORMULATION

6.1 Introduction

Iterative techniques are often used for an efficient solution of a large system of linear equations arising from the MoM formulation, often in conjunction with efficient algorithms for matrix-vector multiplication. Although the use of the latter helps reduce the solution time considerably by decreasing the time for each iteration, the number of iterations needed to achieve convergence governs the overall solution time. To accelerate convergence, one often turns to preconditioning, a topic which has been extensively covered in the literature [39-41] but is beyond the scope of this work. Instead, we focus on an important topic that is seldom ever discussed in the literature, *i.e.,* the choice of the initial guess that plays a significant role in determining the speed of convergence of an iterative procedure. Numerous attempts have been made in the past [42] to derive a good "guess" for the solution via extrapolation (though not in the context of iteration), which is derived from the solutions at previous frequencies. The procedure outlined in [42] can be quite complex because it is necessary to first express the induced current in terms of a set of constituent waves that have their unique frequency behaviors, which must be extrapolated individually. Although such an extrapolation approach has been successfully applied to a number of scattering problems–mostly two-dimensional in nature–the method is not as robust as desired for a general problem for which there is no obvious

way to split up the induced current into the constituent waves that can be conveniently extrapolated as functions of frequency. Yet another strategy is to extrapolate the solutions derived at previous frequencies by using a polynomial fitting [43]. Although this approach is considerably more general than the one in [42], it, too, has difficulties in dealing with structures that exhibit a resonance behavior.

With this background, we seek an alternate approach that takes advantage of the knowledge of the solutions at previous frequencies for extrapolation, although it does so in a completely different way than those implemented in [42,43]. In this thesis, we present a simple and efficient technique for generating the initial guess for an iterative solution of a large, dense system of linear equations arising in the Method of Moments (MoM) formulation of layered structure problems. The proposed approach involves an estimation of the solution vector based on the solutions at previous frequencies. The computational time involved in generating the estimate is negligible compared to that of the MoM matrix generation and the iterative solution. To demonstrate its versatility, we apply this technique to microstrip patch array antennas. We demonstrate the effectiveness of the proposed technique in accelerating the convergence of the iterative procedure. We also discuss the stopping criterion of the iteration procedure.

6.2 Theory and algorithm

One often desires an iterative solution of a matrix equation of the form

$$\mathbf{Ax} = \mathbf{b} \tag{6.1}$$

where $\mathbf{A}$ is the MoM matrix, $\mathbf{b}$ is the known excitation vector, and $\mathbf{x}$ is the unknown vector that we seek.

Most frequently, a zero initial guess is used for starting the iterative process. Experience shows that if we start the iteration process with an alternative choice, the convergence may be slower despite the fact that the initial residual error is considerably lower, certainly well below the one that we obtain with the zero initial guess. This phenomenon can be explained by tracing the behavior of the solution as we iterate. It is possible that the solution wonders off in the wrong direction for a few iterations before moving towards the correct value, and the solution may not converge after many iterations. Thus, although the CG algorithm ensures a monotonic decrease in the residual as a function of the number of iterations, it does not guarantee that the solution will also improve progressively with iteration. One reason for this is that the iteration process may initially drive the solution to a local minimum rather than to a global one. So it must recover from this undesirable detour before entering into the *n*-dimensional function space in which the global minimum resides. Since this behavior is typical for most initial guesses in the context of the CG algorithm, an initial choice of zero for the solution is still regarded as the most robust.

Thus we seek an alternate approach that takes advantage of the knowledge of the solutions at previous frequencies for generating the initial estimate of the current solution. The solutions at previous frequencies span a vector space $\mathbf{C^m}$ given by

$$\mathbf{C^m} \in \{\mathbf{x}_{n-1}, \mathbf{x}_{n-2}, \cdots, \mathbf{x}_{n-m}\} \tag{6.2}$$

where the index n corresponds to the current frequency at which the solution is desired, m refers to the number of previous frequencies at which the solution is pre-computed, and $\mathbf{x}$ is the solution vector. The vectors belonging to $\mathbf{C^m}$ are next orthonormalized by using a modified version of the Gram-Schmidt technique. So let $\hat{\mathbf{x}}_{n-i}$ be the i^{th} component of the modified vector space and let $\mathbf{x}_n$ be the solution to (**6.1**) that we desire to construct at the frequency n. An estimate of this unknown vector may be generated by using a linear combination of the solutions at previous frequencies belonging to the modified $\mathbf{C^m}$ as follows:

$$\mathbf{x}_n^{(0)} = \sum_{i=1}^{m} \alpha_i \hat{\mathbf{x}}_{n-i} \tag{6.3}$$

where α's are the complex expansion coefficients, and $\mathbf{x}_n^{(0)}$ is the initial estimate of the solution at the n^{th} frequency point. Substituting (**6.3**) into (**6.1**) leads to

$$\sum_{i=1}^{m} \alpha_i \mathbf{A}\hat{\mathbf{x}}_{n-i} = \mathbf{b} \tag{6.4}$$

A possible solution for α in (**6.4**) may be obtained by minimizing the projection of the $\mathbf{A}\mathbf{x}_j - \mathbf{b}$ along each of the vectors belonging to the modified function space $\mathbf{C^m}$ as follows:

$$\sum_{i=1}^{m} \alpha_i \left\langle \mathbf{A}\hat{\mathbf{x}}_{n-i}, \hat{\mathbf{x}}_{n-j} \right\rangle = \left\langle \mathbf{b}, \hat{\mathbf{x}}_{n-j} \right\rangle \quad for \quad j = 1, 2, \cdots, m \tag{6.5}$$

The above equation represents a set of linear equations, which are to be solved for the complex expansion coefficients. The initial estimate of the solution vector is then found by using α's computed from (**6.5**).

The residual error is commonly used to estimate the accuracy of the solution in the iterative solution process, and is given by

$$r^{(0)} = \frac{\left\| Ax_n^{(0)} - b \right\|_2}{\left\| b \right\|_2} \times 100 \qquad (6.6)$$

The CG process is started only if the residual error $r^{(0)}$ exceeds the tolerance limit. The CG iterative process is carried out until the residual error becomes smaller than a tolerance value. We choose 0.1% as the stopping criterion for layered structures, and this tolerance value turns out to be a reasonable one to achieve the accuracy of the final parameters of interest that we desire. We apply the extrapolated initial guess technique to patch array antennas; the efficiency of this technique is demonstrated in the following section.

6.3 Numerical results

The proposed approach, described in the previous section, will now be illustrated via an application to two microstrip patch array antennas.

6.3.1 Four-element microstrip patch array

The first example is a four-element microstrip patch array antenna built on a single dielectric layer with $\varepsilon_r = 2.2$ and a substrate thickness of $1.6\,mm$, as shown in Fig. 6.1. The geometry is discretized into rectangular cells and the surface currents are modeled by 2888 rooftop basis functions. The analysis was performed over the frequency

range 2.0 to 2.5 GHz at an interval of 12.5 MHz. The number of iterations needed for the CG with the zero and extrapolated initial guesses are plotted in Fig. **6.2(a)** as functions of frequency. Three solutions at previous frequencies were used to extrapolate the initial guess. The iteration process was terminated when the residual error was smaller than 0.1%. As can be seen from Fig. **6.2(a)**, the CG method requires a lower number of iterations when using the extrapolated initial guess over the entire band that includes the resonant frequency.

The magnitudes of S_{11} derived by the direct solution method, and the CG with the zero and extrapolated guess are plotted in Fig. **6.2(b)**, and good agreement between the two is observed over the entire frequency band. The CPU time for CG with the zero and extrapolated initial guess were 673 sec and 293 sec, respectively.

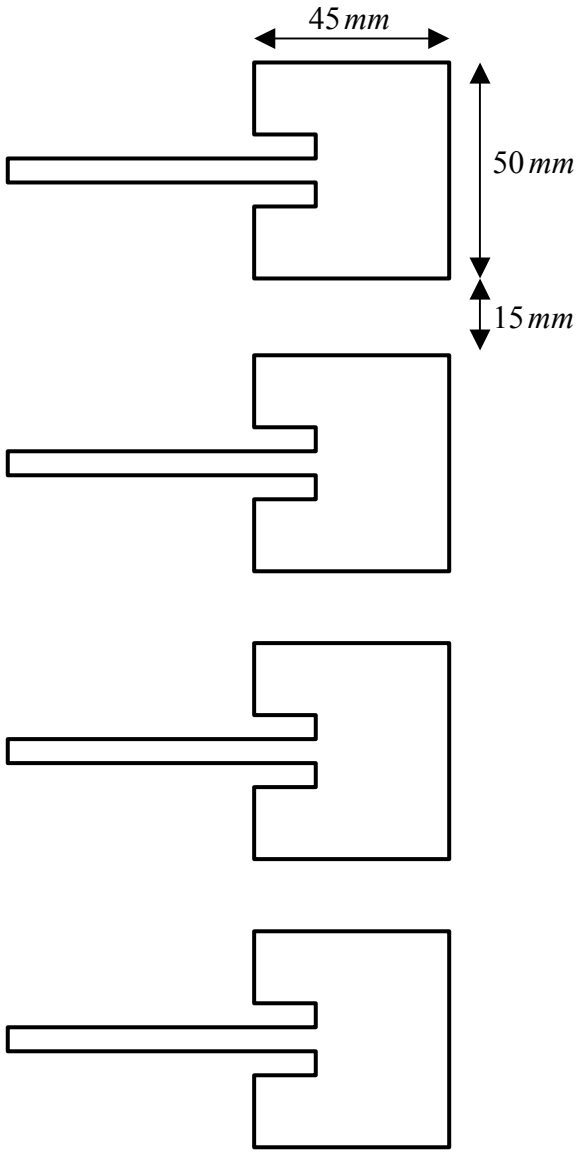

Fig. **6.1**: A four-element microstrip patch array antenna.

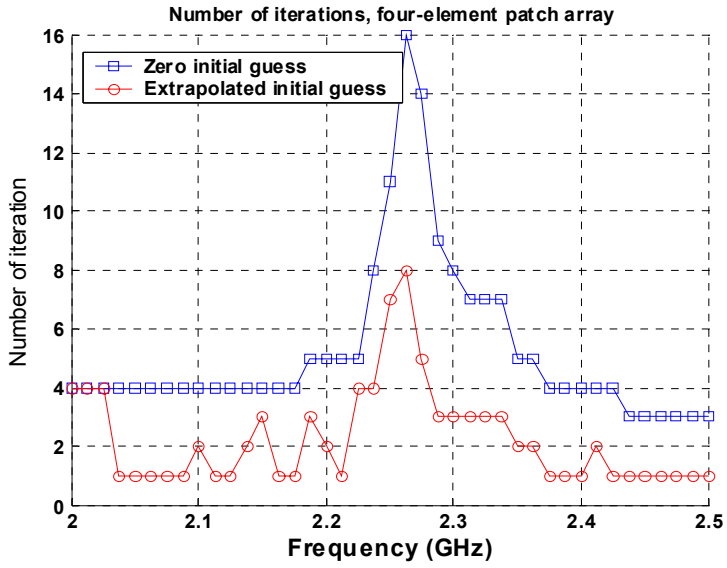

(a)

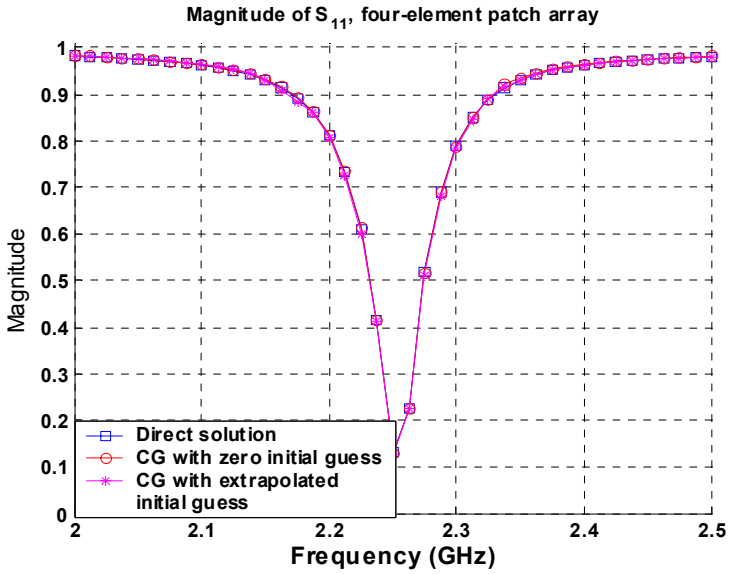

(b)

Fig. **6.2**: (a) Number of iterations needed to achieve 0.1 % residual error with the zero and extrapolated initial guesses. (b) S_{11} derived by the direct solution, and CG with the zero and extrapolated initial guesses.

6.3.2 Two-element proximity-coupled patch array

For our second example, we consider a two-element proximity-couple patch array antenna whose geometry, along with its dimensions, is illustrated in Fig. **6.3**. The feed lines are located inside the dielectric substrate whose $\varepsilon_r = 2.2$, and the antennas are printed on top of the substrate. The geometry is segmented into rectangular cells, and the surface currents of the conductors are represented as a superposition of the rooftop basis functions, leading to a total of 2414 unknowns. The array antenna is analyzed over the frequency range 3 to 5 GHz with a 100 MHz frequency step, using the CG iteration scheme with the zero and extrapolated initial guesses. The tolerance 0.1% was used as the stopping criterion, and the number of iterations needed for CG with the zero and extrapolated guesses are plotted as functions of frequency in Fig. **6.4(a)**. As in the previous example, CG with the extrapolated initial guess required an equal or smaller number of iterations over the entire frequency band. The magnitudes of S_{11} derived by the direct solution, and CG with the zero and extrapolated initial guesses are plotted in Fig. **6.4(b)** and, as in the previous example, the three results show good agreements. The CPU time required for CG with the zero initial guess was 270 sec, whereas it was 185 sec when the extrapolated guess was used.

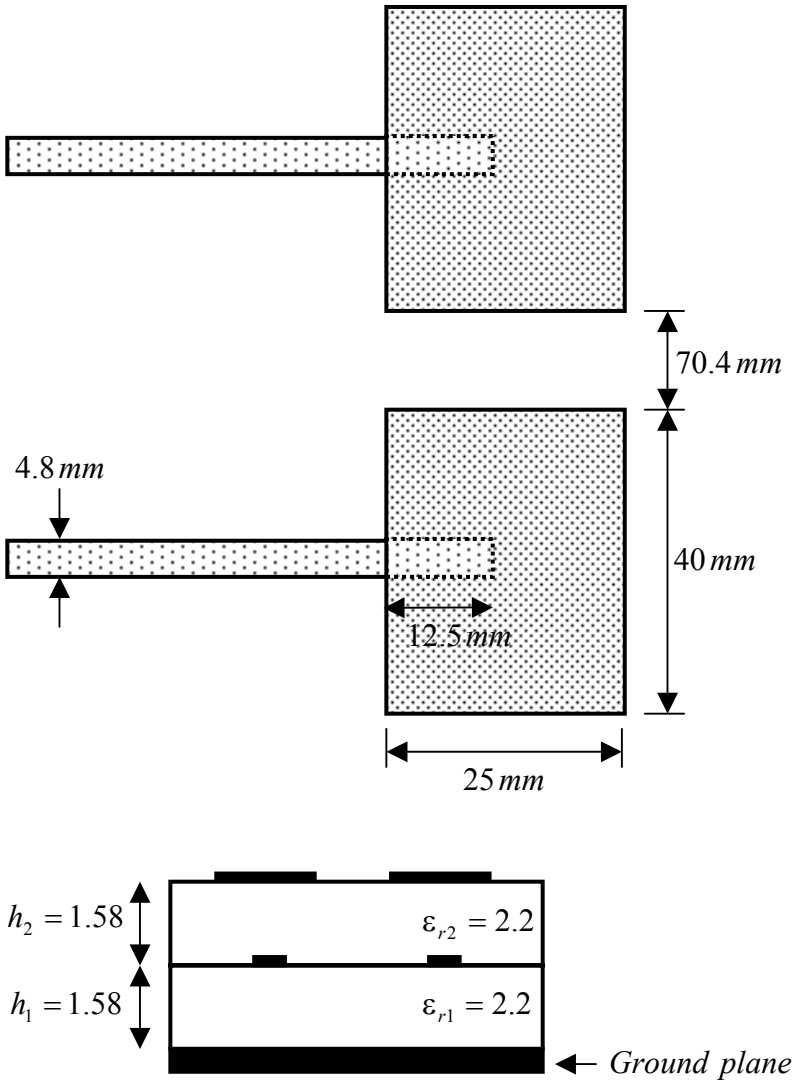

Fig. **6.3**: A two-element microstrip patch antenna.

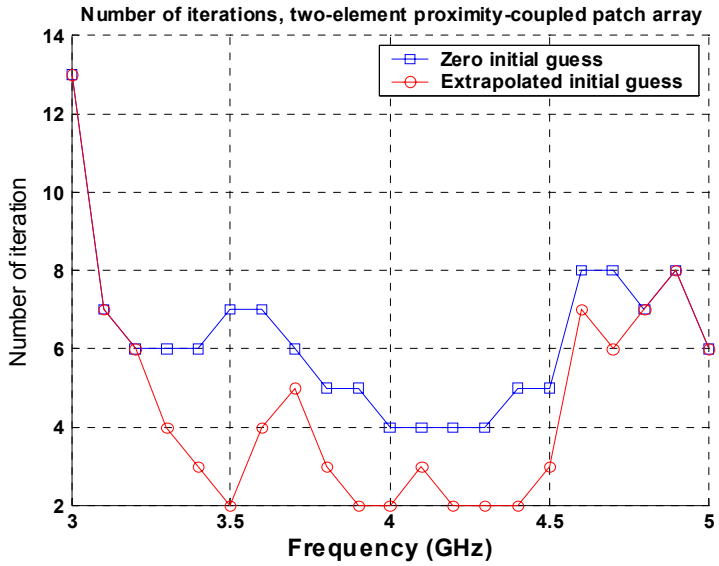

(a)

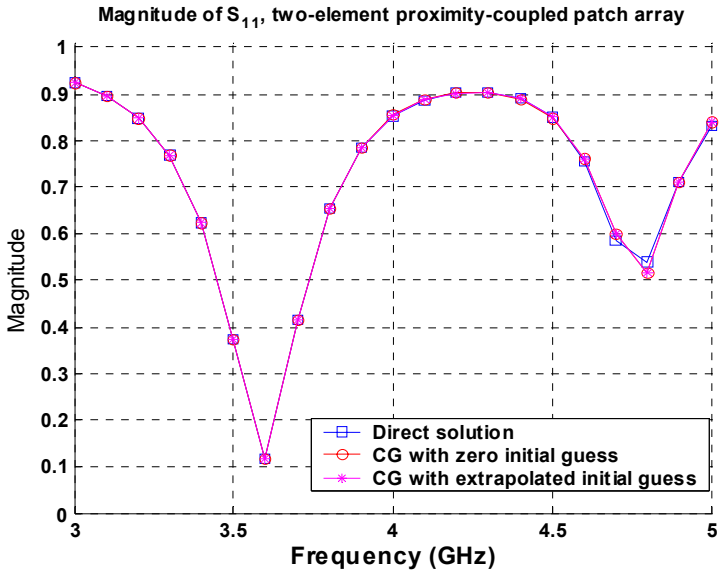

(b)

Fig. **6.4**: (a) Number of iterations needed to achieve 0.1 % residual error with the zero and extrapolated initial guesses. (b) S_{11} derived by the direct solution, and CG with the zero and extrapolated initial guesses.

6.4 Conclusion

In this chapter, we have presented a simple and efficient technique for generating the initial guess in the context of an iterative solution of a large dense system of linear equations arising in the Method of Moments (MoM) formulation of layered structure problems. The proposed approach involves estimation of the solution vector based on the solutions at previous frequencies, which is further refined, if required, by using the Conjugate Gradient (CG) technique. It has been demonstrated that the number of iterations required by the CG method for convergence can be reduced by using the extrapolated initial guess.

Chapter 7

CONCLUSIONS AND FUTURE WORK

This thesis has presented several techniques for improving the efficiency of the MoM analysis of layered structures.

In Chapter 3, we have presented a numerically efficient impedance matrix generation algorithm called the Fast Matrix Generation (FMG) scheme. Two matrix generation schemes that make use of the smooth behavior of the Green's function, and the concept of the equivalent dipole for computing the matrix elements, have been introduced. In this approach, the elements corresponding to the basis/testing function pairs with the separation distance larger than a threshold value are evaluated by using the FMG technique, while the remainder elements are computed by using the rigorous method. Since the evaluation of the impedance matrix element by the use of the FMG technique only involves simple arithmetic operations, the CPU time required for the impedance matrix generation is reduced significantly. Numerical results for several sample problems for printed-layered structures are presented, verifying the fact that the FMG technique reduces the impedance matrix computation time substantially, while maintaining the accuracy of the parameters of interest. Moreover, the algorithm is very general, so it is possible to extend it to other applications such as the solutions of three-dimensional scattering problems.

A new and efficient impedance matrix interpolation scheme for the analysis of printed-layered structures has been presented in Chapter 4. It has been demonstrated that

both the matrix elements and the final parameters derived by using direct and interpolation methods are in very good agreement. Since the proposed algorithm is robust and systematic, it can be readily incorporated into existing codes. The computation time for the analysis of a layered structure can be reduced significantly, since the use of the interpolation reduces the time for generating the impedance matrices to a small fraction of that achieved by direct computation. Although this algorithm was applied to layered structures, it is equally applicable to other classes of problems, such as the radiation and scattering involving objects in free space.

In Chapter 5, a numerically efficient procedure, the Characteristic Basis Function Method (CBFM), has been presented for the analysis of planar microstrip structures by combining the concepts of domain decomposition and high-level basis functions. The generation of the Characteristic Basis Functions (CBFs) involves the LU decomposition of only small-size matrices whose dimensions are a fraction of the original matrix; in addition, the reduced matrix equation is small and well-conditioned. Mutual coupling between the CBFs is efficiently taken into account by using the secondary CBFs and a thresholding scheme that retains only the significant ones. The efficiency and accuracy of the CBFM have been demonstrated by applying it to several sample problems and comparing the resulting circuit parameters with those obtained by using the conventional MoM. Since the CBFM is a very general approach, we anticipate its applications to a wide variety of EM problems in the future.

Finally, a simple and efficient technique for generating the initial guess in the context of an iterative solution of a large dense system of linear equations arising in the Method of Moments (MoM) formulation of layered structure problems has been

introduced in Chapter 6. The proposed approach involves estimation of the solution vector based on the solutions at previous frequencies, which is further refined, if required, by using the Conjugate Gradient (CG) technique. It has been demonstrated that the number of iterations required by the CG method for convergence can be reduced by using the extrapolated initial guess.

The FMG and the impedance matrix interpolation techniques are new approaches to accelerating the matrix generation for a single frequency and a band of frequencies, respectively. It should be possible to combine these two techniques to achieve a higher level of efficiency, *i.e.,* the matrix interpolation can be performed by using the sampled matrices computed by the FMG technique. Though a more sophisticated algorithm is needed since there are two levels of approximations involved in the matrix element generation, spatial and frequency, respectively, a tremendous timesaving is expected from the combination since each of these techniques can save significant computation time – more than 90% in some cases.

Other meaningful possibilities would entail the application of these techniques, or their combinations, as mentioned above, to other classes of electromagnetic problems. These two techniques, the FMG and the impedance matrix interpolation, were initially developed for layered structures in conjunction with the closed-form Green's function. However, it should be possible to extend them to general classes of electromagnetic problems, such as the free space antenna and scattering problems, since the free space Green's function can be regarded as a special case of the closed-form Green's function for layered structures. Thus, it is believed that the two methods or a combination of them

can be successfully applied to a wide variety of electromagnetic (EM) scattering and radiation problems, as well as to microwave circuit and antenna designs.

Bibliography

1. A. Taflove, *Computational Electrodynamics: The Finite-Difference Time-Domain Method*, Norwood, MA: Artech House, 1997.

2. J. M. Jin, *The Finite Element Method in Electromagnetics*, New York: Wiley, 1993.

3. R. F. Harrington, *Field Computation by Moment Methods*, New York: Macmillan, 1968.

4. W. C. Chew, *Waves and Fields in Inhomogeneous Media*. New York: IEEE Press, 1990.

5. Y. L. Chow, J. J. Yang, D. F. Fang, and G. E. Howard, "A closed-form spatial Green's function for the thick substrate," *IEEE Trans. Microwave Theory and Tech*., vol. 39, pp. 588–592, Mar. 1991.

6. M. I. Aksun, "A robust approach for the derivation of closed-form Green's functions," *IEEE Trans. Microwave Theory and Tech*., vol. 44, pp. 651–658, May 1996.

7. W. C. Chew, J. M. Jin, C. C. Lu, E. Michielssen, and J. M. Song, "Fast solution methods in electromagnetics," *IEEE Trans. Antennas and Propagation*, vol. 45, pp. 533-543, Mar. 1997.

8. L. Alatan, M. I. Aksun, and T. Birand, "Improving the numerical efficiency of the method of moments for printed geometries," *IEEE AP-S Int. Symp. Dig.*, Seattle, WA, June 1994, pp. 1698-1701.

9. L. Alatan, M. I. Aksun, K. Mahadevan, and M. T. Birand, "Analytical evaluation of the MoM matrix elements," *IEEE Trans. Microwave Theory and Tech.*, vol. 44, pp. 519-525, Apr. 1996.

10. A. Samet and A. Bouallegue, "Fast and rigorous calculation method for MoM matrix elements in planar microstrip structures," *Electronics Letters*, vol. 36, pp. 801-803, Apr. 2000.

11. N. Kinayman and M. I. Aksun, "Efficient Evaluation of Spatial-Domain MoM Matrix Entries in the Analysis of Planar Stratified Geometries," *IEEE Trans. Microwave Theory and Tech.*, vol. 48, pp. 309-312, Feb. 2000.

12. R. Kipp and C. H. Chan, "Triangular-domain basis functions for full-wave analysis of microstrip discontinuities," *IEEE Trans. Microwave Theory and Tech.*, vol. 41, pp. 1187-1194, June 1993.

13. K. Naishadham, T. W. Nuteson, and Raj Mittra, "Parametric interpolation of the Moment Matrix in surface integral equation formulation," *International Journal of RF and Microwave Computer-Aided Engineering*., vol. 9, no. 6, pp. 474-489, Nov. 1999.

14. J. R. Mosig, "Arbitrarily shaped microstrip structures and their analysis with a mixed potential integral equation," *IEEE Trans. Microwave Theory and Tech*., vol. 36, pp. 314-323, Feb. 1988.

15. K. A. Michalski and D. Zheng, "Electromagnetic scattering and radiation by surfaces of arbitrary shape in layered media: Part I: Theory," *IEEE Trans. Antennas and Propagation*, vol. 38, pp. 335-344, Mar. 1990.

16. T. Itoh, *Numerical Techniques for Microwave and Millimeter-Wave Passive Structures*. New York: Wiley, 1989.

17. E. H. Newman and D. Forrai, "Scattering from a microstrip patch," *IEEE Trans. Antennas and Propagation*, vol. 35, pp. 245-251, Mar. 1987.

18. E. H. Newman, "Generation of wide-band data from the method of moments by interpolating the impedance matrix," *IEEE Trans. Antennas and Propagation*, vol. 36, pp. 1820-1824, Dec. 1988.

19. K. Virga and Y. Rahmat-Samii, "Wide-band evaluation of communications antennas using [Z] matrix interpolation with the method of moments," *Proc. of IEEE Antennas and Propagat. Symp.*, vol. 2, pp. 1262-1265, Jun. 1995.

20. K. L. Virga and Y. Rahmat-Samii, "Efficient wide-band evaluation of mobile communications antennas using [Z] or [Y] matrix interpolation with the method of moments," *IEEE Trans. Antennas and Propagation*, vol. 47, pp. 65-76, Jan. 1999.

21. A. S. Barlevy and Y. Rahmat-Samii, "An efficient method for wide band characterization of periodic structures using a modified Z matrix interpolation," *Proc. of IEEE Antennas and Propagat. Symp.*, vol. 1, pp. 56-59, Jul. 1997.

22. A. S. Barlevy and Y. Rahmat-Samii, "Characterization of electromagnetic band-gaps composed of multiple periodic tripods with interconnecting vias: concept, analysis, and design," *IEEE Antennas and Propagat. Symp.*, AP-49, pp. 343-353, Mar. 2001.

23. X.C. Wei and E. P. Li, "Wide-band EMC analysis of on-platform antennas using impedance-matrix interpolation with the moment method-physical optics method," *IEEE Trans. Electromagnetic Compatibility*, vol. 45, pp. 552-556, Aug. 2003.

24. Junho Yeo and Raj Mittra, "An algorithm for interpolating the frequency variations of method-of-moments matrices arising in the analysis of planar microstrip structures," *IEEE Trans. Microwave Theory and Tech.*, vol. 51, pp. 1018-1025, Mar. 2003.

25. J. R. Mosig and F. E. Gardiol, "Analytical and numerical techniques in the Green's function treatment of microstrip antennas and scatterers," *Proc. Inst. Elec. Eng.*, pt. H, vol. 130, pp. 175-182, Mar. 1983.

26. J. R. Mosig and F. E. Gardiol, "General integral equation formulation for microstrip antennas and scatterers," *Proc. Inst. Elec. Eng.*, pt. H, vol. 132, pp. 424-432, Dec. 1985.

27. Y. L. Chow and W. C. Tang, "3-D Green's functions of microstrip separated into simpler terms – behavior, mutual interaction and formulas of the terms," *IEEE Trans. Microwave Theory and Tech.*, vol. 49, no. 8, pp. 1483-1491, Aug. 2001.

28. K. C. Gupta, "Emerging trends in millimeter-wave CAD," *IEEE Trans. Microwave Theory and Tech.*, vol. 46, pp. 747-755, June 1998.

29. J. S. Zhao, W. C. Chew, C. C. Lu, E. Michielssen and J. Song, "Thin-stratified medium fast-multipole algorithm for solving microstrip structures," *IEEE Trans. Microwave Theory and Tech*., vol. MTT-46, pp. 395-403, Apr. 1998.

30. F. X. Canning, "Improved impedance matrix localization method," *IEEE Trans. Antennas and Propagation*, vol. AP-41, pp. 659-667, May 1993.

31. K. F. Sabet, J. C. Cheng and L. P. B. Katehi, "Efficient wavelet-based modeling of printed circuit antenna arrays," *IEE Proc. on Microwaves, Antennas and Propagation*, vol. 146, pp. 298-304, Aug. 1999.

32. G. E. Howard and Y. L. Chow, "Diakoptic theory for the microstrip structures," in *IEEE AP-S Int. Symp. Dig.*, Dallas, TX, May 8-10, 1990, pp. 1079-1082.

33. F. Schwering, N. N. Puri and C. M. Butler, "Modified Diakoptic Theory of Antennas," *IEEE Trans. Antennas and Propagation*, vol. 34, pp. 1273-1281, Nov. 1986.

34. S. Ooms and D. D. Zutter, "A New Iterative Diakoptics-Based Multilevel Moments Method for Planar Circuits," *IEEE Trans. Microwave Theory and Tech.*, vol. 46, pp. 280-291, Mar. 1998.

35. E. Suter, and J. R. Mosig, "A subdomain multilevel approach for the efficient MoM analysis of large planar antennas," *Microwave and Optical Technology Letters*, vol. 26, pp.270-277, Aug. 2000.

36. R. Mittra, K. Du, V. V. S. Prakash, J. Yeo, and S. J. Kwon, "Efficient simulation of MMIC and RFIC systems using a new matrix generation technique and the MNM iterative solver," *Workshop on EM-based CAD & optimization of waveguide components, planar circuits & antennas, 2002 IEEE MTT-S Microwave Symposium Workshop*, June 2002, Seattle.

37. Raj Mittra, "Development of Efficient CAD Tools for the Simulation of RFIC and MMIC Package," *Proceedings of the IASTED International Conference, Wireless and Optical Communications*, July 17-19, 2002, pp. 1-5, Banff, Canada.

38. V. V. S. Prakash and R. Mittra, "The Characteristic Basis Function Method: A new technique for Efficient Solution of Method of Moments Matrix Equations", *Microwave and Optical Technology Letters*, Jan. 2003.

39. Y. Y. Botros and J. L. Volakis, "Preconditioned generalized minimal residual iterative scheme for perfectly matched layer terminated applications," *IEEE Microwave and Guided Wave letters*, vol.9, no.2, pp.45-47, Feb. 1999.

40. J. R. Poirier, P. Borderies, R. Mittra, and V. Varadarajan, "Numerically efficient solution of dense linear system of equations arising in a class of electromagnetic scattering problems," *IEEE Trans. Antennas and Propagation*, vol.46, pp.1169-1175, Aug. 1998.

41. V. V. S. Prakash and R. Mittra, "Multi-Frontal preconditioners for iterative solvers," *IEEE Antenna Propagation symposium*, Boston, USA, July 2001.

42. Z. Altman and R. Mittra, "A technique for extrapolating numerically rigorous solutions of electromagnetic scattering problems to higher frequencies and their scaling properties," *IEEE Trans. Antennas and Propagation*, vol.47, pp.744-751, April 1999.

43. J. F. Ma, R. Mittra and N. T. Huang, "Improving the convergence of iterative solution of matrix equations in the method of moments formulation using extrapolation techniques," *IEE Proc. on Microwaves, Antennas and Propagation*, vol. 150, pp. 253-257, Aug. 2003.

VITA

Soon Jae Kwon

Soon Jae Kwon was born in Kangwon, Korea on September 6, 1967. He enrolled in the Electronics Engineering program at Korea University, Seoul, in 1986 and received his B. S. degree in February 1990. He received his M.S. degree in Electronics Engineering in August 1992 at Korea University, Seoul, Korea. From August 1992 to May 1998 he was employed as a Hardware Design Engineer at LG Information and Communications (now LG Electronics), Seoul, Korea. He began his doctoral studies in Electrical Engineering at the Pennsylvania State University in the fall of 1998 and has held a research assistantship at the Electromagnetic Communication Laboratory at Penn State. His current research interests are in the area of computational electromagnetics with an emphasis on the development of numerically efficient techniques for the analysis of passive microwave device by the Method of Moments (MoM) and Finite Difference Time Domain (FDTD).